JEM Journal of Experimental Medicine

TECHNICAL ADVANCES AND RESOURCES

Local gene editing of fibroblasts in tumors reveals a new cancer-associated fibroblast state

Nicholas F. Kuhn[1,2], Itzia Zaleta-Linares[1,2], Kenneth H. Hu[3,4], Tristan Courau[1,2], Brittany Davidson[1,2,5], Tammie Tam[1,2,5], Chih-Wei Chu[3,4], Maxime J. Kinet[6], Michael D. Rosenblum[7], Alexis J. Combes[1,2,5], William A. Nyberg[6], Justin Eyquem[2,6,8,9], and Matthew F. Krummel[1,2]

Fibroblasts play critical roles in regulating cellular relationships during tissue homeostasis, immunity, and tumor biology at multiple sites. However, tools to perturb fibroblasts at just one site *in vivo* are limited, restricting our understanding of how these cellular relationships act locally. We optimized local gene editing of fibroblasts in mouse tumor models to investigate how fibroblast perturbations affect the tumor microenvironment (TME). By knocking out receptors *Osmr*, *Tgfbr2*, or *Il1r1* on cancer-associated fibroblasts (CAFs), we uncover that TGFBR2 signaling loss induces the emergence of a new *Col18a1*^{hi} CAF cell state that is associated with worse survival in pancreatic cancer patients. Combinatorial gene KOs in CAFs reveals a circuit where these *Col18a1*^{hi} CAFs reshape the TME by recruiting Siglec-F^{hi} neutrophils via *Cxcl5* expression, and where this *Col18a1*^{hi} CAF cell state is dependent on TNFR1 and canonical Wnt signaling. Together, a fast, affordable, and modular engineering method is demonstrated, allowing discovery of modified fibroblast identities and local intercellular relationships in the TME.

Introduction

Fibroblasts play essential roles as both mediators of homeostasis and drivers of transitions in tissues, for example, during repair (Buechler et al., 2021b; Foster et al., 2021; Guerrero-Juarez et al., 2019; Hu et al., 2023; Mascharak et al., 2021; Plikus et al., 2021). However, fibroblast dysregulation has been associated with many chronic diseases, including fibrosis, autoimmunity, and cancer (Henderson et al., 2020; Kinchen et al., 2018; Korsunsky et al., 2022; Sahai et al., 2020; Tsukui et al., 2020). In cancer specifically, the term "cancer-associated fibroblast" (CAF) refers to a cell that is defined by the absence of epithelial, endothelial, and immune cell lineage markers and lack of cancer cell mutations (Sahai et al., 2020). Recent work has greatly expanded our understanding of the heterogenous CAF cell states in human cancer and mouse tumor models (Grout et al., 2022; Helms et al., 2022; Krishnamurty et al., 2022; McAndrews et al., 2022), where CAF subset identity is informed by their transcriptional state and ability to influence tumor, endothelial, and immune cell function *ex vivo* in experimental co-culture conditions (Biffi et al., 2019; Elyada et al., 2019; Öhlund et al., 2017).

However, studying the interaction of CAFs with other cells in biological settings has been challenging, as *in vitro* models do not fully model complex three-dimensional tumor microenvironments (TMEs), and testing gene functions in mice has suffered from a lack of methods to modify fibroblast gene expression locally at scale (Sahai et al., 2020). In some cases and to circumvent these limitations, tumor cells have been co-injected with defined CAF subsets, which revealed different CAF subset functions in these tumor models (Hutton et al., 2021). However, the injected CAFs are often outcompeted by host fibroblasts, leading to poor engraftment of the co-injected CAFs (Sahai et al., 2020). Mouse models using Cre-loxP provide a highly controllable method to perturb individual genes in fibroblasts by using Cre-driver lines such as *Pdgfra*-Cre, *Col1a2*-Cre, or others that have been developed recently (Plikus et al., 2021). These models require mouse breeding of Cre-driver lines with floxed genes of interest, are time- and cost-intensive, and, when combined with inducible cell-depletion genes, such as diphtheria toxin receptor, typically deplete large populations of fibroblasts globally (Roberts et al., 2013), which limits the ability to draw conclusions about their specific roles in a defined environment. Thus, we set out to develop an *in vivo* fibroblast perturbation platform that is localized, fast, affordable, and modular.

Viral vectors have been extensively used to modify cells *in vivo*, with recombinant adeno-associated viruses (AAVs) being a popular choice due to their low immunogenicity and cytotoxicity (Wang et al., 2019). We hypothesized that local delivery of a

[1]Department of Pathology, University of California, San Francisco, San Francisco, CA, USA; [2]Bakar ImmunoX Initiative, University of California, San Francisco, San Francisco, CA, USA; [3]Department of Immunology, The University of Texas MD Anderson Cancer Center, Houston, TX, USA; [4]James P. Allison Institute, The University of Texas MD Anderson Cancer Center, Houston, TX, USA; [5]UCSF CoLabs, University of California, San Francisco, San Francisco, CA, USA; [6]Department of Medicine, University of California, San Francisco, San Francisco, CA, USA; [7]Department of Dermatology, University of California, San Francisco, San Francisco, CA, USA; [8]Gladstone-UCSF Institute of Genomic Immunology, San Francisco, CA, USA; [9]Parker Institute for Cancer Immunotherapy, San Francisco, CA, USA.

Correspondence to Nicholas F. Kuhn: nicholas.kuhn@ucsf.edu; Matthew F. Krummel: matthew.krummel@ucsf.edu.

https://doi.org/10.1084/jem.20251228

guide RNA (gRNA) via AAV in combination with conditional expression of Cas9 in fibroblasts could generate local KOs of target genes in a defined area of the skin, allowing subsequent study of tumor growth within that tissue area of fibroblast perturbation. Similar strategies of local or organ-specific cell perturbations have been employed to target a variety of cells, such as brain cells (Challis et al., 2022), muscle cells (Tabebordbar et al., 2021), or hepatocytes (Wang et al., 2021). Additionally, screening efforts designed around varying the AAV capsid sequence have identified AAV serotypes with altered cell tropisms (Bryant et al., 2021; Maheshri et al., 2006; Nyberg et al., 2023). Among those, the evolved variants 7m8 and DJ (Westhaus et al., 2020), together with the natural variant AAV serotype 1 (AAV1) (Ellis et al., 2013), have emerged as candidates for efficient fibroblast targeting.

To test our approach, we targeted the following three receptors known to shape CAF biology: (1) transforming growth factor β type II receptor (*Tgfbr2*) encoding a surface receptor that upon binding to its ligand TGF-β1 together with TGFBR1 has been demonstrated to drive profound phenotypic changes in fibroblasts (Massagué and Sheppard, 2023). In tumors, TGF-β1–mediated activation of fibroblasts leads to a contractile phenotype that is associated with increased extracellular matrix (ECM) production, which leads to an overall remodeling of the ECM in the growing tumor (Batlle and Massagué, 2019; Chakravarthy et al., 2018; Laklai et al., 2016). As TGFBR2 is expressed on a multitude of epithelial, stromal, and immune cells, deciphering how TGFBR2 signaling affects tumor growth requires targeted deletion (Krishnamurty et al., 2022). (2) Oncostatin M (OSM) receptor (*Osmr*) encodes a surface receptor that has been implicated in stimulating a pro-inflammatory gene program in fibroblasts (Araujo et al., 2022; Hu et al., 2023; Lee et al., 2021). (3) Interleukin 1 receptor type 1 (*Il1r1*), which—in colorectal cancer lesions—stimulates CAFs to adopt an inflammatory cell state that is associated with increased tumor infiltration of immunosuppressive macrophages (Koncina et al., 2023) and results in therapy-induced senescence of CAFs (Nicolas et al., 2022), both contributing to increased tumor growth.

Here, we sought to develop tools that are adaptable for knocking out genes, singly or in combination. Focusing on these three genes that have produced data indicating intratumoral roles for them in fibroblasts, we sought to develop both the method for localized fibroblast engineering and to answer questions about the localized role of these genes and pathways in intratumoral populations of fibroblasts.

Results

Targeted local KO of gene of interest in fibroblasts

We hypothesized that two elements were necessary for an approach to locally genetically engineer fibroblasts. First is a vector system that delivers a gRNA to the fibroblast. Together with preexisting fibroblast-specific alleles that regulate expression of Cas9, the choice of gRNA provides modular flexibility to target any gene of interest for gene editing. Second is identification of a highly efficient AAV serotype that delivers necessary elements to fibroblasts locally *in vivo*. Toward the first, we designed a self-complementary AAV (scAAV) (McCarty et al., 2001; McCarty et al., 2003; McCarty, 2008; Wang et al., 2003) cargo cassette comprised of the human U6 promoter (hU6) driving RNA polymerase III–mediated expression of a gRNA and a hybrid form of the CBA promoter (CBh) (Gray et al., 2011) driving mCherry expression as a transduction readout (Fig. 1 A). Cargo plasmids encoding gRNAs against *Thy1* (gene encoding Thy1/CD90) or *Pdpn* (gene encoding podoplanin, PDPN) were packaged into scAAVs with the AAV1 capsid—from here on referred to as AAV-gRNA—and used to transduce the mouse fibroblast cell line NIH/3T3 expressing Cas9 (NIH/3T3.Cas9) (Fig. 1 B). The scAAV was transduced at an efficiency of >75% and induced KO noticeable by loss of surface expression of Thy1 or PDPN (Fig. 1, C and D). A comparison of the AAV1 capsid with the recently developed fibroblast-tropic synthetic capsids 7m8 (Isgrig et al., 2019; Westhaus et al., 2020) and DJ (Grimm et al., 2008) showed similar transduction and KO efficiency *in vitro* (Fig. S1 A).

This prompted us to find a solution to the second requirement to identify a highly efficient AAV serotype for local delivery and execution of gene editing elements to fibroblasts *in vivo*. For this, Cas9 expression in host fibroblasts was achieved by combining a *Pdgfra*-driven Cre allele (either *Pdgfra*-Cre or *Pdgfra*-CreERT2 [Chung et al., 2018; Roesch et al., 2008]) with the *Rosa26*-LSL-Cas9-EGFP allele (Platt et al., 2014), hereafter referred to as *Pdgfra*-Cas9-EGFP mice (Materials and methods for details). In single-cell suspensions of tumors, fibroblasts were gated using the markers: DAPI$^-$ CD31$^-$ CD45$^-$ E-Cadherin$^-$ MCAM$^-$ Thy1$^+$ PDPN$^+$ (Fig. S1 B). Of those, 97.3 ± 1.3% (mean ± SD) were GFP$^+$ in *Pdgfra*-Cre;R26-LSL-Cas9-EGFP mice and 71.2 ± 11.7% in *Pdgfra*-CreERT2;R26-LSL-Cas9-EGFP mice (Fig. S1 C), indicating a high percentage of Cas9 expressing CAFs. Conversely, gating on EGFP$^+$ cells revealed that 93–97% of all recombined cells express fibroblast markers Thy1$^+$ and PDPN$^+$ (Fig. S1 D). PDPN staining of EGFP$^+$ cells in tumors was confirmed by microscopy (Fig. S1 E). Testing local delivery of AAV-gRNA was performed by injecting 1e10 viral genomes (vg) of AAV-gThy1-CBh-mCherry s.c. on the dorsal flank of mice and marking the injection site to allow subsequent injection of YUMM5.2 mouse melanoma tumor cells at the same site on the next day (Fig. S1 F). We excluded the 7m8 capsid from further *in vivo* experiments because s.c. injection of 7m8-serotyped scAAV transduced the panniculus carnosus (Fig. S1 G). When comparing AAV1 versus DJ capsids, measuring mCherry expression in the CAFs that populate the growing tumor mass was used as a readout for transduction efficiency, and surface expression of Thy1 was used as a readout for KO efficiency of the AAV. AAV1- and DJ-serotyped scAAVs transduced CAFs at different efficiencies (day 7 time point: 78.5 ± 8.5% [mean ± SD] and 53.6 ± 11.9% [mean ± SD] mCherry$^+$, respectively, Fig. S1 H), leading to higher Thy1-negative levels by scAAV1 versus scDJ (90.9 ± 1.8% [mean ± SD] and 78 ± 4.9% [mean ± SD] Thy1-negative, respectively, Fig. S1 H). AAV1 also predominantly infected CAFs in the *Pdgfra*-Cas9-EGFP mice (93.3 ± 1.7% [mean ± SD]) (Fig. S1, I and J). On this basis, our future experiments used scAAV1.

Next, we tested efficiency of local gene KO in these CAFs by targeting *Thy1* for deletion (Fig. 1 E). More than 85% of all CAFs were Thy1-negative 7 days after tumor challenge, compared with

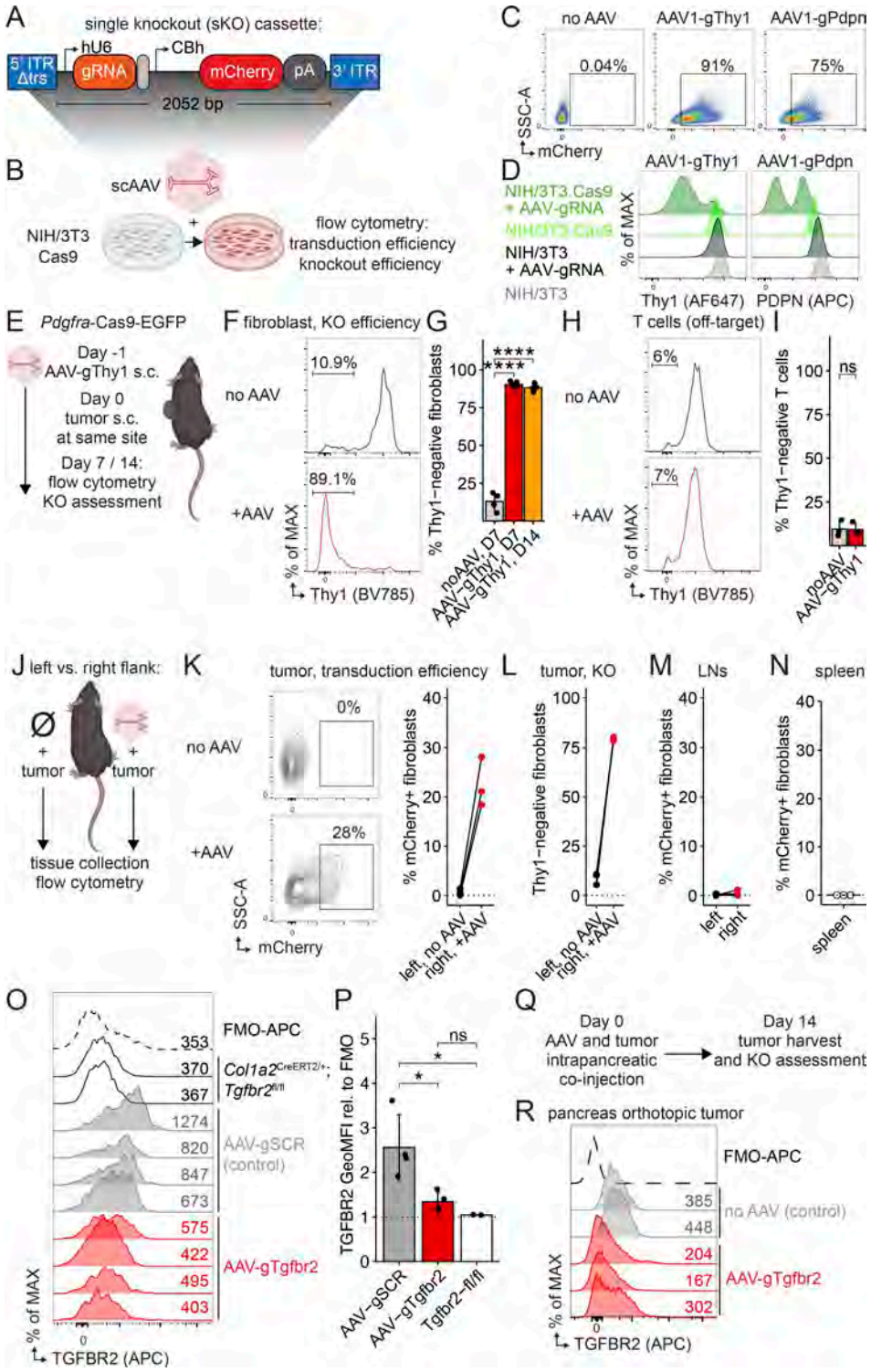

Figure 1. **Local *in vivo* gene KO in fibroblasts. (A)** scAAV cassette for single-gene KO (sKO). ITR, inverted terminal repeat; Δtrs, no terminal resolution site; CBh, chicken β-actin hybrid promoter; pA, SV40 late polyadenylation signal. **(B)** Experimental scheme for testing transduction and KO efficiency of scAAV *in vitro*. NIH/3T3.Cas9 cells were transduced with AAV1 at an MOI of 1e5. 72 h later, cells are analyzed via flow cytometry. **(C)** Flow cytometry plots showing mCherry expression in NIH/3T3.Cas9 cells after transduction with AAV as outlined in B. One of two representative experiments is shown. **(D)** Flow cytometry overlay plots of (left) Thy1 or of (right) PDPN protein surface expression in NIH/3T3 cells expressing Cas9 (green) or not (black) after transduction with AAV as outlined in B. Only Cas9-expressing NIH/3T3 cells exposed to AAV-gRNA lose surface expression of target protein. One of two representative experiments is shown. **(E)** Experimental scheme for gene KO in tumor fibroblasts using scAAV in mice challenged with 5e5 YUMM5.2 melanoma cells. **(F)** Representative histograms showing Thy1 surface expression analyzed by flow cytometry of all EGFP$^+$ tumor fibroblasts from mice treated as outlined in E and analyzed on day 7. One of two representative experiments is shown. **(G)** Quantification of KO efficiency in all EGFP$^+$ tumor fibroblasts on day 7 or 14 after tumor challenge (n = 4–6 mice/group, pooled from two experiments). **(H)** Same as (F) in CD45$^+$ CD3e$^+$ T cells. **(I)** Quantification of H on day 7 (n = 3/group). Significance was

tested using Welch's *t* test. **(J)** Experimental scheme for testing local KO in tumor fibroblasts of mice challenged with 5e5 YUMM5.2 melanoma cells. **(K)** Left: Representative flow cytometry plots showing mCherry expression as a readout for AAV transduction. Cells gated on EGFP$^+$ tumor fibroblasts. Right: Quantification of mCherry$^+$ EGFP$^+$ tumor fibroblasts in paired flank tumors from same mouse (n = 3 mice). **(L)** Quantification of Thy1 KO efficiency in all EGFP$^+$ fibroblasts from paired flank tumors on same mouse (n = 3 mice). **(M)** Quantification of mCherry expression in fibroblasts of brachial and inguinal LNs pooled from left or right flanks (n = 3 mice). **(N)** Quantification of mCherry expression in splenic fibroblasts after flank AAV injection (n = 3 mice). **(O)** Overlay histograms of TGFBR2 surface expression by flow cytometry on all tumor fibroblasts from mice treated with 3e10 vg AAV-gTgfbr2 or AAV-gSCR (control) as outlined in E. Tumor fibroblasts of *Col1a2*$^{CreERT2/+}$;*Tgfbr2*$^{fl/fl}$ mice treated with tamoxifen on five consecutive days prior to tumor engraftment (see Materials and methods for details on dose and application) were included as negative staining control. GeoMFI value listed for each sample. FMO, fluorescence minus one from *Pdgfra*-Cas9-EGFP mouse. One of two representative experiments is shown. **(P)** Quantification of TGFBR2 (GeoMFI) surface expression on all tumor fibroblasts from O relative to FMO (n = 2–4 mice/group). One of two representative experiments is shown. **(Q)** Experimental scheme for KO assessment in orthotopically transplanted pancreatic tumors. **(R)** Overlay histograms of TGFBR2 surface expression by flow cytometry on all tumor fibroblasts isolated from orthotopically grown HY19636 pancreatic tumors from *Pdgfra*-Cas9-EGFP mice after intrapancreatic co-injection of 3e10 vg AAV-gTgfbr2 and 2.5e5 HY19636 cells. GeoMFI values listed for each sample. One of two representative experiments is shown. All data are mean ± SD, and significance was tested using one-way ANOVA with Tukey's multiple comparisons test, unless otherwise noted. *P < 0.05 and ****P < 0.0001. fl, floxed; GeoMFI, geometric mean fluorescence intensity; SCR, scramble; ns, nonsignificant. MOI, multiplicity of infection.

~10% without AAV (Fig. 1, F and G). Targeted *Thy1* KO was stable in CAFs, as the same percentage of about 85% of all CAFs were still Thy1-negative when sampled 14 days after tumor challenge (Fig. 1 G), while the percentage of mCherry$^+$ CAFs expectedly decreased in the same timeframe (Fig. S1 K), due to the non-integrative, episomal AAV genome being lost over time in mitotic cells. When extending this analysis to T cells, another cell type in the TME besides CAFs that express Thy1, AAV-gThy1 injection in *Pdgfra*-Cas9-EGFP mice did not induce loss of surface Thy1 levels (Fig. 1, H and I), indicating targeted gene KO predominantly in CAFs. This efficient and persistent KO of a target gene in CAFs was consistent at higher doses of AAV (Fig. S1 L). To test if the KO was truly local, the same *Pdgfra*-Cas9-EGFP mouse was injected on only one flank s.c. with AAV-gThy1 but challenged with YUMM5.2 tumor on both flanks on the following day (Fig. 1 J). CAF transduction and *Thy1* KO were only detected in the tumor that was grown at the site of prior AAV-gThy1 injection (Fig. 1, K and L), not in tumor-draining LNs (Fig. 1 M) nor in the spleen (Fig. 1 N). This suggests that s.c. injection of AAV-gRNA allows local KO and limits systemic spread of AAV, minimizing KO at unintended locations.

As part of a goal to understand localized roles for specific genes in fibroblasts, we next generated AAV-gTgfbr2 to target the *Tgfbr2* gene in fibroblasts for KO (Fig. S1 M). AAV-gTgfbr2 decreased TGFBR2 levels on all CAFs in *Pdgfra*-Cas9-EGFP mice to similar levels as conventional *Col1a2*-CreERT2–mediated KO of the floxed *Tgfbr2* gene in *Col1a2*$^{CreERT2/wt}$;*Tgfbr2*$^{fl/fl}$ mice (Fig. 1, O and P), demonstrating that AAV-delivered gRNAs have an *in vivo* KO efficiency almost resembling conventional Cre/loxP-based approaches, without having to rely on lengthy mouse breeding to get to the desired genotype for experimental analysis. Instead, AAV-delivered gRNAs required only 2 wk of cloning and AAV generation until injection of AAV-gRNA for targeted, local KO of any gene of interest. This allows subsequent functional studies of any gene of interest expressed by CAFs via local gene KO.

To assess the KO efficiency of our AAV-based system at (A) a different site and (B) within a different setting, we (A) co-injected the pancreatic cancer cell line HY19636, which is derived from a mouse pancreatic ductal adenocarcinoma (PDAC) KPC mouse (*Kras*$^{LSL-G12D/+}$; *Trp53*$^{lox/+}$; *p48/Ptf1a*-Cre) (Yamamoto et al., 2020), together with AAV-gTgfbr2 orthotopically in the pancreas of *Pdgfra*-Cas9-EGFP mice (Fig. 1 Q); or (B) tested it in a skin fibrosis (Błyszczuk et al., 2019) model (Fig. S1 N). Fibroblasts isolated from orthotopically grown pancreatic tumors or in skin fibrosis also lost TGFBR2 surface expression when AAV-gTgfbr2 was co-injected (Fig. 1 R and Fig. S1 O), demonstrating the adaptability of this approach to different tissue sites and disease models.

Local *Osmr* or *Tgfbr2* KO in CAFs repolarizes them toward homeostatic state but differentially affects TREM2$^+$ tumor-associated macrophage phenotype

As a proof of concept and test of the specificity achievable with selective gene KOs, we set out to compare how blocking of a putatively pro-inflammatory gene program in CAFs via *Osmr* KO (Fig. S2, A–C) or blocking of a putatively pro-fibrotic gene program via *Tgfbr2* KO (Fig. 1 P) can affect the fibroblast cell states in growing YUMM5.2 melanoma or HY19636 pancreatic cancer tumors (Fig. 2 A). The HY19636 PDAC model represents a more desmoplastic tumor with high CAF involvement (Fig. S2 D). To assay changes in fibroblast identity, we initially measured surface markers that are typically indicative of different activity states: expression of SCA-I$^+$ Ly6C$^+$ are associated with homeostatic fibroblasts in skin (Buechler et al., 2021b), skin repair (Hu et al., 2023) (Fig. S2, E and F), and tumor growth (Krishnamurty et al., 2022) (Fig. S2, H and 2 I), whereas loss of SCA-I and Ly6C with concomitant upregulation of *Ncam1* marks activated fibroblasts in these settings (Fig. S2, G and J). We thus distinguished double-positive (DP) SCA-I$^+$ Ly6C$^+$, intermediate (Int), double-negative (DN) SCA-I$^-$ Ly6C$^-$, and DN NCAM1$^\pm$ CAF subsets (Fig. S2, K and L). We corroborated these cell states as defined by the aforementioned markers by measuring increased expression of homeostatic marker *Dpt* in the DP CAFs and, inversely, increased expression of *Acta2* and *Postn* in DN NCAM1$^+$ CAFs (Fig. S2 M). We also noted that DN CAFs had the highest expression of *Cthrc1*, a recently described marker of a pro-fibrotic fibroblast subset (Fig. S2, N and O) (Tsukui et al., 2020; Tsukui et al., 2024).

While homeostatic skin fibroblasts expectedly had mostly DP fibroblast and low NCAM1 activation-marker expression (Fig. 2 B), CAFs exhibited a more DN phenotype (Fig. 2 C), which was decreased in both AAV-gOsmr and AAV-Tgfbr2 groups when compared with controls (Fig. 2 D), suggesting that *Osmr* or *Tgfbr2*

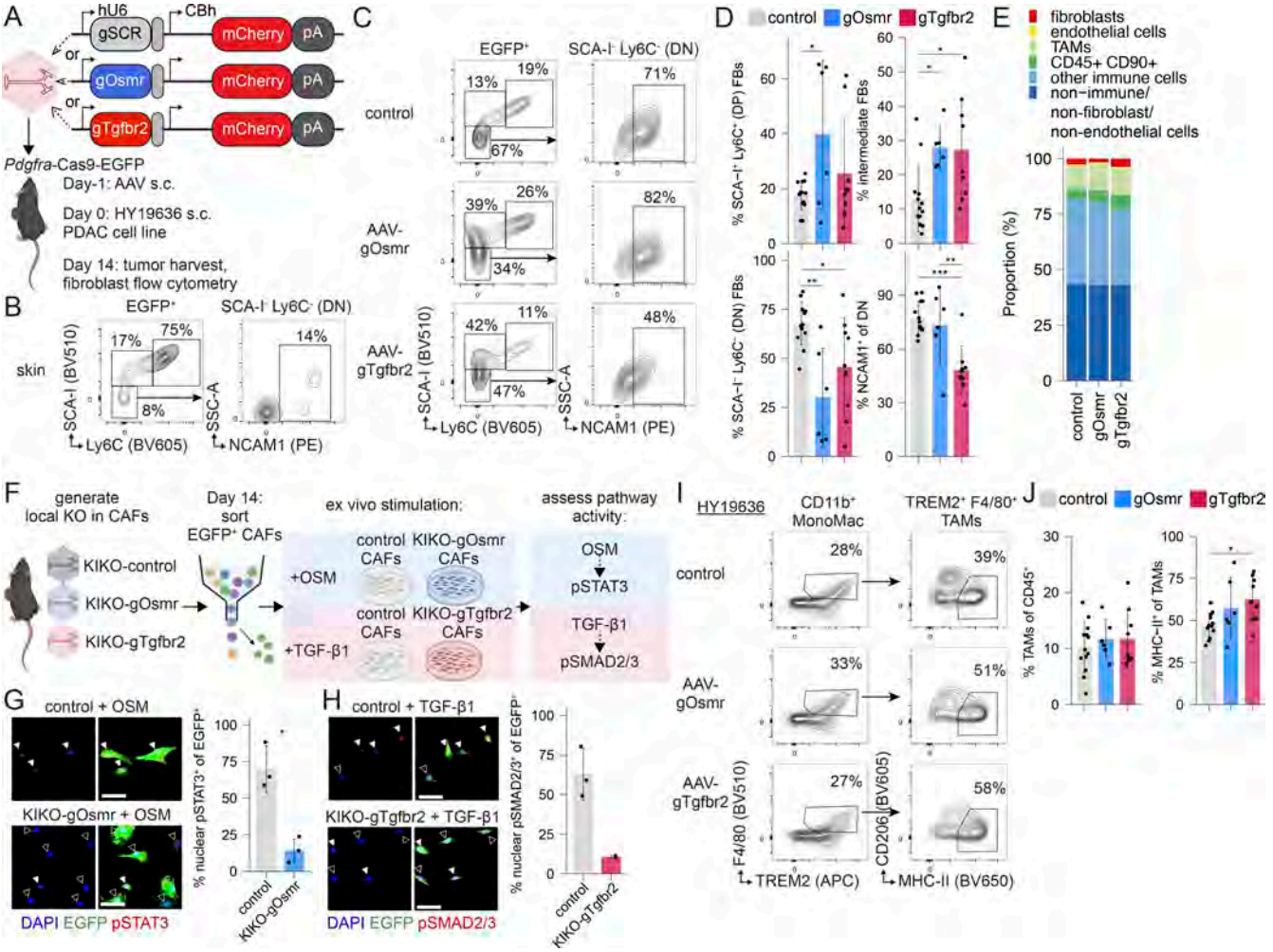

Figure 2. **Local *Osmr* or *Tgfbr2* KO in CAFs repolarizes them toward homeostatic state and subtly affects TREM2⁺ TAM MHC-II expression.** **(A)** Different AAV-gRNA cassettes used in outlined experiment for local KO in tumor fibroblasts. Each AAV-gRNA was injected s.c. in HY19636 pancreatic cancer model at a dose of 1–3e10 vg AAV in *Pdgfra*-Cre;*R26*-Cas9-EGFP$^{+/+}$ or *Pdgfra*-CreERT2$^{+/wt}$;*R26*-Cas9-EGFP$^{+/+}$ mice. **(B)** Flow cytometry plots of (left) EGFP⁺ skin fibroblasts from *Pdgfra*-Cas9-EGFP mice and (right) the DN SCA-I⁻ Ly6C⁻ subset. **(C)** Flow cytometry plots of (left) EGFP⁺ tumor fibroblasts and (right) DN tumor fibroblasts from control-, AAV-gOsmr, or AAV-gTgfbr2–injected *Pdgfra*-Cas9-EGFP mice on day 14 after HY19636 tumor challenge. **(D)** Quantification of C. **(E)** Stacked bar chart of main cell populations identified in tumors from C via flow cytometry plotted as proportion of all live cells. Mean values of n = 6–13 tumors/group, pooled from four independent experiments, are plotted. **(F)** Experimental scheme for *ex vivo* stimulation and analysis of CAFs isolated from *Pdgfra*-Cas9-EGFP mice challenged with HY19636 tumors and prior injection of AAV-KIKO-Thy1 (control), AAV-KIKO-Osmr, or AAV-KIKO-Tgfbr2. **(G)** Left: Representative immunofluorescence images of sorted EGFP⁺ CAFs from F stimulated with OSM. Cells were fixed and counterstained with DAPI prior to staining for pSTAT3. Filled arrowheads mark nuclear location of pSTAT3; open arrowheads mark absence of nuclear pSTAT3. Scale bar, 50 µm. Right: Quantification of EGFP⁺ CAFs with nuclear pSTAT3. Each dot represents CAFs sorted from one tumor (n = 3 tumors/group). Data are mean ± SD, and significance was tested using Welch's t test. **(H)** Left: Representative immunofluorescence images of sorted EGFP⁺ CAFs from F stimulated with TGF-β1. Cells were fixed and counterstained with DAPI prior to staining for pSMAD2/3. Filled arrowheads mark nuclear location of pSMAD2/3; open arrowheads mark absence of nuclear pSMAD2/3. Scale bar, 50 µm. Right: Quantification of EGFP⁺ CAFs with nuclear pSMAD2/3. Each dot represents CAFs sorted from one tumor (n = 2–3 tumors/group). **(I)** Representative flow cytometry plots of (left) CD11b⁺ MonoMacs and (right) F4/80⁺ TREM2⁺ TAMs from HY19636 tumors with *Osmr* or *Tgfbr2* KO in fibroblasts as outlined in A. **(J)** Quantification of F. Data represent three (B) or four (C and I) independent experiments. Data in D and J are mean ± SD, and significance was tested using one-way ANOVA with Tukey's multiple comparison test (n = 6–13 tumors/group, pooled from four independent experiments). CBh, chicken β-actin hybrid promoter; pA, polyadenylation signal; SCR, scramble; ns, nonsignificant. *P < 0.05, **P < 0.01, and ***P < 0.001.

KO in CAFs is sufficient to shift the subset balance away from the activated DN CAF population. *Tgfbr2* KO also decreased the frequency of the NCAM1⁺ DN population (Fig. 2 D). We did not observe a significant effect on tumor weight or fibroblast, endothelial, and immune cell numbers (Fig. 2 E and Fig. S3 A). These findings were replicated in the YUMM5.2 melanoma model (Fig. S3, B–D), demonstrating the robust adaptability of this local fibroblast gene editing tool to other settings.

For the control group, we decided to pool tumor samples that had received AAV with a scrambled gRNA sequence (gSCR) that does not recognize any sequence in the mouse (Suzuki et al., 2016); AAV with a gRNA targeting the T cell receptor α constant (*Trac*) locus—which is not expressed in fibroblasts and, thus, serves as a genome cutting control (Fig. S3 E); and samples that had received no AAV. These three control groups all showed no significant differences on measured fibroblast phenotypes

when compared with each other (Fig. S3 F) and so are presented as one "control" group for the rest of the study.

To confirm gene inactivation of *Osmr* and *Tgfbr2* in the targeted CAFs, we initially attempted to stably knockin (KI) mCherry in the *Osmr* or *Tgfbr2* locus, respectively, which would allow enrichment of knocked-out CAFs by sorting mCherry$^+$ cells and then use them for further studies to assess gene inactivation. We designed KI-KO (KIKO) AAV constructs that combine a U6-gRNA cassette to induce DNA double-strand breaks with a homology-directed repair template (HDRT) to KI genetic payloads into regions of interest in target cells (Fig. S3 G). The homology arms of the HDRT and the payload are designed to generate an in-frame KI of mCherry at the gOsmr or gTgfbr2 target sites, thereby disrupting endogenous *Osmr* or *Tgfbr2* expression (Fig. S3 H). *In vivo* KI efficiencies in CAFs of 3–12% and 18–45% were detected for targeting *Osmr* and *Tgfbr2*, respectively (Fig. S3 I). These differences in mCherry reporter expression between different gene targets potentially reflect differences in gene level expression after KIKO and/or differences in KI efficiencies of the HDRTs at their unique genomic loci.

To ascertain *Osmr* or *Tgfbr2* gene inactivation after *in vivo* gene editing, CAFs were sorted from HY19636 challenged *Pdgfra*-Cas9-EGFP mice that received AAV-KIKO-Osmr or AAV-KIKO-Tgfbr2 and were then exposed *ex vivo* to OSM (the primary ligand for OSMR in mice) or TGF-β1 (ligand for TGFBR2) to measure pathway activity in KIKO CAFs (Fig. 2 F). Here, all EGFP$^+$ CAFs were sorted, instead of just the mCherry$^+$ CAFs, to maximize cell yield. CAFs from AAV-KIKO-Thy1–treated mice served as controls. Decrease in nuclear location of pSTAT3 or pSMAD2/3 in KIKO-Osmr or KIKO-Tgfbr2 CAFs, respectively, upon stimulation demonstrated stable functional *in vivo* KO of *Osmr* or *Tgfbr2* (Fig. 2, G and H). Thus, AAV-based *in vivo* KO of target genes allows functional gene inactivation.

A benefit of engineering fibroblasts specifically in the TME is the ability to study the effect of their modification upon other local cells. Given the relationship between macrophages and fibroblasts in a multitude of tissue functions and pathology (Buechler et al., 2021a; Franklin, 2021), we sought to apply our method to understand modulation in tumor-associated macrophages (TAMs, gated as DAPI$^-$ CD45$^+$ Ly6G$^-$ CD90.2$^-$ B220$^-$ NK1.1$^-$ SiglecF$^-$ non-[CD64$^-$ CD24$^+$] CD11b$^+$ F4/80$^+$ TREM2$^+$) (Fig. S3 J). While TAMs did not change in their frequency within all immune cells, *Tgfbr2* KO in CAFs led to a slight but statistically significant increase in the frequency of those that expressed MHCII$^+$ (Fig. 2, I and J; and S3 K)—a phenotype associated with immunostimulatory myeloid cells (Kilian et al., 2023; Wang et al., 2011). This increase in MHCII$^+$ TAMs was reproduced in the YUMM5.2 model again without an increase in total intratumoral CD90$^+$ lymphocytes or monocyte/macrophages (Macs) (Fig. S3, L–N). These findings highlight the utility of modulating genes of interest in CAFs to induce changes in their phenotype, with secondary effects on other cells of the TME, such as TAMs.

Extending the analysis of CAF pathway perturbations beyond OSM and TGFβ signaling, we tested how *Il1r1* KO in CAFs (Fig. S3, O and P) in the PDAC model affects their subset polarization because IL-1 pathway activity in CAFs has been shown to promote disease progression (Koncina et al., 2023; Nicolas et al., 2022). Here, we found no changes compared with control (Fig. S3 Q), as well as no changes when measuring TAM frequencies in the tumor, although MHCII$^+$ TAMs were again more abundant in CAF *Il1r1* KO tumors (Fig. S3 R). Thus, *Osmr*, *Tgfbr2*, or *Il1r1* KO in CAFs repolarizes CAFs differently, prompting us to investigate those differences and their effect on the networks of gene expression in the TME in more detail.

Local *Tgfbr2* KO in CAFs reveals emergence of unique *Col18a1*^{hi} CAF cell state

To study the effect of *Osmr*, *Tgfbr2*, or *Il1r1* KO in CAFs on a transcriptional level and to capture its effect on other cells of the TME, immune, stromal, and tumor cells of s.c. grown KPC tumors were collected for single-cell RNA-sequencing (scRNA-seq) analysis after targeted, local KO by AAV in *Pdgfra*-Cas9-EGFP mice (Fig. 3A and Fig. S4 A). A total of 115,637 high-quality cells were captured from a total of 16 tumors (n = 4 per AAV-gRNA group), covering all major cell populations in the TME: neutrophils, MonoMacs, dendritic cells (DCs), mast cells, T cells, natural killer (NK) cells, endothelial cells, pericytes, and fibroblasts (Fig. S4, B–D).

Sub-clustering of the CAF compartment revealed eight different subsets (Fig. 3, B and C; and Table S1). Homeostatic fibroblasts expressed *Pi16*, *Ly6c1*, and *Ly6a*, genes associated with "universal" fibroblasts (Fig. S2 K); inflammatory CAFs expressed *Il6*, *Lif*, and *Saa3*, genes previously described in pro-inflammatory settings (Öhlund et al., 2017; Tsukui et al., 2024); myofibroblastic CAFs (myCAFs) were characterized by myofibroblast-associated genes, such as *Acta2*, *Lrrc15*, and *Ncam1* (Dominguez et al., 2020; Hinz et al., 2001; Ye et al., 2024) and could be further subdivided into four groups based on proliferative markers (*Mki67*; myCAF_prolif), *Slit1* and *Fabp5* (myCAF_2), or *Wif1* and *Lamc3* (myCAF_3). The Int cluster harbored genes of both homeostatic and inflammatory fibroblasts, whereas the Col18a1 cluster was named after one of its most differentially expressed gene (DEG), *Col18a1*, and noticeably has low expression of the other homeostatic, inflammatory, or myofibroblast-defining genes (Fig. 3 C).

The Col18a1 cluster was only present in the AAV-gTgfbr2 group (Fig. 3 D) and represented the most abundant CAF subset within those samples at about one half of all AAV-gTgfbr2 CAFs (Fig. 3 E). Conversely, *Tgfbr2* KO in CAFs leads to a decrease in all myCAF subsets (Fig. 3 E). This could be explained by the lack of a recently published fibroblast TGF-β1 response signature specifically in AAV-gTgfbr2 CAFs (Fig. S4 E), a prominent driver of myofibroblast differentiation (Mariathasan et al., 2018). To assess if the emergence of the *Col18a1*-expressing CAFs in the mouse PDAC model was unique to our AAV-based *Tgfbr2* KO, we re-analyzed a published mouse PDAC scRNA-seq data set using conditional *Tgfbr2* KO in universal fibroblasts (Krishnamurty et al., 2022) and found that a population with the Col18a1 CAF cluster signature can also be identified specifically when *Tgfbr2* was knocked out using Cre/LoxP-based mouse genetics (Fig. S4 F), demonstrating the methodological robustness of using AAV-gRNA or Cre/LoxP-based gene KOs.

To gain a better understanding of how *Osmr*, *Tgfbr2*, or *Il1r1* KO affects CAF transcriptional polarization, we compared the overlap of DEG lists from each KO group and noticed that the

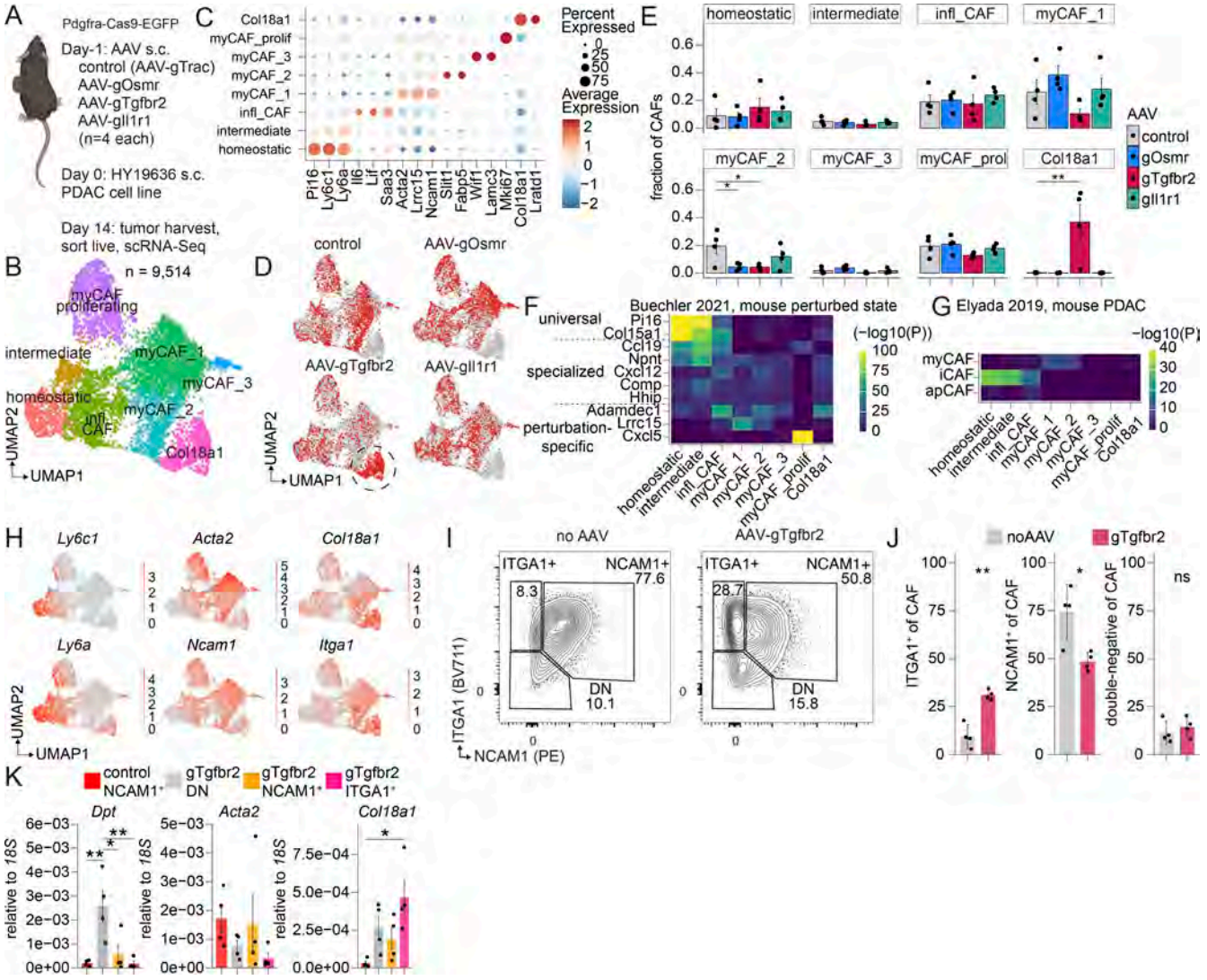

Figure 3. **Local *Tgfbr2* KO in CAFs reveals emergence of unique *Col18a1*^{hi} CAF cell state. (A)** Experimental layout. **(B)** Uniform manifold approximation and projection (UMAP) of CAF subsets. **(C)** Marker gene expression of identified CAF subsets. **(D)** UMAP of CAFs highlighted by AAV-gRNA condition. **(E)** Bar charts of frequency of CAF subsets (scRNA-seq) as a fraction of all fibroblasts by AAV-gRNA condition plotted as mean ± SEM (n = 4 per group). *P < 0.05 one-way ANOVA with Dunnett's multiple comparison test. **(F and G)** Similarity of DEGs between CAF subsets (columns) and (F) mouse fibroblasts in perturbed states by Buechler et al. (2021b) (rows) or (G) mouse PDAC CAF subsets by Elyada et al. (2019). Statistical significance of DEG overlap (−log10 [P value], hypergeometric test, P value adjusted using Bonferroni correction) for each pairwise comparison is plotted as heatmap. Yellow indicates high statistically significant overlap of DEG lists. **(H)** UMAP visualization of select genes (homeostatic *Ly6c1* and *Ly6a*; myofibroblast-associated *Acta2* and *Ncam1*; AAV-gTgfbr2–associated *Col18a1* and *Itga1*) in CAFs. **(I)** Flow cytometry contour plots of tumor fibroblasts on day 14 after 2.5e5 HY19636 s.c. cell injection in *Pdgfra*-Cas9-EGFP mice with or without 1e10 vg AAV-gTgfbr2 injection on day −1. ITGA1$^+$ NCAM1$^-$ gate (top left) highlights AAV-gTgfbr2–specific CAF population. One of three representative experiments is shown. **(J)** Quantification of I. Data are mean ± SD, and significance was tested using Welch's t test (n = 4/group). One of two representative experiments is shown. *P < 0.05, **P < 0.01, and ns, nonsignificant. **(K)** Gene expression of CAFs sorted as in I analyzed by quantitative real-time PCR. Data are mean ± SEM (n = 4 tumors/group), and significance was tested using one-way ANOVA with Tukey's multiple comparison test.

majority of DEGs were unique to their respective KO group (Fig. S4, G and H; and Table S2). For example, AAV-gOsmr and AAV-gTgfbr2 only shared 20 and 24 genes that were up or down-regulated, respectively, when compared with the unperturbed control CAFs (Fig. S4 H). Gene set enrichment analysis (GSEA) revealed that AAV-gOsmr CAFs were enriched for inflammatory response genes (*Ifitm1*, *Il1a*, *Irf1*, *Lyn*, and *P2rx4*), but depleted of hypoxia-related genes that are involved in carbohydrate metabolic processes (*Slc2a1*, *Pfkl*, *Pdk1*, and *Gys1*), whereas AAV-gTgfbr2 CAFs were enriched for hypoxia-related (*Ndrg1*, *S100a3*) and glycolytic genes (*Pgk1*, *Ldha*, and *Ugp2*) but depleted of epithelial-to-mesenchymal transition genes (*Acta2*, *Tagln*, *Lrrc15*, and *Ccn1*) (Fig. S4, I and J), a known consequence of absent TGFBR2 signaling in fibroblasts (Buechler et al., 2021b; Elyada et al., 2019; Hinz et al., 2001). Together, these results demonstrate that the AAV-mediated KO of individual receptors can induce distinct transcriptional changes in CAFs.

With the Col18a1 cluster uniquely emerging in the AAV-gTgfbr2 condition and it not being characterized by homeostatic, inflammatory, or myofibroblastic gene signatures, we also

compared its transcriptional profile with published mouse scRNA-seq fibroblast data sets (Buechler et al., 2021b; Elyada et al., 2019). As expected, the DEGs of the homeostatic and Int clusters had the most overlap with the *Pi16*$^+$ and *Col15a1*$^+$ homeostatic/universal state; the inflammatory CAF cluster had the most overlap with the colitis-associated *Adamdec1*$^+$ state, and the myCAF_1 and myCAF_2 clusters were most similar to *Lrrc15*$^+$ myofibroblasts (Fig. 3 F) and PDAC myCAFs (Fig. 3 G). However, the Col18a1 cluster did not uniquely map to any previously identified mouse fibroblast states (Fig. 3, F and G). Even when comparing the Col18a1 gene signature with published human fibroblast profiles (Gao et al., 2024; Hwang et al., 2022), the Col18a1 cluster did not have the highest overlap with any identified human fibroblast subset (Fig. S4, K–M), further suggesting that *Tgfbr2* KO CAFs adopt a unique transcriptional cell state.

The myCAF_1 cluster exhibited the highest similarity with human PDAC myofibroblasts and non-small cell lung cancer FAP$^+$ CAFs (Fig. S4, K and L), suggesting it is correct to refer to these as myofibroblasts. While the myCAF_2 cluster had some similarity with human PDAC myofibroblasts, they also shared transcriptional similarity with previously described inflammatory, "stress-associated" HSPA6 fibroblasts (Fig. S4 M). The myCAF_3 cluster, which emerged in the AAV-gOsmr condition (Fig. 3 E), was also most similar to stress-associated HSPA6 fibroblasts (Fig. S4 M). In summary, the myCAF_1 cluster transcriptionally resembles myCAFs, whereas the myCAF_2 and myCAF_3 clusters exhibit more mixed transcriptional phenotypes of inflammatory and myofibroblastic states.

To identify the Col18a1 CAFs orthogonally via flow cytometry, we identified surface expressed proteins that were transcriptionally expressed at high levels within the Col18a1 cluster. While *Itga1* (encoding integrin α 1/ITGA1) was not exclusively expressed in the Col18a1 cluster (Fig. 3 H), when combining ITGA1 staining with SCA-I, Ly6C, and NCAM1, we identified a ITGA1$^+$ NCAM1$^-$ CAF population that specifically emerged in AAV-gTgfbr2 tumors (Fig. 3, I and J) and was low for the homeostatic markers SCA-I and Ly6C (Fig. S4 N). qPCR analysis of sorted CAF populations based on NCAM1 and ITGA1 markers further validated their usefulness in identifying CAFs expressing homeostasis-associated gene *Dpt* (ITGA1$^-$ NCAM1$^-$ DN), myofibroblast-associated *Acta2* (ITGA1$^-$ NCAM1$^+$), and *Col18a1* (ITGA1$^+$ NCAM1$^-$) (Fig. 3 K).

Tgfbr2 KO-induced *Col18a1*^{hi} CAFs are distinct from iCAFs and myCAFs and correlate with worse survival in human pancreatic cancer patients

The emergence of the *Col18a1*^{hi} CAF state prompted us to investigate the possibility that local *Tgfbr2* KO in fibroblasts during tumor growth led to the polarization of a distinct CAF cell state. *In silico* pseudotime-based trajectory analysis using Monocle 3 (Cao et al., 2019) of all captured CAFs, sans proliferating myCAFs, placed Col18a1 CAFs at the end of the trajectory (Fig. 4 A). The analysis suggested that CAFs, in the setting of *Tgfbr2* KO, progressed from homeostatic to inflammatory through the myCAF cell state until they eventually arrived at the Col18a1 cell state (Fig. 4 B). This progression along the pseudotime axis was characterized by a loss of the universal marker *Pi16* and sequential emergence of inflammatory markers *Saa3* and *Cthrc1*, prior to upregulation of myofibroblast markers *Lrrc15*, *Acta2*, and *Ncam1*, which then were lost when the Col18a1 state was reached (Fig. S5 A).

By focusing on the AAV-gTgfbr2 fibroblast object only, which predominantly contains the *Col18a1*^{hi} subset but also homeostatic, inflammatory CAFs, myCAF_1, and myCAF_2 subsets (Fig. 3 E), we noticed a branchpoint in cell trajectory (Fig. S5 B) that separated the homeostatic and inflammatory CAFs (pre-branchpoint) from the myCAF_1 subset (branch 1) and *Col18a1*^{hi} subset (branch 2) (Fig. S5, C and D). Differential gene expression comparing the pre-branchpoint versus branch 1 or branch 2 (Fig. S5, E and F) revealed increased expression of AP-1 transcription factors (*Fos*, *Fosb*, *Jun*, and *Junb)* in cells along branch 2 (*Col18a1*^{hi} subset), which inversely decreased in expression along branch 1 (myCAF_1 subset) (Fig. S5 G). AP-1 transcription factors have been shown to interact with and cross-regulate Smad3/Smad4 proteins from the TGF-β signaling pathway (Massagué and Chen, 2000), suggesting that in this context of *Tgfbr2* KO in CAFs, the *Col18a1*^{hi} CAF subset emerges because of aberrant transcriptional regulation.

With the Col18a1 cluster not previously classified, we therefore identified *de novo* signatures across all identified CAF states using nonnegative matrix factorization (NMF) (Stein-O'Brien et al., 2018). This approach allows non-cluster–based analysis of transcriptional cell states by decomposing the cell-by-gene scRNA-seq count matrix into two smaller matrices, where one matrix represents the factors, i.e., groupings of co-expressed genes, and the other matrix represents the expression of those individual factors across each cell. Especially for cell populations with mixed cell states or without clearly defined subsets, such as fibroblasts, this approach can uncover heterogeneous gene expression patterns that are masked by clustering analysis.

We identified a total of 18 different factors within the CAF population (Fig. S5 H and Table S3). While most averaged factor weights did not differ between the AAV-gRNA groups, factor 6 and factor 9 were elevated in AAV-gTgfbr2 CAFs, and factor 14 was elevated in the AAV-gOsmr CAFs (Fig. S5 I). Correlation of factor weights across all CAFs further revealed that there were three major groupings of gene factors: (1) factors 7 and 13 that were enriched in inflammatory CAFs; (2) the factors 5, 11, and 14 that were enriched in myCAFs; (3) and the AAV-gTgfbr2–enriched factors 6 and 9 (Fig. 4, C and D). Noticeably, the inflammatory factors 7 and 13 were anticorrelated with both other groupings, suggesting that the inflammatory cell state is mutually exclusive with other CAF cell states detected here. CAFs within the Col18a1 cluster were enriched for factors 6 and 9 (Fig. 4 E), which were identified as gene signatures of various developmental states (factor_6) and ossification/osteoblast differentiation (*Fzd1*, *Pth1r*, and *Spp1*) (factor_9) (Fig. 4 F and Table S3). With osteoblasts representing a unique mesenchymal lineage within the bone tissue (Zhu et al., 2024), we speculated whether a *Tgfbr2* KO in CAFs reprograms them to an osteoblast-like cell. However, comparison of Col18a1 DEGs with a recently published mouse bone marrow stromal cell atlas (Baryawno et al., 2019) did not suggest that the Col18a1 cluster adopted a specific bone marrow stroma program (Fig. S5 J). This suggested

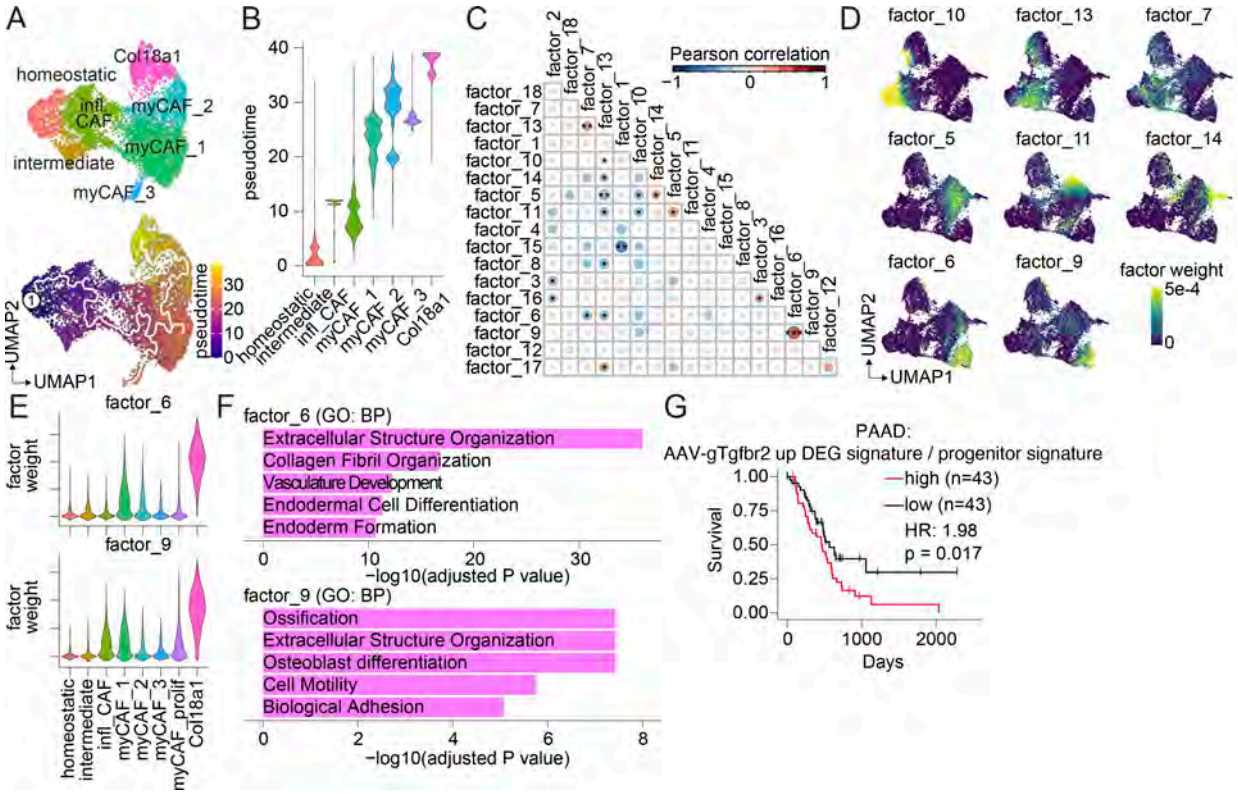

Figure 4. ***Tgfbr2* KO-induced *Col18a1*^{hi} CAFs are distinct from iCAFs and myCAFs and correlate with worse survival in human pancreatic cancer patients. (A)** UMAP of (top) CAF subsets without myCAF_prolif subset and (bottom) pseudotime trajectory starting at the homeostatic fibroblast subset and ending at cluster myCAF_3 or Col18a1. **(B)** Violin plot of CAF subsets plotted according to their distribution in pseudotime. **(C)** Pairwise Pearson correlation coefficient of CAF NMF factor expression across all CAFs. Rows and columns are ordered by hierarchical clustering. **(D)** UMAP visualization of select NMF factor expression in CAFs. **(E)** Violin plots of (top) NMF factor_6 and (bottom) NMF factor_9 expression in the CAF subsets. **(F)** Enriched gene sets (Gene Ontology: biological process [BP]) based on top contributing genes in (top) NMF factor_6 and (bottom) NMF factor_9. **(G)** Kaplan–Meier survival plot of PAAD patients from TCGA excluding PNET (pancreatic neuroendocrine tumor) diagnosed patients categorized into upper and lower quartiles by the ratio of "AAV-gTgfbr2 up" DEG signature to the fibroblast progenitor signature (see Materials and methods for details). The mouse-derived AAV-gTgfbr2 up DEG signature was generated using human orthologs. Hazard ratio (HR) and P value of Cox regression fit are shown. UMAP, uniform manifold approximation and projection.

that the AAV-gTgfbr2–induced CAFs harbored a cell state that is distinct of myofibroblasts, homeostatic, and inflammatory CAFs, instead presenting as a mix of ECM-producing CAFs with an osteoblast-like gene signature.

While both a high stromal gene signature (Combes et al., 2022) and a high fibroblast TGF-β1 response signature (Mariathasan et al., 2018) in human cancers are associated with worse survival (Fig. S5, K and L), we were curious how signatures derived from the DEGs from AAV-gRNA CAFs would associate with survival in pancreatic adenocarcinoma (PAAD) patients in the TCGA cohort (excluding pancreatic neuroendocrine tumor patients). To identify genes for inclusion in DEG-based signatures, we applied the following four steps (more details in Materials and methods): (1) the upregulated DEGs from the pseudobulk analysis of CAFs were selected for each AAV-gRNA group (Table S2); (2) the mouse genes were transferred to their human orthologs; (3) genes were kept if they were expressed most highly in fibroblasts or stellate cells (resident fibroblasts of the pancreas) in human pancreatic cancer scRNA-seq data sets (Tyler et al., 2025); (4) genes were excluded if they were shared between >1 AAV-gRNA group (Table S4). By categorizing PAAD patients based on the ratio of the AAV-gRNA DEG signature to a progenitor signature, we found that a high "AAV-gTgfbr2 up DEG signature/progenitor signature" ratio was associated with worse survival in PAAD, reaching a significant hazard ratio of 1.98 (P = 0.0175) (Fig. 4 G). Notably, survival analysis using the AAV-gOsmr, AAV-gIl1r1, or the TGF-β response signature did not yield significant differences in survival of PAAD patients (Fig. S5 M). Together, this suggests that a relative increase of the AAV-gTgfbr2–induced CAF cell state compared with progenitor fibroblasts, characterized by an osteoblast-like gene signature, is pro-tumorigenic in PAAD.

Tgfbr2 KO-induced *Col18a1*^{hi} CAFs recruit Siglec-F^{hi} neutrophils via high *Cxcl5* expression

To gain a better understanding of how the AAV-gTgfbr2–induced *Col18a1*^{hi} CAFs interact with their TME, the percentage of all identified major immune cell subsets (Fig. S5, N–Q) were correlated across all samples (Fig. 5 A). This revealed several cell networks, with Col18a1 CAFs positively correlating with two populations: the TAM.Ndrg1 subset and the neutrophil.4 subset. The neutrophil.4 subset was most abundant in AAV-gTgfbr2 tumors (Fig. 5B) and characterized by high *Siglecf* expression (Fig. 5C). The TAM.Ndrg1 subset had elevated MHC-II gene (*H2-Ab1*, *H2-Aa*, and *H2-Eb1*) expression in AAV-gTgfbr2 tumors

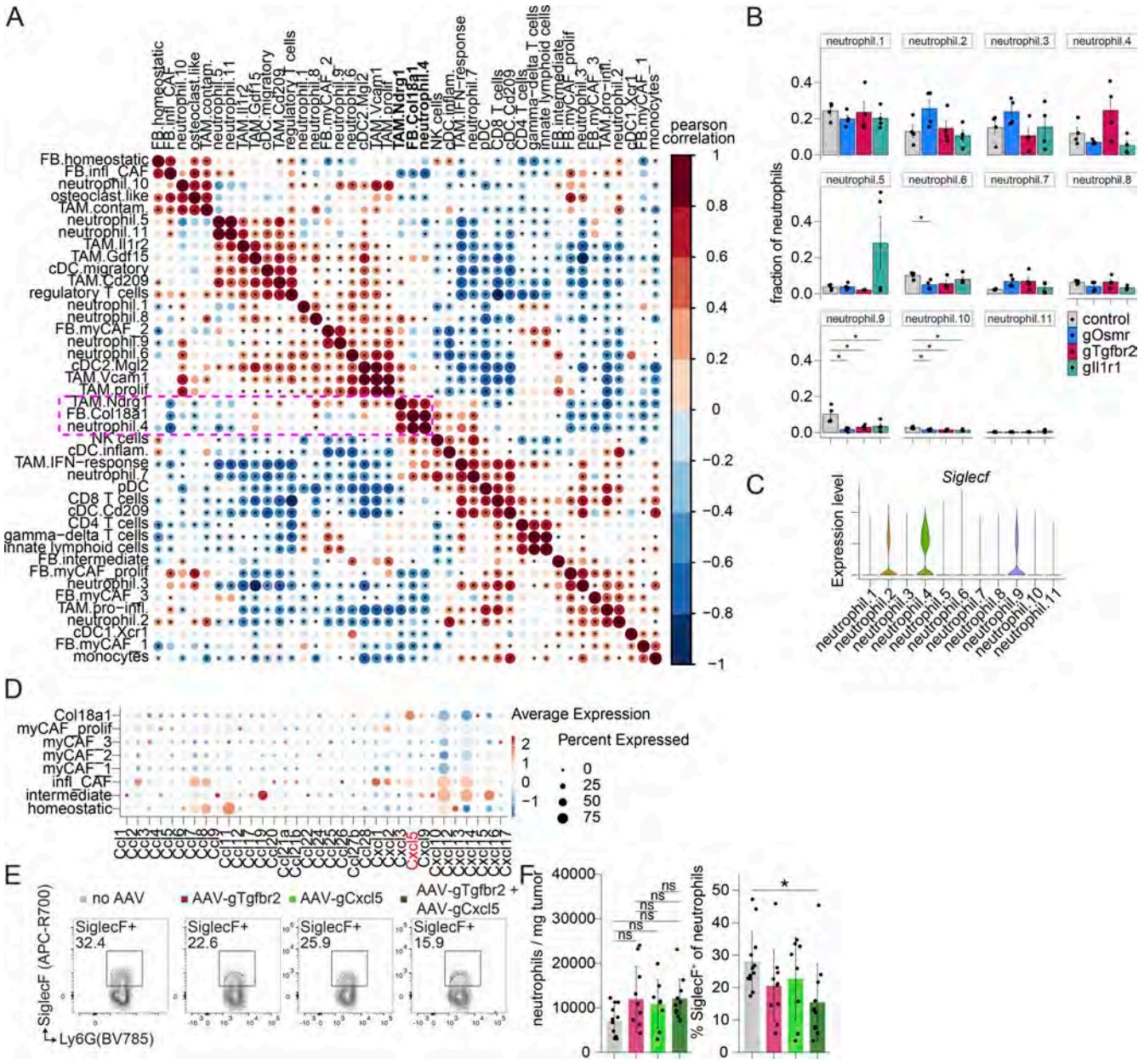

Figure 5. ***Tgfbr2* KO-induced *Col18a1*^{hi} CAFs recruit Siglec-F^{hi} neutrophils via high *Cxcl5* expression. (A)** Heatmap showing the pairwise Pearson correlation of cell type frequencies among AAV-gRNA samples. Box highlights grouping of Col18a1 CAF-associated cell types. *P < 0.05. **(B)** Bar charts of frequency of neutrophil subsets (scRNA-seq) as a fraction of all neutrophils by AAV-gRNA condition plotted as mean ± SEM (n = 4 per group). *P < 0.05 one-way ANOVA with Dunnett's multiple comparison test. **(C)** Violin plot of *Siglecf* expression among all neutrophil subsets. **(D)** Bubble plot of scaled expression of all detected *Ccl* and *Cxcl* genes in all CAF subsets. *Cxcl5* highlighted in red as most highly expressed in Col18a1 cluster. **(E)** Flow cytometry contour plots of DAPI$^-$ CD45$^+$ CD11b$^+$ Ly6G$^+$ neutrophils on day 14 after 2.5e5 HY19636 s.c. cell injection in *Pdgfra*-Cas9-EGFP mice with single or combinatorial 1e10 vg AAV-gRNA injection on day −1. **(F)** Quantification of E: (left) total neutrophil numbers normalized by tumor weight and (right) percentage of Siglec-F$^+$ neutrophils among all neutrophils. Data are mean ± SD, and significance was tested using one-way ANOVA with Tukey's multiple comparison test (n = 10–12 tumors/group, pooled from four independent experiments). *P < 0.05; ns, nonsignificant.

(Fig. S5 R), mirroring our previous findings of increased MHCII$^+$ TAMs, as analyzed by flow cytometry (Fig. 2 J).

To discover whether *Col18a1*^{hi} CAFs mediated recruitment of the neutrophil.4 subset, we analyzed transcriptional expression of all detected CCL/CXCL chemokine family members in the CAF subsets and noted the elevated expression of *Cxcl5* in *Col18a1*^{hi} CAFs (Fig. 5 D), a chemokine binding to the constitutively expressed chemokine receptor CXCR2 on neutrophils (Griffith et al., 2014). Cancer cell–derived CXCL5 has been described to promote neutrophil infiltration into tumors (Zhou et al., 2014), with *Tgfbr2* deletion in breast cancer cells resulting in increased CXCL5 production (Yang et al., 2008). To test if *Cxcl5* expression in AAV-gTgfbr2–induced *Col18a1*^{hi} CAFs is recruiting the neutrophil.4 subset to the PDAC TME, we used Siglec-F staining as a marker for the neutrophil.4 cluster (Fig. 5 C) and employed combinatorial AAV-gRNA administration (AAV-gCxcl5

plus AAV-gTgfbr2) to KO *Cxcl5* together with *Tgfbr2* in CAFs (Fig. S5 S). While Siglec-F staining and analysis by flow cytometry did not show a significant increase of Siglec-F$^+$ neutrophils in AAV-gTgfbr2 tumors, dual *Cxcl5* and *Tgfbr2* KO locally in CAFs via combinatorial AAV-Tgfbr2 plus AAV-gCxcl5 delivery did reduce Siglec-F$^+$ neutrophil accumulation in the TME (Fig. 5, E and F), implying that CAF-derived CXCL5 contributes to Siglec-F$^+$ neutrophil accumulation in PDAC tumors.

Combinatorial KO shows that emergence of *Tgfbr2* KO-induced *Col18a1*^{hi} CAFs is dependent on TNFR1 and canonical Wnt signaling

Finally, to nominate pathways that could potentially positively amplify the generation of the osteoblast-like AAV-gTgfbr2–initiated *Col18a1*^{hi} CAF subset, we used two computational approaches: ligand–receptor analysis using CellChat (Jin et al., 2021) and transcription factor activity inference using decoupleR (Badia-I-Mompel et al., 2022).

Ligand–receptor-based analysis using CellChat to identify potential signaling pathways between the Col18a1 CAF cluster and the TAM.Ndrg1 cluster, as well as the neutrophil.4 cluster, nominated TNF-TNFR1 (*Tnf*-to-*Tnfrsf1a*) signaling as a major contributor to the Col18a1 CAF cell state (Fig. 6 A). Both the TAM.Ndrg1 and the neutrophil.4 clusters were most abundant in AAV-gTgfbr2 tumors (Fig. 6 B) and were transcriptionally enriched for the GO hallmark term "TNFa signaling via NFkB" (Fig. 6 C), suggesting that they, together with the Col18a1 CAFs, exist in a TME with high TNFα signaling. Thus, we hypothesized that TNFR1-mediated signaling in AAV-gTgfbr2 CAFs mediates the emergence of the Col18a1/factor 9 osteoblast-like cell state (Fig. 4 F).

For transcription factor activity inference, we focused on osteoblast-associated transcription factors (Zhu et al., 2024) because NMF gene program analysis revealed that the Col18a1 cluster was enriched for osteoblast-related genes (Fig. 4 F). *Ctnnb1* and *Lef1*—two regulators of the Wnt pathway—were nominated as highly active in Col18a1 and all myCAF subsets (Fig. 6 D). This prompted us to hypothesize that Wnt pathway activity—a known contributor to the myofibroblast phenotype in cancer (Mosa et al., 2020) and skin fibrosis (Akhmetshina et al., 2012)—in the context of TGFBR2 signaling loss, produces the Col18a1 osteoblast-like CAF phenotype. To test the contributions of TNFR1 or Wnt pathway signaling in CAFs, we generated AAV-gTnfrsf1a and AAV-gCtnnb1 (Fig. S5, T and U) and found that combinatorial KO of *Tgfbr2* with *Tnfrsf1a* or *Ctnnb1* in CAFs (Fig. S5, V and W) decreased the ITGA1$^+$ NCAM1$^-$ CAF population compared to AAV-gTgfbr2 alone (Fig. 6, E and F), indicating that both pathways are contributing to ITGA1$^+$ Col18a1 CAF cluster generation. Furthermore, AAV-gCtnnb1 alone decreased the myofibroblast NCAM1$^+$ population to similar levels as AAV-gTgfbr2, while simultaneously maintaining the ITGA1$^-$ NCAM1$^-$ DN, homeostatic-like CAF population (Fig. 6, E and F).

Using AAV-gRNA–mediated KOs in fibroblasts, we present an experimental toolbox that allows local *in vivo* gene editing of fibroblasts to study gene functions—both on an individual as well as on a combinatorial level—in the context of mouse tumor models.

Discussion

The modularity of the localized *in vivo* CAF gene editing approach presented here—relying only on delivering a gRNA packaged in an AAV and conditional Cas9 expression in PDGFRA$^+$ fibroblasts—allows customizable, user-defined investigation of individual or combinatorial gene perturbations, while the local application allows spatially confined perturbations that limit potentially confounding effects induced by systemic gene perturbations, such as conventional Cre-loxP–based mouse models. We believe this approach will be beneficial to the advancement of understanding the complexity of fibroblast biology within different disease settings, as gene candidates can be more quickly and cost-effectively evaluated by not fully relying on complex mouse breeding to generate genetically engineered single or multiple KO mouse strains.

Previous to our study, AAV-mediated gene delivery in fibroblasts has been demonstrated *in vivo*, resulting in transient target gene expression from a classically introduced promoter (Francisco et al., 2021; Rezvani et al., 2016; Song et al., 2016). However, our study goes further in achieving true genome editing, plus improving selectivity for fibroblast lineages as well as the local environment. As an alternative approach to our CRISPR/Cas9 method, another recent study reported the knockdown of a target in fibroblasts *in vivo* using shRNA (Rajendran et al., 2023). While this will be beneficial in situations when Cas9 expression cannot be achieved in the target cell population, downregulation of mRNA in this method is transient, whereas CRISPR/Cas9-mediated KO allows sustained gene KO and more long-term analysis of gene perturbations—we observed stable KO of up to 14 days in the tumor fibroblast population (Fig. 1). Generating a sustained gene KO is especially valuable when studying long-term processes, excluding confounding effects via residual gene expression in knockdown scenarios. Additionally, the AAV-mediated gene delivery in fibroblasts allows editing in adult animals of genes that can cause embryonic lethality when knocked out constitutively.

Importantly, transduction of fibroblasts with a non-cutting gRNA (gSCR) or a gRNA cutting an irrelevant, non-expressed gene (gTrac) *in vivo* did not affect polarization of the SCA-I$^+$ Ly6C$^+$ states noticeably compared with non-transduced fibroblasts (Fig. S3 F). This indicated that at least in the context of tumor growth, the use of AAV1-serotyped scAAV does not affect fibroblast biology on its own and can be considered a fairly innocuous transduction method (Shirley et al., 2020) that does not mask effects of targeted gene KO.

One clear opportunity afforded here is the possibility of sculpting fibroblasts through a series of edits. Fibroblasts receive a multitude of signaling input during tumor growth, as demonstrated by their expression of different receptor families, as well as their transcriptional and functional polarization when receiving these signals (Biffi et al., 2019; Dominguez et al., 2020; Plikus et al., 2021; Wu et al., 2021). Sequential gene edits via subsequent injection of multiple sKO-AAVs or simultaneous edits via co-injection of multiple sKO-AAVs allow uncovering of redundant, synergistic, compensatory, or agonistic effects of gene functions in CAF biology. For example, inflammatory and myofibroblast CAF states have been described as two distinct fates fibroblasts can adopt in PDAC (Biffi et al., 2019;

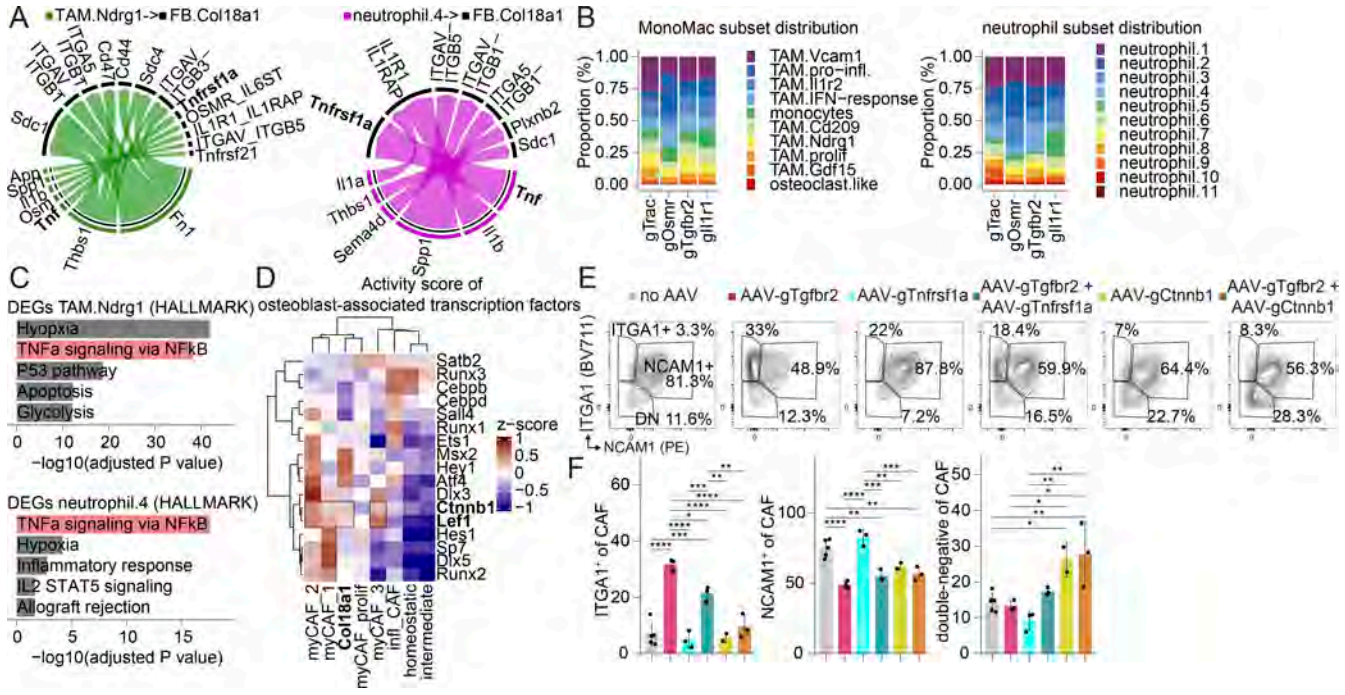

Figure 6. **Combinatorial KO shows that emergence of *Tgfbr2* KO-induced *Col18a1*^{hi} CAFs is dependent on TNFR1 and canonical Wnt signaling.** **(A)** Chord diagrams of ligand–receptor pairs between (left) TAM.Ndrg1 cells (senders) and Col18a1 CAFs (receivers) or (right) neutrophil.4 subset (senders) and Col18a1 CAFs (receivers). *Tnf*/*Tnfrsf1a* ligand–receptor pairing highlighted as bold. **(B)** Left: Proportion of MonoMac subsets (scRNA-seq) in each AAV-gRNA group. Right: Proportion of neutrophil subsets (scRNA-seq) in each AAV-gRNA group. **(C)** Top: Enriched gene sets (Gene Ontology hallmark) based on DEGs from TAM.Ndrg1 cluster. Bottom: Enriched gene sets (Gene Ontology hallmark) based on DEGs from neutrophil.4 cluster. **(D)** Heatmap of average activity score calculated by PROGENy (Badia-I-Mompel et al., 2022) of osteoblast-associated transcription factors (Zhu et al., 2024) in CAF subsets. **(E)** Flow cytometry contour plots of tumor fibroblasts on day 14 after 2.5e5 HY19636 s.c. cell injection in *Pdgfra*-Cas9-EGFP mice with single or combinatorial 1e10 vg AAV-gRNA injection on day −1. **(F)** Quantification of E. Data are mean ± SD, and significance was tested using one-way ANOVA with Tukey's multiple comparison test (n = 2–5 tumors/group, pooled from two independent experiments). *P < 0.05, **P < 0.01, ***P < 0.001, ****P < 0.0001.

Krishnamurty et al., 2022). While inhibition of either the JAK/STAT or the TGFBR signaling pathway via systemic drug application polarized CAFs to opposite cell states (Biffi et al., 2019), we noticed adoption of a separate osteoblast-like transcriptional cell state when TGFBR2 signaling was specifically inhibited in CAFs only, as opposed to pathway inhibition in any cell that a systemically administered drug could reach. Furthermore, KO of members of the TNF pathway (via *Tnfrsf1a* KO) or the canonical Wnt pathway (via *Ctnnb1* KO) in combination with TGFBR2 diminished CAF polarization toward both myofibroblast and osteoblast-like phenotypes, demonstrating how multiple gene edits via AAV-gRNA delivery can uncover hierarchies of pathway activities in CAFs (Fig. 6).

Lack of TGFBR2 signaling in FSP1^{+} fibroblasts with a resulting increase in secreted hepatocyte growth factor has been described as a transforming factor in epithelial cells, specifically contributing to squamous cell carcinoma of the forestomach, intraepithelial neoplasia in the prostate of mice, and developmental abnormalities in mammary duct development (Bhowmick et al., 2004; Cheng et al., 2005; Eikesdal et al., 2018). Other tissues appeared histologically normal, emphasizing the importance of how organ-specific and temporally controlled fibroblast perturbations (e.g., constitutively throughout development or acute perturbation in the adult animal) can have distinct effects on their local tissue environments. The local fibroblast-specific gene editing afforded us the possibility of temporally controlled perturbation, where *Tgfbr2* KO induced a unique CAF cell state that led to the recruitment of distinct neutrophil and TAM subsets. This observation was similar to recent findings of conditional fibroblast-specific KO of *Tgfbr2* in either alveolar fibroblasts in the setting of lung fibrosis or in brain border fibroblasts in stroke, where an increase in monocytes or neutrophils, respectively, was observed when fibroblast-specific TGFBR2 signaling was disrupted (Tsukui et al., 2024; Ewing-Crystal et al., 2025). Intriguingly, mice fared worse in both settings when *Tgfbr2* was knocked out in fibroblasts, mirroring the worse survival of PAAD in patients with a high *Tgfbr2* KO-associated, osteoblast-like gene signature (Fig. 4 G). While the higher morbidity in the lung fibrosis and stroke models could be attributed to a disrupted resolution of inflammation, further work is required to determine how a lack of *Tgfbr2* signaling in CAFs contributes to worse survival. In particular, the functional importance of the Col18a1 fibroblasts in the tumor setting remains to be established, likely across multiple settings. Application of this local gene editing platform in orthotopic cancer models and other models of fibrosis in future studies can shed light on their importance, especially by targeting the TNFR1 and/or Wnt signaling pathways, which are required for their formation. Targeting of Col18a1 fibroblast marker genes, such as Col18a1 itself, provides another intriguing strategy to assess the function of Col18a1 fibroblasts in TME formation.

Single-cell studies of tissue ecosystems have highlighted the relationship of immune, stroma, and parenchymal cells in settings of disease and homeostasis (Bonnardel et al., 2019; Combes et al., 2022; Luca et al., 2021; Pelka et al., 2021). Observing these processes over space and time allow generation of experimentally and computationally inferred cell state trajectories within individual cells, as defined by transcriptional changes occurring throughout the process (Hu et al., 2023; Qiu et al., 2022). These types of changes of transcriptional states by individual cells are linked through paracrine signaling with their neighboring cells and have been formulated in two-cell circuits between heterotypic cells, such as macrophages and fibroblasts (Zhou et al., 2018). By manipulating fibroblasts locally with high genetic precision, we were able to extend these findings to test how perturbations in fibroblasts alter the relationships between different cell types and which cell states are linked during multicellular tissue processes. Crucially, this goes beyond computationally inferred cell–cell interactions and affords rapid validation of which mediators orchestrate the observed multicellular changes, which are not necessarily observed on a compositional level of changed major cell type proportions but instead are hidden within linked transcriptional cell state changes. One previously underappreciated linkage discovered here is between TGFBR2 signaling inhibited CAFs recruiting Siglec-F^{hi} neutrophils via increased *Cxcl5* expression (Fig. 5). Siglec-F^{hi} neutrophils in the TME have been described as CD8 T cell inhibitory (Simoncello et al., 2022), inversely correlated with immunotherapy response (Gungabeesoon et al., 2023), and being recruited by cancer cell–derived *Cxcl5* (Zhou et al., 2014). Here, we extend that cell–cell relationship to include *Cxcl5*$^{+}$ CAFs, demonstrating how their altered state can negatively affect the cellular TME by recruiting these immune inhibitory neutrophils. This highlights how fibroblasts occupy an important niche within the cellular hierarchy in the TME (Mayer et al., 2023), and how their local perturbation allows discovery of linked constellations of cell states at site.

The method defined here thus provides a rapid and site-selective approach to modulate fibroblasts and record the resulting changes within them and the pathways that are modified via single or combinatorial KOs of target genes. We envisage that with this quicker turnaround time from gene target identification to combinatorial gene perturbations, we can learn more, discover faster, and describe better fibroblast functions in their native tissue context.

Limitations

The outlined approach requires the use of a transgenic mouse line expressing Cas9 driven by Cre expression in fibroblasts. While the choice of Cre driver can be further modified to control conditional Cas9 expression in a desired cell population to potentially investigate more defined fibroblast subpopulations or other cell types (Plikus et al., 2021), it does prevent this technology from being directly adopted for use in genetically engineered mouse models (GEMMs) of cancer that rely on Cre expression in the cancer-initiating cell. GEMMs of cancer generally recapitulate aspects of tumor initiation, progression, metastasis, and outgrowth more faithfully than transplanted tumor models, as used in this study. Fibroblasts have been described as being involved in all of these processes (Sahai et al., 2020), emphasizing the need to develop more sophisticated approaches. It is conceivable to combine the Cre-driven Cas9 expression in the fibroblast with alternative recombinase systems, such as the Flp/Frt or Dre/rox systems (Chen et al., 2021; Han et al., 2021; Schönhuber et al., 2014), or non-recombinase–dependent tumor models such as the MMTV-PyMT mammary carcinoma model (Guy et al., 1992), which would allow studying these gene perturbations in GEMMs of cancer.

We also note that when targeting one gene for KO in a cell population, compensatory expression of the targeted gene in the non-edited fraction of the cell population may limit our ability to draw conclusions about the absolute requirement for any one gene in any given cell (e.g., *Il1r1* in this study).

The dual KO approach of co-injecting two different AAVs delivering gRNAs targeting two different genes has the disadvantage of potentially generating nonuniform KO efficiencies between the two targeted genes, as seen in this study (Fig. S5, S–W). This can lead to a low percentage of double KO observed within the same cell if the two AAV transduction events are independent and if one transduction is significantly lower than the other, which was seen in some mice, but not all. Future studies targeting more than one gene should use multiplexed designs, wherein only one AAV is used carrying multiple gRNAs in its genome (McCarty et al., 2020). This should increase multiple gene KO efficiencies in the target cell by only requiring efficient transduction of one AAV (Fig. S1 H), circumventing the need for one cell being transduced by multiple different AAVs, and thereby increasing the robustness of this combinatorial local gene editing approach in fibroblasts.

This study investigated CAF cell states as collected from s.c. transplanted pancreatic cancer cells. The heterotopic growth of the tumor in the skin does not fully recapitulate the TME in pancreatic cancer. Thus, aspects of pancreas-specific fibroblasts, such as pancreatic stellate cells, which contribute unique aspects of CAF biology (Sherman and di Magliano, 2023), are not considered here. Orthotopic injection of AAVs into the organ of interest, such as the pancreas, is conceivable, albeit requiring invasive or ultrasound-guided surgical procedures (Camara Serrano, 2022). While we demonstrate feasibility of local CAF editing in transplantable orthotopic pancreatic tumor models using this system (Fig. 1, Q and R), future and extensive studies may apply this approach to isolating disease-specific functions and networks of fibroblast models, beyond those in the skin. We also note that fibroblasts and their gene networks may operate differently in different organs.

Materials and methods

Animals

Mouse strains and breeding

All mice were housed in an American Association for the Accreditation of Laboratory Animal Care–accredited animal facility and maintained in specific pathogen-free conditions. All animal experiments were approved and performed in accordance with the Institutional Animal Care and Use Program protocol number

AN200424. WT C57BL/6J (#000664), *Pdgfra*-Cre (#013148), and *Rosa26*-LSL-Cas9-EGFP (#026175) mice were purchased from The Jackson Laboratory. *Pdgfra*-CreERT2 (stock #032770) mice were a kind gift from Dr. Tien Peng (University of California, San Francisco [UCSF], San Francisco, CA, USA). *Cthrc1*-CreERT2;Ai14 mice were a kind gift from Drs. Tatsuya Tsukui and Dean Sheppard (UCSF, San Francisco, CA, USA). Transgenic *Pdgfra*-Cre mice were crossed with *Rosa26*-LSL-Cas9-EGFP$^{+/+}$ mice to generate F1 *Pdgfra*-Cre;*Rosa26*-LSL-Cas9-EGFP$^{+/wt}$ mice. F1 *Pdgfra*-Cre;*Rosa26*-LSL-Cas9-EGFP$^{+/wt}$ mice were crossed with *Rosa26*-LSL-Cas9-EGFP mice to generate F2 *Pdgfra*-Cre;*Rosa26*-LSL-Cas9-EGFP$^{+/+}$ mice, which were used for experiments. KI Pdgfra-CreERT2 mice were bred in the same manner to generate *Pdgfra*-CreERT2$^{+/wt}$;*Rosa26*-LSL-Cas9-EGFP$^{+/+ \text{ or } +/wt}$ mice and used in experiments after tamoxifen treatment (see below) only in Figs. S1 and 2. *Col1a2*-CreERT2 (MGI 6721050 from Bin Zhou [Shanghai Tech University, Shanghai, China]) (He et al., 2017) were crossed with *Tgfbr2*$^{Exon2-fl/fl}$ mice (MGI 2384513, kind gift from Dr. Ari Molofsky [UCSF, San Francisco, CA, USA]) (Chytil et al., 2002) to generate *Col1a2*-CreERT2$^{+/wt}$;*Tgfbr2*$^{Exon2-fl/fl}$ mice. All mice were housed at the UCSF animal facility with typical light/dark cycles and standard chow.

Tamoxifen treatment

For tamoxifen-induced Cre recombination in *Cthrc1*-CreERT2, *Pdgfra*-CreERT2, and *Col1a2*-CreERT2 mice, adult mice aged 6–12 wk were injected i.p with 100 µl of tamoxifen (#T5648; Sigma-Aldrich) dissolved in corn oil or ChremophorEL:EtOH:PBS (ratio 1:1:2) at 20 mg/ml, yielding a dose of 2 mg per mouse, on five consecutive days 1 wk prior to tumor engraftment.

Tumor models

For tumor growth studies and engraftment, YUMM5.2 mouse melanoma cancer cells derived from male *Tyr*-Cre;*Braf*$^{V600E/wt}$;*Trp53*$^{-/-}$ mice (Meeth et al., 2016) (5×10^5 cells/50 µl PBS) or HY19636 mouse pancreatic cancer cells derived from female KPC mice (*Kras*$^{LSL-G12D/+}$;*Trp53*$^{lox/+}$;*p48/Ptfla*-Cre) (Bardeesy et al., 2006) (2.5×10^5 cells/50 µl PBS) were transplanted into the s.c. mouse flank of male or female mice, respectively. For tumor growth studies, tumor size was monitored twice a week using the formula $0.5 \times (\text{length} \times \text{width}^2)$. Once reaching an endpoint of size >1,000 mm^3, mice were euthanized. For indicated analyses, mice were sacrificed at indicated time points, tumors were excised, and processed for downstream analysis.

For intrapancreatic orthotopic growth of HY19636 cells, mice were anesthetized with 3% isoflurane and s.c. injected with 50 µl of 0.25% bupivacaine and 50 µl of 50 µg/ml buprenorphine for analgesia. The hair was removed on the left side flank, and the skin was prepared by three alternating rounds of applying ChloraPrep swab stick (2% wt/vol chlorhexidine gluconate and 70% vol/vol isopropyl alcohol) and alcohol wipes. A small incision was made in proximity to the spleen, both in the skin and the peritoneum, and the pancreas was carefully exposed by gently pulling on the spleen with forceps. For injection, 2.5e5 HY19636 cells and 3e10 vg of AAV were co-injected in a total volume of 50 µl of PBS into the tail of the pancreas using a 31G insulin syringe. After injection, the peritoneal incision was closed using 4-0 PDS II sutures (#Z823G; Ethicon), and then the skin incision was closed using the BD AutoClip Wound Closing System. Mice were monitored for 48 h after surgery for any signs of distress and given second dose of buprenorphine 4–6 h after surgery, third dose the following morning, fourth dose in the afternoon, and additional doses as needed.

Bleomycin-induced skin fibrosis model

For induction of skin fibrosis, 6–20-wk-old male C57BL/6 mice *Pdgfra*-Cre;*Rosa26*-LSL-Cas9-EGFP$^{+/+}$ mice were injected s.c. with 100 µl of 1 U/ml bleomycin (#16714090801; NorthStar Rx) dissolved in PBS three times per week for 3 wk into a 1×1 cm^2 area on the dorsal skin of the animal, rotating injection site at every injection.

Cell lines

The YUMM5.2 mouse melanoma cell line (CRL-3367; ATCC), the HEK293T cell line (CRL-3216; ATCC), and the mouse fibroblast cell line NIH/3T3 (CRL-1658; ATCC) were purchased from ATCC. The HY19636 pancreatic tumor cell line was a kind gift from Dr. Hiaoqing Ying (MD Anderson Cancer Center, Houston, TX, USA). The Lenti-X 293T cell line was purchased from Takara (#632180). All cell lines were cultured at 37°C in 5% CO_2 in cell growth media: DMEM (11995065; Gibco) supplemented with 10% FBS (Foundation C, 900-308; Gemini Bio), 2 mM L-glutamine, 100 U/ml penicillin, 100 µg/ml streptomycin, and 50 µM β-mercaptoethanol (21985-023; Gibco). For all tumor injections, cells were used within the first two passages after thawing. The HY19636 cell line was kept below passage #10, and the YUMM5.2 cell line was kept below passage #20 for experiments.

To generate NIH/3T3 cells expressing Cas9 (NIH/3T3.Cas9.EGFP), NIH/3T3 cells were lentivirally transduced with the viral supernatant produced in Lenti-X 293T cells after transfection with the following plasmids: cargo plasmid containing Cas9 and EGFP (pL-CRISPR.EFS-GFP, #57818; Addgene), VSV-G envelope–containing plasmid (pMD2.G, #12259; Addgene), and envelope plasmid (pCMV-dR8.91, #OVT2971; Creative Biogene) at a molar ratio of 1:0.44:0.8, respectively, and added polyethylenimine (PEI), linear, MW 25000 (#23966; Polysciences) at a PEI-to-DNA ratio of 4-to-1. Two days after Lenti-X 293T transfection, viral supernatant was filtered through a 0.45-µm filter (Whatman) and added to NIH/3T3 cells with supplemented polybrene (#TR-1003-G; Sigma-Aldrich) at a final concentration of 8 µg/ml. Cas9-expressing NIH/3T3 cells were enriched by sorting EGFP$^+$ cells.

AAV production

The helper plasmid (pHelper, #6234; Takara) was used in conjunction with one of three different RepCap plasmids (7m8, #64839; Addgene [Isgrig et al., 2019]; pAAV-DJ [Grimm et al., 2008] Cell Biolabs, VPK-420-DJ; pAAV2/1, #112862; Addgene), and a scAAV cargo vector (see design below) to package vector genomes into double-stranded AAV particles. For AAV production, on day 1, three 15-cm dishes were seeded, each with 9e6 HEK293T cells (ATCC, CRL-3216) in 23 ml of cell growth media DMEM (11995065; Gibco) supplemented with 10% FBS (Foundation C, 900-308; Gemini Bio), 2 mM L-glutamine, 100 U/ml penicillin, 100 µg/ml streptomycin, and 50 µM β-mercaptoethanol

(21985-023; Gibco). On day 2, the HEK293T cells were transfected using PEI at a PEI-to-DNA ratio of 8-to-1 (660 µg total PEI), with the DNA comprising 20.25 µg cargo plasmid, 26 µg RepCap plasmid, and 36.36 µg pHelper, all in a total volume of 7.5 ml of a 150 mM NaCl solution. Each plate of HEK293T received 2.5 ml of the PEI-DNA transfection reagent by dropwise adding it on top. Transfected HEK293T cells were cultured for 3 more days, and then AAV was collected using the AAVpro Purification Kit Midi (6675; Takara) following the manufacturer's instructions. After purification, aliquots were taken to determine titers by qPCR after DNase I (#B0303S; NEB) treatment and proteinase K (#1114886; Qiagen) digestion. For qPCR, primers amplifying a 138-bp region of the hU6 promoter on the cargo plasmid within the ITRs were used (titer_U6_Forward, 5′-GAGGGCCTATTTCCCATGATTCC-3′; titer_U6_Reverse, 5′-CCCAAGAAATTATTACTTTCTACGTCACG-3′) with the SsoAdvanced Universal SYBR Green Supermix (#1725270; Bio-Rad) on CFX384 BioRad Real-Time PCR System with the following cycling protocol: 95°C for 30 s, 95°C for 5 s, 58°C for 20 s, and repeat steps 2 and 3 40 times. Relative quantity was determined by comparison with a serial dilution of the cargo plasmid standard of known concentration. AAVs were stored in autoclaved protein low-binding tubes (3207; Costar) and handled with protein low-binding pipets (4151; Corning).

AAV cargo plasmid design

To generate the pscAAV-hU6-gSCR-CBh-mCherry plasmid (#249124; Addgene) for generation of scAAVs carrying a gRNA cassette plus mCherry as a reporter gene for transduction efficiency, the pscAAV-CAG-EGFP plasmid (83279; Addgene) was cut using AvrII and NotI, and then Gibson assembled (Gibson et al., 2009) with a PCR-amplified fragment from pAAV-U6-gRNA-CBh-mCherry (forward primer, 5′-GTTCCTGGAGGGGTGGAGTCG TGACCTAGGGAGGGCCTATTTCCCATGATTCCTT-3′; reverse primer, 5′-AAAGCATCGAGATCGCAGGTGAGGCCTAGCGGC CGCTTACTTGTACAGCTCGTCCATGCC-3′). This yielded the intermediate plasmid pscAAV-hU6-gRNA-CBh-mCherry, which was never used for scAAV production because it had a 77 bp sequence between the RNA polymerase III termination sequence at the 3′ end of the gRNA scaffold sequence and the KpnI cut site at the 5′ end of the CBh promoter sequence. The pscAAV-hU6-gRNA-CBh-mCherry plasmid was then cut with AvrII and KpnI and Gibson assembled with a 402-bp long double-stranded DNA (dsDNA) oligo synthesized by Twist Biosciences containing the scrambled gSCR sequence (5′-GCTTAGTTACGCGTGGACGA-3′) (Suzuki et al., 2016), which does not exist in the murine genome; gRNA scaffold; and shortened sequence between the gRNA scaffold and CBh promoter, yielding the pscAAV-hU6-gSCR-CBh-mCherry plasmid with a 2053 bp insert from 5′ ITR to 3′ ITR sequence. This plasmid was then used to clone all other plasmids containing a single gRNA by cutting it with AvrII and KpnI and then inserting a dsDNA oligo (synthesized by Twist Biosciences) containing the U6 promoter sequence plus a gRNA sequence of interest. These plasmids were then used for scAAV packaging.

To generate the KIKO plasmid pscAAV-KIKO-U6-gThy1-p2a-mCherry-STOP-pA-400 (#249129; Addgene), the pscAAV-hU6-gSCR-CBh-mCherry plasmid was cut with AvrII and SpeI and Gibson assembled with two dsDNA oligos synthesized by Twist Bioscience containing the hU6-gThy1 sequence, gRNA scaffold, 400-bp left homology arm complementary to the sequence upstream of the gThy1 cut site, P2A element, mCherry ORF with stop codon, SV40late polyadenylation sequence, and a 380-bp right homology arm complementary to the sequence downstream of the gThy1 cut site. All other KIKO constructs were generated using the same cloning strategy with adjusted homology arms and gRNA sequences depending on KI site. All plasmid and gRNA sequences used in this study are found in Table S5 and have been deposited on Addgene (#249119-249131).

AAV transduction *in vitro*

For validation of AAV-mediated KO, NIH/3T3.Cas9 cells were used as target cells and analyzed by flow cytometry to assess KO efficiencies. On day 1, 1e4 NIH/3T3.Cas9 cells were seeded in 500 µl culture media per well in a 24-well cell culture plate. On day 2, 16 h later, AAV was added at specified multiplicity of infection. After 3–5 days of incubation, culture media was aspirated; cells were washed once with PBS and collected using trypsin (0.05% Trypsin-EDTA, #25300054; Gibco) to detach the cells. Cells were further processed for flow cytometry analysis of surface protein expression of target gene KO and mCherry reporter gene expression transduction efficiency. See below for details on flow cytometry analysis.

AAV application *in vivo*

All AAV injections in this study were done s.c. on the dorsal lateral flank of mice 24 h prior to tumor engraftment at the same site. The hair at the site of injection was removed using clippers and cleaned using alcohol wipe pads. The doses used were either 1e10-3e10 vg AAV per injection in 50 µl PBS using a 31-G insulin syringe (163311564B; Sol-M). The actual dose used for each experiment can be found in the figure legends. AAV injection sites were demarcated using green tattoo paste (2420101; Thermo Fisher Scientific), allowing engraftment of tumor cells at the same site the next day (see Fig. S1 F).

Indel frequency analysis

Indel frequencies within target cell populations at gRNA target sites were estimated using genomic DNA as input for amplicon PCR surrounding the gRNA target sites, followed by Sanger sequencing and ICE analysis (Synthego Performance Analysis, ICE Analysis. 2019. version 3.0. Synthego). Primers used for amplicon PCRs are listed in Table S6.

Tissue collection and processing for flow cytometry

Tumor and skin samples

At time of analysis, mice were euthanized, and tumor mass was carefully excised from the s.c. region without collecting the adjacent skin and surrounding adipose tissue. For skin collection, a 3 × 3 cm^2 region on the dorsal flank, cleared from hair using clippers, was excised using scissors, and excess fat was removed. On ice, samples were finely minced with scissors and then placed in a 2-ml tube containing 1.5 ml of digestion medium (2 mg/ml collagenase XI [C7657; Millipore Sigma], 0.5 mg/ml hyaluronidase [LS005477; Worthington], and 0.1 mg/ml DNase [10104159001; Roche] in DMEM [11995065; Gibco] supplemented

with 10% FBS [Foundation C, 900-308; Gemini Bio], 2 mM L-glutamine, 100 U/ml penicillin, 100 µg/ml streptomycin, and 50 µM β-mercaptoethanol [21985-023; Gibco]). The tube was placed horizontally in a bacterial shaker for 45 min at 37°C and 225 rpm. The tumor samples were then filtered through a 40-µm filter, and skin samples were filtered through a 100-µm filter. Samples were then washed with 10 ml cold PBS. The generated single-cell suspension was then processed further depending on analysis method.

Spleen and LNs

Inguinal and brachial LNs were collected, and the capsule was mechanically torn open using two 25-G needles prior to digestion. LNs and spleens were then separately digested in 1 ml digestion media (2 mg/ml collagenase D, collagenase IV [50 µg/ml] in DMEM with 2% FBS, and 10 mM HEPES [Sigma-Aldrich, H0887]) for 30 min at 37°C without agitation. Every 10 min, samples were pipetted up and down five times using a P1000 pipette. Samples were filtered through a 35-µm filter and washed with 3 ml of cold PBS. After pelleting the spleen sample at 500 *g* for 5 min in a centrifuge, the sample was resuspended in 1 ml of RBC lysis buffer (11814389001; Roche) and incubated for 10 min on ice to lyse red blood cells. The lysis was quenched by adding 4 ml of fluorescence-activated cell sorting (FACS) buffer (staining buffer [PBS, 2% FBS, and 2 mM EDTA]). Cells were pelleted again at 500 *g* for 5 min in a centrifuge and resuspended in FACS buffer and used for further analysis.

Pancreas tumor processing

To collect orthotopically grown tumors after intrapancreatic tumor cell injection, mice were euthanized, and tumor mass was carefully excised from the pancreatic tissue. Tumor tissue was minced with scissors on ice in 200 µl of digestion buffer (1× PBS, 4% bovine serum albumin [A4503; Sigma-Aldrich], 0.2 mg/ml trypsin inhibitor [T6522; Sigma-Aldrich], 0.2 mg/ml DNase I, 2 mg/ml collagenase XI, and 0.5 mg/ml hyaluronidase), then incubated for 30 min in 5 ml total digestion buffer on an orbital shaker at 37°C and 180 rpm in a 15-ml conical tube. Sample was pulse vortexed once every 10 min. Digestion was stopped by adding 5 ml of Stop buffer (1× PBS, 5% FBS [Foundation C, 900-308; Gemini Bio], and 0.2 mg DNase I). Single-cell suspension was filtered through 70-µm nylon filter, washed with 5 ml of 1× PBS, and pelleted at 350 *g* for 5 min at 4°C. Red blood cells were lysed with RBC lysis buffer (11814389001; Roche) for 10 min on ice. Cells were washed and pelleted again at 350 *g* for 5 min at 4°C and then used for subsequent processing and analysis.

Flow cytometry

AAV validation in vitro

NIH/3T3.Cas9 cells transduced with AAVs *in vitro* were collected, washed, and pelleted at 500 *g* for 5 min centrifugation in FACS staining buffer (PBS, 2% FBS, and 2 mM EDTA) and resuspended in 50 µl of staining buffer plus 0.5 µg purified anti-mouse CD16/32 antibody (clone 2.4G2, Tonbo Biosciences). Samples were incubated for 10 min on ice to block FC receptors. Following this incubation, the cells were stained with antibodies against surface receptors that were targeted by AAV. Antibodies were diluted in 50 µl staining buffer prior to addition of cells to yield a final volume of 100 µl staining volume. Antibodies used for staining and their dilutions are listed in Table S6. The cells were incubated for a further 10 min on ice in the dark. After this staining incubation, cells were washed with 1 ml of staining buffer, pelleted again at 500 *g* for 5 min, and resuspended in staining buffer containing DAPI (1 µg/ml) as a live/dead stain. Cells were analyzed on a BD LSRFortessa Cell Analyzer (BD Biosciences) at the Parnassus Flow Cytometry core at UCSF and gated on live (DAPI-negative) singlets. Loss of surface receptor expression compared with naive (not exposed to AAV) NIH/3T3.Cas9 cells was used as a readout of KO efficiency, and expression of mCherry was used as a readout for transient AAV expression in the KO constructs.

Staining of tumor and tissue samples

Single-cell suspensions from tumors and other tissues were generated as described above, pelleted by centrifugation at 500 *g* for 5 min, resuspended in 5e6 cells/50 µl FACS staining buffer containing 1 µg purified anti-mouse CD16/32 antibody (clone 2.4G2; Tonbo Biosciences). Samples were incubated for 10 min on ice to block FC receptors. Following this incubation, 50 µl FACS staining buffer containing antibodies for surface staining was added and incubated for 20 min at room temperature in the dark. Antibodies used for staining and their dilutions are listed in Table S6. Cells were washed with 1 ml of FACS staining buffer, pelleted, and resuspended in FACS staining buffer containing DAPI (1 µg/ml) for live cell discrimination prior to analysis on a BD LSRFortessa Cell Analyzer (BD Biosciences).

FACS of fibroblast subsets

For sorting of tumor fibroblast subsets, tumors were processed as described above to generate a single-cell suspension and stained as described in the previous section. After staining, cells were filtered on a 35-µm filter right before being sorted on a BD FACSAria II cell sorter (BD Biosciences) Parnassus Flow Cytometry core at UCSF. Cells were collected based on the gating scheme outlined in Fig. S1 B to yield live singlet fibroblasts as defined by DAPI$^-$ CD31$^-$ CD45$^-$ E-Cadherin$^-$ MCAM$^-$ Thy1$^+$ PDPN$^+$ EGFP$^+$, and then further subsetted as outlined in Fig. S2 K to sort four fibroblast subsets: DP SCA-I$^+$ Ly6C$^+$, Int SCA-I^{mid} Ly6C^{mid}, DN SCA-I$^-$ Ly6C$^-$ NCAM1$^-$, and DN SCA-I$^-$ Ly6C$^-$ NCAM1$^+$. Sorted cells were collected in 4°C cold cell culture media (DMEM with 10% FCS, 2 mM L-glutamine, 100 U/ml penicillin, 100 µg/ml streptomycin, and 50 µM β-mercaptoethanol). For each sample, 2,000–24,000 cells were collected per fibroblast subset. Individual samples were immediately pelleted by centrifugation at 500 *g* for 5 min at 4°C and processed for qPCR analysis as described below.

Ex vivo stimulation and immunofluorescence imaging of CAFs

For *ex vivo* culturing, stimulation, and subsequent immunofluorescence imaging (Fig. 2 F), CAFs from day 14 HY19636 tumors that had received 3e10 vg AAV-KIKO-Thy1 (control), AAV-KIKO-Osmr, or AAV-KIKO-Tgfbr2 to generate local KIKOs on day 1 were isolated and processed for sorting as described above using the following markers: samples were stained with anti-mouse

CD31-PerCP-Cy5.5 (clone 390; BioLegend) and anti-mouse CD45-BUV395 (clone 30-F11; BD Biosciences) and sorted as singlets DAPI⁻ CD31⁻ CD45⁻ EGFP⁺ cells on a BD FACSAria II cell sorter (BD Biosciences) Parnassus Flow Cytometry core at UCSF. 2,000–3,000 EGFP⁺ CAFs were collected from each tumor in 500 µl of DMEM (11995065; Gibco) supplemented with 10% FBS (Foundation C, 900-308; Gemini Bio), 2 mM L-glutamine, 100 U/ml penicillin, 100 µg/ml streptomycin, and 50 µM β-mercaptoethanol (21985-023; Gibco) and then directly transferred into one well of a 8-well Lab-Tek ChamberSlide with removable gasket (177445; Lab-Tek). CAFs were allowed to adhere to slide for 14 h during incubation at 37°C in 5% CO_2. CAFs from AAV-KIKO-Thy1 (control) and AAV-KIKO-Osmr–treated tumors were stimulated with recombinant mouse OSM (762802; BioLegend) at a concentration of 50 ng/ml for 20 min at 37°C in 5% CO_2. CAFs from AAV-KIKO-Thy1 (control) and AAV-KIKO-Tgfbr2–treated tumors were stimulated with recombinant mouse TGF-β1 (763102; BioLegend) at a concentration of 1 ng/ml for 20 min at 37°C in 5% CO_2. After removing media and washing in 1× PBS, cells were then fixed in 4% formaldehyde (18814; Polysciences, Inc.) for 15 min at room temperature. Fixative was aspirated, and fixed cells were rinsed three times in 1× PBS for 2 min each. Cells were then permeabilized with ice-cold 100% methanol (179337; Millipore Sigma) for 10 min at room temperature. Methanol was aspirated, and cells were rinsed three times in 1× PBS for 2 min each. Cells were then blocked in blocking buffer (1× PBS, 5% mouse serum, and 0.3% Triton X-100) for 60 min at room temperature and then stained with anti-human/mouse phospho-STAT3-AF647 (clone 4/P-STAT3, BD Biosciences, 1:100) or anti-human/mouse phospho-SMAD2/3-AF647 (clone 072-670, BD Biosciences, 1:100) plus DAPI (1 µg/ml) in antibody staining buffer (1× PBS, 1% bovine serum albumin [A4503; Sigma-Aldrich], and 0.3% Triton X-100 [T8787; Millipore Sigma]) for 16 h at 4°C in the dark. Cells were then washed three times in 1× PBS, the gasket was removed from the Lab-Tek slide, and cells were mounted using VECTASHIELD PLUS (H-1900; Vector Laboratories, Inc.). For imaging, samples were acquired on a Leica Stellaris 5 (Leica) inverted laser scanning confocal microscope with a water immersion 25 × HC Fluotar VISIR (506375; Leica) objective using the 405, 488, and 638 nm laser lines to excite DAPI, EGFP, and AF647, respectively. A 4 × 4 tiled image was acquired, and images were analyzed using the Imaris software suite (Bitplane). For quantification, CAFs were identified based on EGFP signal, and all DAPI⁺ nuclei were counted, and a percentage of DP DAPI⁺ AF647⁺ nuclei of all DAPI⁺ nuclei was calculated per sample.

Tissue collection and processing for microscopy

Tissue collection

S.c. tumors were excised from flank skin, including adjacent skin layers and then fixed in 4% paraformaldehyde (PFA) (16% PFA, Electron Microscopy Sciences, diluted in 1× PBS) at 4°C overnight on a rotator. This was followed by a 15% and 30% wt/vol sucrose in PBS incubation step at 4°C for 8 and 16 h, respectively. Samples were then embedded and frozen in OCT (4583; Sakura). 10- or 200-µm thick sections were then made using a cryostat and placed into PBS to wash OCT residue away. 200 µm samples were mounted using VECTASHIELD PLUS (H-1900; Vector Laboratories, Inc.) and then used for second-harmonic generation (SHG) imaging if no additional staining was required. For additional staining of PDPN on 10-µm sections, sections were preprocessed by washing once for 5 min in deionized H_2O at room temperature, refixed with 4% PFA for 10 min at room temperature, and then washed again for 5 min in deionized H_2O at room temperature. Sections were incubated with blocking buffer (1× PBS, 5% hamster serum, and 0.3% Triton X-100) for 1 h at room temperature in the dark and stained with anti-mouse PDPN-APC (clone 8.1.1., 127409; BioLegend; 1:100) plus DAPI (1 µg/ml) for 16 h at 4°C. Samples were then washed three times in deionized H_2O prior to being mounted using VECTASHIELD PLUS.

Immunofluorescence imaging of 10 µm sections

For 10-µm sections, samples were imaged using a Leica SP8 laser scanning confocal microscope with a white light laser (for detection of EGFP, mCherry, and PDPN-APC) and 405 nm diode (for detection of DAPI), using a 20× 0.75NA (HC PL APO 20×/0.75 IMM CORR CS2, Leica) objective. After acquisition, individual tiled images were stitched together using the LAS X software (Leica) and then analyzed using the Imaris software suite (Bitplane).

SHG and immunofluorescence imaging using 2-photon microscopy of 200-µm sections

For 200-µm sections, a custom-built 2-photon setup equipped with two infrared lasers (8W Mai Tai Ti:Sapphire, Spectra Physics; 18W Chameleon Vision II, Coherent) was used. The Mai Tai laser was tuned to 920 nm for excitation of EGFP. The Chameleon laser was tuned to 780 nm for simultaneous excitation of mCherry and detection of SHG. The two lasers were exciting in alternating sequences. Emitted light was detected using a 25 × 1.05-NA water lens (Olympus, XLPlan N) coupled to a six-color detector array (custom; utilizing Hamamatsu H9433MOD detectors). Emission filters used were: violet 417/50, green 510/42, red 607/70 to detect SHG, EGFP, and mCherry emission, respectively. The microscope was controlled using the Micro-Manager software suite (Pinkard et al., 2016) to acquire 16 z-stacks at z-depth of 10 µm to cover 150 µm total z-distance of the 200-µm thick sample. Multiple adjacent z-stacks were acquired to cover a larger XYZ tissue section. The individual z-stacks were stitched together using the Imaris-Micro Magellan compiler plugin from the Micro-Manager software suite. Data analysis was performed using the Imaris software suite (Bitplane).

Reverse transcription real-time quantitative PCR of sorted fibroblast subsets

Fibroblasts from tumors were isolated and sorted as described using the gating strategy outlined in Fig. S1 B and Fig. S2 K. Cells were washed and pelleted in 1× cold PBS, and RNA was isolated using the Qiagen RNeasy Micro Kit (#74004) according to the manufacturer's instructions. All isolated RNA was used as input for cDNA generation using the iScript Reverse Transcription Supermix (#1708840; Bio-Rad) following the manufacturer's instructions. The reaction mix was used for qPCR analysis using the SsoAdvanced Universal SYBR Green Supermix (#1725270;

Bio-Rad) on a Bio-Rad thermocycler with the following cycling conditions: 95°C for 30 s, 95°C for 5 s, 60°C for 10 s, repeat of steps 2 and 3 39 times, and then melt-curve analysis 65–95°C with 0.5°C increments at 5 s each. Each sample was run in technical triplicates for each assayed gene. 18 s expression was used for the reference gene normalization. Primer sequences used can be found in the Table S6.

scRNA-seq reference data sets

The previously published data sets by Hu et al. (2023) (mouse wound fibroblasts) and Krishnamurty et al. (2022) (mouse pancreatic tumor fibroblasts) were used as reference data sets for scRNA-seq analysis. Deposited data was downloaded from Gene Expression Omnibus (GEO) (Hu et al., 2023; GSE204777) or ArrayExpress (Krishnamurty et al., 2022; E-MTAB-12028). To generate the wound fibroblast Seurat object from Hu et al. (2023) the data was processed as described (Hu et al., 2023). To generate the tumor fibroblast Seurat object, the ReadMtx function from the Seurat R package (version 5.0.1) (Hao et al., 2024) was used to read in matrix.mtx, genes.tsv, and barcodes.tsv files. The CreateSeuratObject function was then used to generate the tumor fibroblast Seurat object. Cells were annotated using the meta.txt file, and fibroblasts were extracted based on rows matching "fibroblast" in the "CellType" column using the subset function. Cells were removed according to the feature count (<300) and mitochondrial count (>5%) parameters outlined in the original paper. The remaining fibroblasts were then further processed using the following Seurat functions in the listed order: NormalizeData (log-normalize RNA transcript counts), FindVariableFeatures (selection.method "vst," nfeatures = 2000), ScaleData (default parameters), RunPCA (default parameters), FindNeighbors (15 PCs), and RunUMAP (13 PCs) were used for 2D visualization. Clustering was performed using the FindClusters function (resolution of 0.3), and cluster 5 was removed as it was identified as a contaminating immune cell cluster (~1% of total object, 66 of 6,589 cells). The remaining tumor fibroblasts and wound fibroblasts were used to plot gene expression of homeostatic and activation marker genes using the DotPlot, FeaturePlot, and VlnPlot functions in the Seurat package.

Tumor collection and processing for scRNA-seq

For tumor collection and subsequent analysis by live cells from day 14 HY19636 tumors (after s.c. injection of 2.5e5 HY19636 on day 0 into *Pdgfra*-Cas9-EGFP mice) that had received 3e10 vg scAAV1-gTrac, scAAV1-gOsmr, scAAV1-gTgfbr2, or scAAV1-gIl1r1 to generate local KOs on day 1 were isolated and processed for sorting as described above on a BD FACSAria II cell sorter (BD Biosciences, Parnassus Flow Cytometry Core at UCSF) with minor modifications: live cells were identified as negative for Zombie-NIR (BioLegend, 1:200) and positive for Calcein blue AM (C1429; Thermo Fisher Scientific, 10 µM working concentration). Samples were additionally stained with anti-mouse CD45-BUV395 (clone 30-F11; BD Biosciences, 1:500), anti-Thy1.2/CD90.2-BV786 (clone 53–2.1; BD Biosciences, 1:500, for Thy1 detection), and anti-E-Cadherin/CD324-PE-Cy7 (clone DECMA-1; BioLegend, 1:200). Four live cell populations were sorted: (1) $CD45^+$ (immune cells), (2) $CD45^-$ $EGFP^+$ $Thy1^+$ (fibroblasts), (3) $CD45^-$ $EGFP^-$ E-Cadherin$^-$ (miscellaneous), and (4) $CD45^-$ $EGFP^-$ E-Cadherin$^+$ (tumor cells) (see Fig. S4 A for gating scheme). The four populations from each sample were then pooled in a 15-ml Falcon tube and pelleted for 7 min at 500 *g*. The supernatant was removed, and cells were further processed using the Chromium Fixed RNA Profiling (Gene Expression Flex) pipeline. In brief, each sample was first fixed using the Single Cell Fixed RNA Sample Preparation Kit (PN-1000414; 10x Genomics) following the manufacturer's instructions. Samples were fixed for 18 h at 4°C and, after addition of quenching buffer and storage buffer, stored at −80°C until further processing. After thawing of samples, samples were processed using the Chromium Fixed RNA Kit, Mouse Transcriptome (PN-1000496; 10x Genomics), following the manufacturer's instructions to generate a fixed RNA gene expression library. For multiplexing, each sample (4 replicates × 4 AAV groups = 16 total) was hybridized with a separate Probe Barcode library including added custom probes (*Egfp*, 8casd09, 5′-GGTAGTGGTCGGCGAGCTGCA CGCTGCCGTCCTCGATGTTGTGGCGGATC-3′; and *Egfp*, 8casd10, 5′-AGGGTGTCGCCCTCGAACTTCACCTCGGCGCGGGTCTTGTAG TTGCCGTC-3′). Approximately 2.5e5 total cells were encapsulated and sequenced on two lanes of a NovaSeq X flow cell (1.25 B reads/lane) to reach about 10,000 reads/cell. Sequencing output was processed using cellranger-7.2.0 and the mouse transcriptome probe set v1.0.1_mm10-2020-A with added custom *Egfp* probes from above. After demultiplexing the 16 samples using the provided Probe Barcodes, the samples were integrated in Seurat version 5.1.0 (Hao et al., 2024), and low-quality cells were filtered out if they had <150 genes or >20% mitochondrial genes. Features with counts in <3 cells were also filtered out. After merging all samples using the Seurat merge() function, the gene expression matrix was normalized using Seurat NormalizeData() function, with default parameters. The top 2,000 variable genes were identified, and the gene expression matrix was scaled prior to principal component analysis (PCA). The first 23 PCs were used for UMAP visualization based on the elbow plot cutoff, and the FindClusters() function at a resolution of 0.2 was used to identify individual clusters. The following markers were used to identify major cell types: fibroblasts (*Pdgfra*, *Col1a2*, and *Egfp*), pericytes (*Rgs5*), epidermal basal cells (*Krt14; Krt5*), endothelial cells (*Pecam1*), tumor cells (*Cdh1*; *Msln*), T cells and NK cells (*Trac*; *Ncr1*), neutrophils (*S100a8*), mast cells (*Mcpt4*), and myeloid cells (*H2-Ab1*; *Lyz2*). Major cell types were subsetted and further processed to remove doublets. DCs were further subsetted from the "myeloid cells" object. This generated nine separate objects: fibroblasts (n = 9,514), pericytes (n = 745), endothelial cells (n = 3,895), tumor cells (n = 81,588), T and NK cells (n = 5,209), neutrophils (n = 43,824), mast cells (n = 1,581), MonoMacs (n = 35,810), and DCs (n = 5,059). Tumor cells were subsampled to a total of 10,000 cells, and then all objects were remerged for Fig. S4 B. The individual fibroblasts, MonoMac, DCs, neutrophils, and T/NK cell objects were further sub-clustered, and the DEGs of the individual subclusters can be found in Table S1.

Pseudobulk differential gene expression analysis

For identification of DEGs between CAFs of different AAV-gRNA groups, we used a pairwise pseudobulk approach comparing the

control group (AAV-gTrac) with the three different experimental groups (AAV-gOsmr, AAV-gTgfbr2, or AAV-gIl1r1) individually. Each group was represented by four replicates, and DEGs were identified using MAST with random effects (Finak et al., 2015; Zimmerman et al., 2021). The number of DEGs are grouped by cell type with a threshold of P value <0.05 after false discovery rate correction using the Benjamini–Hochberg procedure. The list of DEGs for each experimental group can be found in Table S2.

Pseudotime analysis

Pseudotime analysis of the fibroblast scRNA-seq object

Prior to pseudotime analysis of the fibroblast object, the "myCAF proliferating" cluster was removed. After rerunning PCA, a UMAP representation was generated using the first 18 PCs (Fig. 4 A) in Seurat. The Seurat object was converted to a cell_data_set object using Monocle 3 (Trapnell et al., 2014) (version 1.3.7). The pseudotime trajectory was calculated using Monocle 3 with the homeostatic fibroblast cluster used as the root cell state. To plot the distribution of cells in pseudotime as a violin plot in Seurat, the position of each cell within the pseudotime graph was extracted from the cell_data_set object and then added as metadata to the Seurat object.

Pseudotime trajectory analysis of AAV-gTgfbr2 CAF object

The Seurat object containing AAV-gTgfbr2 CAFs only was analyzed independently to identify potential branchpoints in fibroblast polarization trajectory when *Tgfbr2* is knocked out. The monocle developmental trajectory was constructed using Monocle 2 (Qiu et al., 2017) (monocle R package, version 2.34.0). Raw count matrices were extracted and used to generate the CellDataSet object. Size factors and dispersions were estimated using estimateSizeFactors() and estimateDispersions() functions. Ordering genes were identified based on differential expression across cell identity clusters using differentialGeneTest(), and the top 1,000 genes ranked by q value were selected as ordering genes. Pseudotime was computed using reduceDimension() (method = "DDRTree") and orderCells() functions. Trajectories were visualized using plot_cell_trajectory(). Branch-dependent gene expression changes were analyzed using Branch Expression Analysis Modeling at branch_point = 1, and the top 50 branch-specific genes were visualized using plot_genes_branched_heatmap() with num_clusters = 2 to highlight distinct gene modules associated with divergent trajectories.

Comparison of gene expression similarity between CAFs and existing data sets

To measure the similarity of DEGs between CAF clusters in this study to published data sets, we performed the hypergeometric test to find overlapping genes using the phyper() function from the stats package in R. When comparing to published human data sets, the human genes from those data sets were label transferred to mouse genes using the homologene (version 1.4.68.19.3.27) (Mancarci, 2018) R package. DEGs from each individual data set were filtered based on a P value <0.05 and an average log2 fold change >0.25.

NMF decomposition

NMF was performed on the normalized gene-by-cell count matrix of the fibroblast object using the nmf function from the RcppML (version 0.3.7) R package (DeBruine et al., 2021, *Preprint*). All genes expressed in >2% of all cells were used as input. Mitochondrial (starting with "mt-") and ribosomal (starting with "Rps" or "Rpl") genes were excluded. To select the number of factors used for factorization (Fig. S5 H, top), first, the mean squared error (MSE) of an NMF model was plotted versus its factorization rank for NMF models of rank 1–50. Second, an inflection point was identified by plotting the difference between successive MSE values and then selecting the rank where the MSE values plateau (Fig. S5 H, bottom). K = 18 was the rank where the MSE values plateaued and was thus chosen as the K value in the nmf() function of the RcppML package using 1,000 maximum iterations (maxit = 1,000) and tol = 1e-5 as the stopping criteria. The factor-weight-by-cell matrix (h matrix output) was added to the fibroblast Seurat object as a new "NMF" assay using the Seurat CreateAssayObject function. The factor weight values from the NMF assay were used to visualize NMF factor weights per cell in UMAP representation (Fig. 4 D). The AverageExpression function in Seurat was used to calculate the average NMF factor weights per sample.

NMF factor weight correlation across CAFs

The NMF factor weights of each cell were correlated in pairwise fashion using the cor() function and "method = pearson" from the stats package. Statistical significance was measured using cor.mtest() function from the corrplot (version 0.95) R package (Wei and Simko, 2010).

GSEA

GSEA for fibroblast NMF factors was done using the hypeR (version 2.0.0) package (Federico and Monti, 2020) using R (version 4.3.2). The top 50 genes of each NMF factor were inputted for GSEA, and statistically significant enrichment among the gene ontology term "Biological Process" from the Molecular Signatures Database (MSigDB version 7.2.1) was computed using the hypergeometric test.

Survival analysis of TCGA data based on gene signatures

Data download and processing

The TCGA transcriptomic TPM data were downloaded from the Toil recompute (Vivian et al., 2017) in the TCGA Pan-Cancer cohort on the University of California, Santa Cruz, Xena browser (http://xena.ucsc.edu) and imported into R. The tumor samples were filtered down to only include primary solid tumors (sample type code = 01), and tumor types with <100 samples were excluded from further analysis. Prior to calculation of gene signature scores derived from mouse genes (i.e., the top 25 upregulated genes from AAV-gTgfbr2 DEG, AAV-gOsmr DEG, and AAV-gIl1r1 DEG analysis), the mouse gene names were transferred to their human orthologs using the gprofiler2 (version 0.2.3) R package (Kolberg et al., 2019). Mouse genes without human orthologs or human orthologs not present in the gene-by-sample matrix of TCGA data set were dropped from further analysis. Then, to select genes that are predominantly specific to fibroblasts in the TME, we only included genes if they were most highly expressed in fibroblasts or stellate cells (resident fibroblasts of the pancreas) within at least one of The Curated Cancer

Cell Atlas (Tyler et al., 2025) pancreatic cancer objects (Hwang et al., 2022; Lin et al., 2020; Moncada et al., 2020; Peng et al., 2019; Raghavan et al., 2021; Steele et al., 2020). Finally, to maintain gene signature specificity, genes that were shared between the three "AAV-gTgfbr2 up DEG"/"AAV-gOsmr up DEG"/"AAV-gIl1r1 up DEG" signatures were excluded. For the "stromal signature," the identified genes by Combes et al. (2022) were used. For the "fibroblast TGFβ response signature," the genes by Mariathasan et al. (2018) were used. For the "progenitor signature," the top5 nonoverlapping marker genes of the progenitor/homeostatic fibroblast clusters c03-COL15A1 and c05-PI16 by Gao et al. (2024) were used. The individual genes for each signature are listed in Table S4.

Gene signature score calculation

Gene signature scores were calculated on log10(TPM+1) normalized data, and the expression of each gene was converted to percentile ranks across the samples. The final gene signature score of each sample was calculated as the average percentile rank from all genes belonging to one gene signature.

Survival analysis

For pan-TCGA survival analysis, the Cox proportional hazards model from the survival (version 3.8-3) R package was used to test overall survival differences between patients in the top and bottom quartiles based on gene signature scores "stromal" and "fibroblast TGFbeta response," with age, sex, and cancer type as covariates. For survival analysis in the TCGA PAAD cohort, the same analysis was done on gene signatures after normalizing them to the "progenitor signature" because a high stromal signature is already associated with worse survival (Fig. S5 K). Kaplan–Meier survival curves were plotted using the survminer (version 0.5.0) R package. Forest plots of all analyzed cancer types were generated after meta-analysis using a random effects model using the meta (version 8.1-0) R package.

Identification of cell frequency correlation between fibroblasts and immune cells

To identify potential co-occurring cell populations of CAF subsets and captured immune cells in the scRNA-seq data set, the proportion of each cell subset within its corresponding major cell compartment (fibroblasts, MonoMacs, DCs, neutrophils, T, and NK cells) was calculated. The proportion of each cell subset was correlated in pairwise fashion with all other cell subsets across all 16 samples (4 replicates × 4 AAV groups) using the cor() function and "method = pearson" from the stats package. Statistical significance of correlation was measured using cor.mtest() function from the corrplot package (Wei and Simko, 2010), and results were plotted as a heatmap with samples arranged by hierarchical clustering.

Candidate identification of ligand–receptor interactions

The CellChat (Jin et al., 2021) (version 2.1.2) package was used to identify putative ligand–receptor interactions between two target cell populations. First, all cell subsets belonging to one experimental AAV group were subsetted from the full Seurat object. Then a CellChat object was created and processed using default parameters. Source and target cells were defined prior to plotting the top six inferred ligand–receptor interactions.

Transcription factor activity prediction with decoupleR

To infer osteoblast-related transcription factor activity in the CAF subsets, the decoupleR (version 2.10.0) package was used to run a univariate linear model (function "ulm") with default parameters. All genes were used as input, and all mouse transcription factors were initially considered. For plotting osteoblast-related transcription factor activity (Zhu et al., 2024), the mean activity of each transcription factor per CAF subset was used.

Quantification and statistical analysis

Statistical analyses were done using R version 4.3.2. Details of individual experiments can be found in their respective figure legends.

Online supplemental material

Table S1 shows DEGs for each cell subtype identified within major cell types. Major cell types grouped by sheet. Table S2 shows DEGs of AAV-gRNA groups using pairwise pseudobulk differential gene expression analysis comparing control (AAV-gTrac) with experimental groups (AAV-gOsmr, AAV-gTgfbr2, or AAV-gIl1r1). Table S3 shows weighted gene output ordered by NMF factors from fibroblast object. Table S4 shows signature genes used for survival analysis. Table S5 shows DNA sequences of plasmids and gRNAs used in this study. Table S6 shows table of reagents used in this study.

Data availability

The raw scRNA-seq data are available under GEO accession number GSE315708. The processed scRNA-seq data generated for this study and presented in Fig. 3, 4, 5, 6 and Fig. S4 and S5 have been deposited in the Synapse.org data repository under Project SynID syn71058181. Companion code is deposited on Github (https://github.com/NickKuhn/Kuhn_AAV-gRNA_CAF). The generated plasmids have been deposited at Addgene (#249119-249131). All other data supporting the findings of this study are available from the corresponding author on reasonable request.

Acknowledgments

We would like to thank members of the Krummel and Ari Molofsky labs for scientific discussions and comments on the manuscript. We would like to thank Bushra Samad in the DataScience CoLab at UCSF for guidance on computational analysis.

This work was supported by funds from National Institutes of Health (NIH) R01CA197363 and the Parker Institute for Cancer Immunotherapy (C-02350, C-04189). N.F. Kuhn is the recipient of a Cancer Research Institute/Merck Postdoctoral Fellowship (CRI4546). Flow cytometry was performed at the University of California San Francisco (UCSF) Parnassus Flow CoLab (RRID: SCR_018206) and supported in part by the UCSF Diabetes Research Center (DRC) Grant NIH P30 DK063720. Sequencing was performed at the UCSF Center for Advanced Technology,

supported by UCSF Program for Breakthrough Biomedical Research, Research Resource Program Institutional Matching Instrumentation Award, and NIH 1S10OD028511-01 grants.

Author contributions: Nicholas F. Kuhn: conceptualization, data curation, formal analysis, funding acquisition, investigation, methodology, project administration, resources, software, supervision, validation, visualization, and writing—original draft, review, and editing. Itzia Zaleta-Linares: investigation. Kenneth H. Hu: conceptualization, data curation, formal analysis, supervision, visualization, and writing—review and editing. Tristan Courau: methodology. Brittany Davidson: investigation and resources. Tammie Tam: data curation, resources, and software. Chih-Wei Chu: data curation, formal analysis, software, and visualization. Maxime J. Kinet: investigation and methodology. Michael D. Rosenblum: methodology and writing—review and editing. Alexis J. Combes: methodology, project administration, resources, supervision, and writing—review and editing. William A. Nyberg: methodology. Justin Eyquem: resources and supervision. Matthew F. Krummel: conceptualization, funding acquisition, methodology, project administration, supervision, validation, visualization, and writing—original draft, review, and editing.

Disclosures: M.D. Rosenblum reported personal fees from TRex Bio, Radera Bio, and Mozart Therapeutics outside the submitted work. A.J. Combes reported grants from Eli Lilly and Roche Genentech outside the submitted work. J. Eyquem reported personal fees from Azalea Therapeutics, Mnemo Therapeutics, Danaher, TreeFrog Therapeutics, and Resolution Therapeutics outside the submitted work. No other disclosures were reported.

Submitted: 17 June 2025
Revised: 9 July 2025
Accepted: 3 February 2026

References

Akhmetshina, A., K. Palumbo, C. Dees, C. Bergmann, P. Venalis, P. Zerr, A. Horn, T. Kireva, C. Beyer, J. Zwerina, et al. 2012. Activation of canonical Wnt signalling is required for TGF-β-mediated fibrosis. *Nat. Commun.* 3: 735. https://doi.org/10.1038/ncomms1734

Araujo, A.M., A. Abaurrea, P. Azcoaga, J.I. López-Velazco, S. Manzano, J. Rodriguez, R. Rezola, L. Egia-Mendikute, F. Valdés-Mora, J.M. Flores, et al. 2022. Stromal oncostatin M cytokine promotes breast cancer progression by reprogramming the tumor microenvironment. *J. Clin. Invest.* 132:e148667. https://doi.org/10.1172/JCI148667

Badia-I-Mompel, P., J. Vélez Santiago, J. Braunger, C. Geiss, D. Dimitrov, S. Müller-Dott, P. Taus, A. Dugourd, C.H. Holland, R.O. Ramirez Flores, and J. Saez-Rodriguez. 2022. decoupleR: ensemble of computational methods to infer biological activities from omics data. *Bioinform. Adv.* 2: vbac016. https://doi.org/10.1093/bioadv/vbac016

Bardeesy, N., K.-H Cheng, J.H. Berger, G.C. Chu, J. Pahler, P. Olson, A.F. Hezel, J. Horner, G.Y. Lauwers, D. Hanahan, and R.A. DePinho. 2006. Smad4 is dispensable for normal pancreas development yet critical in progression and tumor biology of pancreas cancer. *Genes Dev.* 20:3130–3146. https://doi.org/10.1101/gad.1478706

Baryawno, N., D. Przybylski, M.S. Kowalczyk, Y. Kfoury, N. Severe, K. Gustafsson, K.D. Kokkaliaris, F. Mercier, M. Tabaka, M. Hofree, et al. 2019. A cellular taxonomy of the bone marrow stroma in homeostasis and Leukemia. *Cell.* 177:1915–1932.e16. https://doi.org/10.1016/j.cell.2019.04.040

Batlle, E., and J. Massagué. 2019. Transforming growth factor-β signaling in immunity and cancer. *Immunity.* 50:924–940. https://doi.org/10.1016/j.immuni.2019.03.024

Bhowmick, N.A., A. Chytil, D. Plieth, A.E. Gorska, N. Dumont, S. Shappell, M.K. Washington, E.G. Neilson, and H.L. Moses. 2004. TGF-beta signaling in fibroblasts modulates the oncogenic potential of adjacent epithelia. *Science.* 303:848–851. https://doi.org/10.1126/science.1090922

Biffi, G., T.E. Oni, B. Spielman, Y. Hao, E. Elyada, Y. Park, J. Preall, and D.A. Tuveson. 2019. Il1-induced Jak/STAT signaling is antagonized by TGFβ to shape CAF heterogeneity in pancreatic ductal adenocarcinoma. *Cancer Discov.* 9:282–301. https://doi.org/10.1158/2159-8290.CD-18-0710

Błyszczuk, P., A. Kozlova, Z. Guo, G. Kania, and O. Distler. 2019. Experimental mouse model of bleomycin-induced skin fibrosis. *Curr. Protoc. Immunol.* 126:e88. https://doi.org/10.1002/cpim.88

Bonnardel, J., W. T'Jonck, D. Gaublomme, R. Browaeys, C.L. Scott, L. Martens, B. Vanneste, S. De Prijck, S.A. Nedospasov, A. Kremer, et al. 2019. Stellate cells, hepatocytes, and endothelial cells imprint the Kupffer cell identity on monocytes colonizing the liver macrophage niche. *Immunity.* 51:638–654.e9. https://doi.org/10.1016/j.immuni.2019.08.017

Bryant, D.H., A. Bashir, S. Sinai, N.K. Jain, P.J. Ogden, P.F. Riley, G.M. Church, L.J. Colwell, and E.D. Kelsic. 2021. Deep diversification of an AAV capsid protein by machine learning. *Nat. Biotechnol.* 39:691–696. https://doi.org/10.1038/s41587-020-00793-4

Buechler, M.B., W. Fu, and S.J. Turley. 2021a. Fibroblast-macrophage reciprocal interactions in health, fibrosis, and cancer. *Immunity.* 54:903–915. https://doi.org/10.1016/j.immuni.2021.04.021

Buechler, M.B., R.N. Pradhan, A.T. Krishnamurty, C. Cox, A.K. Calviello, A.W. Wang, Y.A. Yang, L. Tam, R. Caothien, M. Roose-Girma, et al. 2021b. Cross-tissue organization of the fibroblast lineage. *Nature.* 593:575–579. https://doi.org/10.1038/s41586-021-03549-5

Camara Serrano, J.A. 2022. Ultrasound guided surgery as a refinement tool in oncology Research. *Animals.* 12:3445. https://doi.org/10.3390/ani12233445

Cao, J., M. Spielmann, X. Qiu, X. Huang, D.M. Ibrahim, A.J. Hill, F. Zhang, S. Mundlos, L. Christiansen, F.J. Steemers, et al. 2019. The single-cell transcriptional landscape of mammalian organogenesis. *Nature.* 566: 496–502. https://doi.org/10.1038/s41586-019-0969-x

Chakravarthy, A., L. Khan, N.P. Bensler, P. Bose, and D.D. De Carvalho. 2018. TGF-β-associated extracellular matrix genes link cancer-associated fibroblasts to immune evasion and immunotherapy failure. *Nat. Commun.* 9:4692. https://doi.org/10.1038/s41467-018-06654-8

Challis, R.C., S. Ravindra Kumar, X. Chen, D. Goertsen, G.M. Coughlin, A.M. Hori, M.R. Chuapoco, T.S. Otis, T.F. Miles, and V. Gradinaru. 2022. Adeno-associated virus toolkit to target diverse brain cells. *Annu. Rev. Neurosci.* 45:447–469. https://doi.org/10.1146/annurev-neuro-111020-100834

Chen, Y., J. Kim, S. Yang, H. Wang, C.-J. Wu, H. Sugimoto, V.S. LeBleu, and R. Kalluri. 2021. Type I collagen deletion in αSMA$^+$ myofibroblasts augments immune suppression and accelerates progression of pancreatic cancer. *Cancer Cell.* 39:548–565.e6. https://doi.org/10.1016/j.ccell.2021.02.007

Cheng, N., N.A. Bhowmick, A. Chytil, A.E. Gorksa, K.A. Brown, R. Muraoka, C.L. Arteaga, E.G. Neilson, S.W. Hayward, and H.L. Moses. 2005. Loss of TGF-beta type II receptor in fibroblasts promotes mammary carcinoma growth and invasion through upregulation of TGF-alpha-, MSP- and HGF-mediated signaling networks. *Oncogene.* 24:5053–5068. https://doi.org/10.1038/sj.onc.1208685

Chung, M.-I., M. Bujnis, C.E. Barkauskas, Y. Kobayashi, and B.L.M. Hogan. 2018. Niche-mediated BMP/SMAD signaling regulates lung alveolar stem cell proliferation and differentiation. *Development.* 145:dev163014. https://doi.org/10.1242/dev.163014

Chytil, A., M.A. Magnuson, C.V.E. Wright, and H.L. Moses. 2002. Conditional inactivation of the TGF-beta type II receptor using Cre:Lox. *Genesis.* 32: 73–75. https://doi.org/10.1002/gene.10046

Combes, A.J., B. Samad, J. Tsui, N.W. Chew, P. Yan, G.C. Reeder, D. Kushnoor, A. Shen, B. Davidson, A.J. Barczak, et al. 2022. Discovering dominant tumor immune archetypes in a pan-cancer census. *Cell.* 185:184–203.e19. https://doi.org/10.1016/j.cell.2021.12.004

DeBruine, Z.J., J.A. Pospisilik, and T.J. Triche. 2021. Fast and interpretable non-negative matrix factorization for atlas-scale single cell data. *bioRxiv.* https://doi.org/10.1101/2021.09.01.458620. (Preprint posted May 14, 2024).

Dominguez, C.X., S. Müller, S. Keerthivasan, H. Koeppen, J. Hung, S. Gierke, B. Breart, O. Foreman, T.W. Bainbridge, A. Castiglioni, et al. 2020. Single-cell RNA sequencing reveals stromal evolution into LRRC15$^+$ myofibroblasts as a determinant of patient response to cancer immunotherapy. *Cancer Discov.* 10:232–253. https://doi.org/10.1158/2159-8290.CD-19-0644

Eikesdal, H.P., L.M. Becker, Y. Teng, A. Kizu, J.L. Carstens, K. Kanasaki, H. Sugimoto, V.S. LeBleu, and R. Kalluri. 2018. BMP7 signaling in TGFBR2-deficient stromal cells provokes epithelial carcinogenesis. *Mol. Cancer Res.* 16:1568–1578. https://doi.org/10.1158/1541-7786.MCR-18-0120

Ellis, B.L., M.L. Hirsch, J.C. Barker, J.P. Connelly, R.J. Steininger, and M.H. Porteus. 2013. A survey of ex vivo/in vitro transduction efficiency of mammalian primary cells and cell lines with Nine natural adeno-associated virus (AAV1-9) and one engineered adeno-associated virus serotype. *Virol. J.* 10:74. https://doi.org/10.1186/1743-422X-10-74

Elyada, E., M. Bolisetty, P. Laise, W.F. Flynn, E.T. Courtois, R.A. Burkhart, J.A. Teinor, P. Belleau, G. Biffi, M.S. Lucito, et al. 2019. Cross-species single-cell analysis of pancreatic ductal adenocarcinoma reveals antigen-presenting cancer-associated fibroblasts. *Cancer Discov.* 9:1102–1123. https://doi.org/10.1158/2159-8290.CD-19-0094

Ewing-Crystal, N.A., N.M. Mroz, A. Larpthaveesarp, C.O. Lizama, R. Pennington, P. Chiaranunt, J.I. Dennis, A.A. Chang, E.D. Merrill, S.E. Caryotakis, et al. 2025. Dynamic fibroblast-immune interactions shape recovery after brain injury. *Nature*. 646:934–944. https://doi.org/10.1038/s41586-025-09449-2

Federico, A., and S. Monti. 2020. hypeR: an R package for geneset enrichment workflows. *Bioinformatics*. 36:1307–1308. https://doi.org/10.1093/bioinformatics/btz700

Finak, G., A. McDavid, M. Yajima, J. Deng, V. Gersuk, A.K. Shalek, C.K. Slichter, H.W. Miller, M.J. McElrath, M. Prlic, et al. 2015. MAST: A flexible statistical framework for assessing transcriptional changes and characterizing heterogeneity in single-cell RNA sequencing data. *Genome Biol.* 16:278. https://doi.org/10.1186/s13059-015-0844-5

Foster, D.S., M. Januszyk, K.E. Yost, M.S. Chinta, G.S. Gulati, A.T. Nguyen, A.R. Burcham, A. Salhotra, R.C. Ransom, D. Henn, et al. 2021. Integrated spatial multiomics reveals fibroblast fate during tissue repair. *Proc. Natl. Acad. Sci. USA*. 118:e2110025118. https://doi.org/10.1073/pnas.2110025118

Francisco, J., Y. Zhang, Y. Nakada, J.I. Jeong, C.-Y. Huang, A. Ivessa, S. Oka, G.J. Babu, and D.P. Del Re. 2021. AAV-mediated YAP expression in cardiac fibroblasts promotes inflammation and increases fibrosis. *Sci. Rep.* 11:10553. https://doi.org/10.1038/s41598-021-89989-5

Franklin, R.A. 2021. Fibroblasts and macrophages: Collaborators in tissue homeostasis. *Immunol. Rev.* 302:86–103. https://doi.org/10.1111/imr.12989

Gao, Y., J. Li, W. Cheng, T. Diao, H. Liu, Y. Bo, C. Liu, W. Zhou, M. Chen, Y. Zhang, et al. 2024. Cross-tissue human fibroblast atlas reveals myofibroblast subtypes with distinct roles in immune modulation. *Cancer Cell*. 42:1764–1783.e10. https://doi.org/10.1016/j.ccell.2024.08.020

Gibson, D.G., L. Young, R.-Y. Chuang, J.C. Venter, C.A. Hutchison, and H.O. Smith. 2009. Enzymatic assembly of DNA molecules up to several hundred kilobases. *Nat. Methods*. 6:343–345. https://doi.org/10.1038/nmeth.1318

Gray, S.J., S.B. Foti, J.W. Schwartz, L. Bachaboina, B. Taylor-Blake, J. Coleman, M.D. Ehlers, M.J. Zylka, T.J. McCown, and R.J. Samulski. 2011. Optimizing promoters for recombinant adeno-associated virus-mediated gene expression in the peripheral and central nervous system using self-complementary vectors. *Hum. Gene Ther.* 22:1143–1153. https://doi.org/10.1089/hum.2010.245

Griffith, J.W., C.L. Sokol, and A.D. Luster. 2014. Chemokines and chemokine receptors: Positioning cells for host defense and immunity. *Annu. Rev. Immunol.* 32:659–702. https://doi.org/10.1146/annurev-immunol-032713-120145

Grimm, D., J.S. Lee, L. Wang, T. Desai, B. Akache, T.A. Storm, and M.A. Kay. 2008. In vitro and in vivo gene therapy vector evolution via multispecies interbreeding and retargeting of adeno-associated viruses. *J. Virol.* 82:5887–5911. https://doi.org/10.1128/JVI.00254-08

Grout, J.A., P. Sirven, A.M. Leader, S. Maskey, E. Hector, I. Puisieux, F. Steffan, E. Cheng, N. Tung, M. Maurin, et al. 2022. Spatial positioning and matrix programs of cancer-associated fibroblasts promote T-cell exclusion in human lung tumors. *Cancer Discov.* 12:2606–2625. https://doi.org/10.1158/2159-8290.CD-21-1714

Guerrero-Juarez, C.F., P.H. Dedhia, S. Jin, R. Ruiz-Vega, D. Ma, Y. Liu, K. Yamaga, O. Shestova, D.L. Gay, Z. Yang, et al. 2019. Single-cell analysis reveals fibroblast heterogeneity and myeloid-derived adipocyte progenitors in murine skin wounds. *Nat. Commun.* 10:650. https://doi.org/10.1038/s41467-018-08247-x

Gungabeesoon, J., N.A. Gort-Freitas, M. Kiss, E. Bolli, M. Messemaker, M. Siwicki, M. Hicham, R. Bill, P. Koch, C. Cianciaruso, et al. 2023. A neutrophil response linked to tumor control in immunotherapy. *Cell*. 186:1448–1464.e20. https://doi.org/10.1016/j.cell.2023.02.032

Guy, C.T., R.D. Cardiff, and W.J. Muller. 1992. Induction of mammary tumors by expression of polyomavirus middle T oncogene: A transgenic mouse model for metastatic disease. *Mol. Cell. Biol.* 12:954–961. https://doi.org/10.1128/mcb.12.3.954-961.1992

Han, X., Z. Zhang, L. He, H. Zhu, Yan Li, W. Pu, M. Han, H. Zhao, K. Liu, Yi Li, et al. 2021. A suite of new Dre recombinase drivers markedly expands the ability to perform intersectional genetic targeting. *Cell Stem Cell*. 28:1160–1176.e7. https://doi.org/10.1016/j.stem.2021.01.007

Hao, Y., T. Stuart, M.H. Kowalski, S. Choudhary, P. Hoffman, A. Hartman, A. Srivastava, G. Molla, S. Madad, C. Fernandez-Granda, and R. Satija. 2024. Dictionary learning for integrative, multimodal and scalable single-cell analysis. *Nat. Biotechnol.* 42:293–304. https://doi.org/10.1038/s41587-023-01767-y

He, L., X. Huang, O. Kanisicak, Yi Li, Y. Wang, Yan Li, W. Pu, Q. Liu, H. Zhang, X. Tian, et al. 2017. Preexisting endothelial cells mediate cardiac neovascularization after injury. *J. Clin. Invest.* 127:2968–2981. https://doi.org/10.1172/JCI93868

Helms, E.J., M.W. Berry, R.C. Chaw, C.C. DuFort, D. Sun, M.K. Onate, C. Oon, S. Bhattacharyya, H. Sanford-Crane, W. Horton, et al. 2022. Mesenchymal lineage heterogeneity underlies nonredundant functions of pancreatic cancer-associated fibroblasts. *Cancer Discov.* 12:484–501. https://doi.org/10.1158/2159-8290.CD-21-0601

Henderson, N.C., F. Rieder, and T.A. Wynn. 2020. Fibrosis: From mechanisms to medicines. *Nature*. 587:555–566. https://doi.org/10.1038/s41586-020-2938-9

Hinz, B., G. Celetta, J.J. Tomasek, G. Gabbiani, and C. Chaponnier. 2001. Alpha-smooth muscle actin expression upregulates fibroblast contractile activity. *Mol. Biol. Cell*. 12:2730–2741. https://doi.org/10.1091/mbc.12.9.2730

Hu, K.H., N.F. Kuhn, T. Courau, J. Tsui, B. Samad, P. Ha, J.R. Kratz, A.J. Combes, and M.F. Krummel. 2023. Transcriptional space-time mapping identifies concerted immune and stromal cell patterns and gene programs in wound healing and cancer. *Cell Stem Cell*. 30:885–903.e10. https://doi.org/10.1016/j.stem.2023.05.001

Hutton, C., F. Heider, A. Blanco-Gomez, A. Banyard, A. Kononov, X. Zhang, S. Karim, V. Paulus-Hock, D. Watt, N. Steele, et al. 2021. Single-cell analysis defines a pancreatic fibroblast lineage that supports anti-tumor immunity. *Cancer Cell*. 39:1227–1244.e20. https://doi.org/10.1016/j.ccell.2021.06.017

Hwang, W.L., K.A. Jagadeesh, J.A. Guo, H.I. Hoffman, P. Yadollahpour, J.W. Reeves, R. Mohan, E. Drokhlyansky, N. Van Wittenberghe, O. Ashenberg, et al. 2022. Single-nucleus and spatial transcriptome profiling of pancreatic cancer identifies multicellular dynamics associated with neoadjuvant treatment. *Nat. Genet.* 54:1178–1191. https://doi.org/10.1038/s41588-022-01134-8

Isgrig, K., D.S. McDougald, J. Zhu, H.J. Wang, J. Bennett, and W.W. Chien. 2019. AAV2.7m8 is a powerful viral vector for inner ear gene therapy. *Nat. Commun.* 10:427. https://doi.org/10.1038/s41467-018-08243-1

Jin, S., C.F. Guerrero-Juarez, L. Zhang, I. Chang, R. Ramos, C.H. Kuan, P. Myung, M.V. Plikus, and Q. Nie. 2021. Inference and analysis of cell-cell communication using CellChat. *Nat. Commun.* 12:1088. https://doi.org/10.1038/s41467-021-21246-9

Kilian, M., R. Sheinin, C.L. Tan, M. Friedrich, C. Krämer, A. Kaminitz, K. Sanghvi, K. Lindner, Y.-C. Chih, F. Cichon, et al. 2023. MHC class II-restricted antigen presentation is required to prevent dysfunction of cytotoxic T cells by blood-borne myeloids in brain tumors. *Cancer Cell*. 41:235–251.e9. https://doi.org/10.1016/j.ccell.2022.12.007

Kinchen, J., H.H. Chen, K. Parikh, A. Antanaviciute, M. Jagielowicz, D. Fawkner-Corbett, N. Ashley, L. Cubitt, E. Mellado-Gomez, M. Attar, et al. 2018. Structural remodeling of the human colonic mesenchyme in inflammatory bowel disease. *Cell*. 175:372–386.e17. https://doi.org/10.1016/j.cell.2018.08.067

Kolberg, L., U. Raudvere, and I. Kuzmin. 2019. *gprofiler2: Interface to the "g: Profiler" Toolset. CRAN: Contributed Packages*. https://CRAN.R-project.org/package=gprofiler2

Koncina, E., M. Nurmik, V.I. Pozdeev, C. Gilson, M. Tsenkova, R. Begaj, S. Stang, A. Gaigneaux, C. Weindorfer, F. Rodriguez, et al. 2023. IL1R1^{+} cancer-associated fibroblasts drive tumor development and immunosuppression in colorectal cancer. *Nat. Commun.* 14:4251. https://doi.org/10.1038/s41467-023-39953-w

Korsunsky, I., K. Wei, M. Pohin, E.Y. Kim, F. Barone, T. Major, E. Taylor, R. Ravindran, S. Kemble, G.F.M. Watts, et al. 2022. Cross-tissue, single-cell stromal atlas identifies shared pathological fibroblast phenotypes in four chronic inflammatory diseases. *Med.* 3:481–518.e14. https://doi.org/10.1016/j.medj.2022.05.002

Krishnamurty, A.T., J.A. Shyer, M. Thai, V. Gandham, M.B. Buechler, Y.A. Yang, R.N. Pradhan, A.W. Wang, P.L. Sanchez, Y. Qu, et al. 2022.

LRRC15⁺ myofibroblasts dictate the stromal setpoint to suppress tumour immunity. *Nature*. 611:148–154. https://doi.org/10.1038/s41586-022-05272-1

Laklai, H., Y.A. Miroshnikova, M.W. Pickup, E.A. Collisson, G.E. Kim, A.S. Barrett, R.C. Hill, J.N. Lakins, D.D. Schlaepfer, J.K. Mouw, et al. 2016. Genotype tunes pancreatic ductal adenocarcinoma tissue tension to induce matricellular fibrosis and tumor progression. *Nat. Med.* 22: 497–505. https://doi.org/10.1038/nm.4082

Lee, B.Y., E.K.J. Hogg, C.R. Below, A. Kononov, A. Blanco-Gomez, F. Heider, J. Xu, C. Hutton, X. Zhang, T. Scheidt, et al. 2021. Heterocellular OSM-OSMR signalling reprograms fibroblasts to promote pancreatic cancer growth and metastasis. *Nat. Commun.* 12:7336. https://doi.org/10.1038/s41467-021-27607-8

Lin, W., P. Noel, E.H. Borazanci, J. Lee, A. Amini, I.W. Han, J.S. Heo, G.S. Jameson, C. Fraser, M. Steinbach, et al. 2020. Single-cell transcriptome analysis of tumor and stromal compartments of pancreatic ductal adenocarcinoma primary tumors and metastatic lesions. *Genome Med.* 12: 80. https://doi.org/10.1186/s13073-020-00776-9

Luca, B.A., C.B. Steen, M. Matusiak, A. Azizi, S. Varma, C. Zhu, J. Przybyl, A. Espín-Pérez, M. Diehn, A.A. Alizadeh, et al. 2021. Atlas of clinically distinct cell states and ecosystems across human solid tumors. *Cell*. 184: 5482–5496.e28. https://doi.org/10.1016/j.cell.2021.09.014

Maheshri, N., J.T. Koerber, B.K. Kaspar, and D.V. Schaffer. 2006. Directed evolution of adeno-associated virus yields enhanced gene delivery vectors. *Nat. Biotechnol.* 24:198–204. https://doi.org/10.1038/nbt1182

Mancarci, O. 2018. Homologene: Quick access to homologene and gene annotation updates. CRAN: Contributed Packages. https://CRAN.R-project.org/package=homologene

Mariathasan, S., S.J. Turley, D. Nickles, A. Castiglioni, K. Yuen, Y. Wang, E.E. Kadel 3rd, H. Koeppen, J.L. Astarita, R. Cubas, et al. 2018. TGFβ attenuates tumour response to PD-L1 blockade by contributing to exclusion of T cells. *Nature*. 554:544–548. https://doi.org/10.1038/nature25501

Mascharak, S., H.E. des Jardins-Park, M.F. Davitt, M. Griffin, M.R. Borrelli, A.L. Moore, K. Chen, B. Duoto, M. Chinta, D.S. Foster, et al. 2021. Preventing *Engrailed*-1 activation in fibroblasts yields wound regeneration without scarring. *Science*. 372:eaba2374. https://doi.org/10.1126/science.aba2374

Massagué, J., and Y.-G. Chen. 2000. Controlling TGF-β signaling. *Genes & Dev.* 14:627–644. https://doi.org/10.1101/gad.14.6.627

Massagué, J., and D. Sheppard. 2023. TGF-β signaling in health and disease. *Cell*. 186:4007–4037. https://doi.org/10.1016/j.cell.2023.07.036

Mayer, S., T. Milo, A. Isaacson, C. Halperin, S. Miyara, Y. Stein, C. Lior, M. Pevsner-Fischer, E. Tzahor, A. Mayo, et al. 2023. The tumor microenvironment shows a hierarchy of cell-cell interactions dominated by fibroblasts. *Nat. Commun.* 14:5810. https://doi.org/10.1038/s41467-023-41518-w

McAndrews, K.M., Y. Chen, J.K. Darpolor, X. Zheng, S. Yang, J.L. Carstens, B. Li, H. Wang, T. Miyake, P. Correa de Sampaio, et al. 2022. Identification of functional heterogeneity of carcinoma-associated fibroblasts with distinct IL6-mediated therapy resistance in pancreatic cancer. *Cancer Discov.* 12:1580–1597. https://doi.org/10.1158/2159-8290.CD-20-1484

McCarty, D., P. Monahan, and R. Samulski. 2001. Self-complementary recombinant adeno-associated virus (scAAV) vectors promote efficient transduction independently of DNA synthesis. *Gene Ther.* 8:1248–1254. https://doi.org/10.1038/sj.gt.3301514

McCarty, D.M. 2008. Self-complementary AAV vectors; advances and applications. *Mol. Ther.* 16:1648–1656. https://doi.org/10.1038/mt.2008.171

McCarty, D.M., H. Fu, P.E. Monahan, C.E. Toulson, P. Naik, and R.J. Samulski. 2003. Adeno-associated virus terminal repeat (TR) mutant generates self-complementary vectors to overcome the rate-limiting step to transduction in vivo. *Gene Ther.* 10:2112–2118. https://doi.org/10.1038/sj.gt.3302134

McCarty, N.S., A.E. Graham, L. Studená, and R. Ledesma-Amaro. 2020. Multiplexed CRISPR technologies for gene editing and transcriptional regulation. *Nat. Commun.* 11:1281. https://doi.org/10.1038/s41467-020-15053-x

Meeth, K., J.X. Wang, G. Micevic, W. Damsky, and M.W. Bosenberg. 2016. The YUMM lines: A series of congenic mouse melanoma cell lines with defined genetic alterations. *Pigment Cell Melanoma Res.* 29:590–597. https://doi.org/10.1111/pcmr.12498

Moncada, R., D. Barkley, F. Wagner, M. Chiodin, J.C. Devlin, M. Baron, C.H. Hajdu, D.M. Simeone, and I. Yanai. 2020. Integrating microarray-based spatial transcriptomics and single-cell RNA-seq reveals tissue architecture in pancreatic ductal adenocarcinomas. *Nat. Biotechnol.* 38: 333–342. https://doi.org/10.1038/s41587-019-0392-8

Mosa, M.H., B.E. Michels, C. Menche, A.M. Nicolas, T. Darvishi, F.R. Greten, and H.F. Farin. 2020. A Wnt-induced phenotypic switch in cancer-associated fibroblasts inhibits EMT in colorectal cancer. *Cancer Res.* 80:5569–5582. https://doi.org/10.1158/0008-5472.CAN-20-0263

Nicolas, A.M., M. Pesic, E. Engel, P.K. Ziegler, M. Diefenhardt, K.B. Kennel, F. Buettner, C. Conche, V. Petrocelli, E. Elwakeel, et al. 2022. Inflammatory fibroblasts mediate resistance to neoadjuvant therapy in rectal cancer. *Cancer Cell*. 40:168–184.e13. https://doi.org/10.1016/j.ccell.2022.01.004

Nyberg, W.A., J. Ark, A. To, S. Clouden, G. Reeder, J.J. Muldoon, J.-Y. Chung, W.H. Xie, V. Allain, Z. Steinhart, et al. 2023. An evolved AAV variant enables efficient genetic engineering of murine T cells. *Cell*. 186: 446–460.e19. https://doi.org/10.1016/j.cell.2022.12.022

Öhlund, D., A. Handly-Santana, G. Biffi, E. Elyada, A.S. Almeida, M. Ponz-Sarvise, V. Corbo, T.E. Oni, S.A. Hearn, E.J. Lee, et al. 2017. Distinct populations of inflammatory fibroblasts and myofibroblasts in pancreatic cancer. *J. Exp. Med.* 214:579–596. https://doi.org/10.1084/jem.20162024

Pelka, K., M. Hofree, J.H. Chen, S. Sarkizova, J.D. Pirl, V. Jorgji, A. Bejnood, D. Dionne, W.H. Ge, K.H. Xu, et al. 2021. Spatially organized multicellular immune hubs in human colorectal cancer. *Cell*. 184:4734–4752.e20. https://doi.org/10.1016/j.cell.2021.08.003

Peng, J., B.-F. Sun, C.-Y. Chen, J.-Y. Zhou, Y.-S. Chen, H. Chen, L. Liu, D. Huang, J. Jiang, G.-S. Cui, et al. 2019. Single-cell RNA-seq highlights intra-tumoral heterogeneity and malignant progression in pancreatic ductal adenocarcinoma. *Cell Res.* 29:725–738. https://doi.org/10.1038/s41422-019-0195-y

Pinkard, H., N. Stuurman, K. Corbin, R. Vale, and M.F. Krummel. 2016. Micromagellan: Open-source, sample-adaptive, acquisition software for optical microscopy. *Nat. Methods*. 13:807–809. https://doi.org/10.1038/nmeth.3991

Platt, R.J., S. Chen, Y. Zhou, M.J. Yim, L. Swiech, H.R. Kempton, J.E. Dahlman, O. Parnas, T.M. Eisenhaure, M. Jovanovic, et al. 2014. CRISPR-Cas9 knockin mice for genome editing and cancer modeling. *Cell*. 159: 440–455. https://doi.org/10.1016/j.cell.2014.09.014

Plikus, M.V., X. Wang, S. Sinha, E. Forte, S.M. Thompson, E.L. Herzog, R.R. Driskell, N. Rosenthal, J. Biernaskie, and V. Horsley. 2021. Fibroblasts: Origins, definitions, and functions in health and disease. *Cell*. 184: 3852–3872. https://doi.org/10.1016/j.cell.2021.06.024

Qiu, X., Q. Mao, Y. Tang, L. Wang, R. Chawla, H.A. Pliner, and C. Trapnell. 2017. Reversed graph embedding resolves complex single-cell trajectories. *Nat. Methods*. 14:979–982. https://doi.org/10.1038/nmeth.4402

Qiu, C., J. Cao, B.K. Martin, T. Li, I.C. Welsh, S. Srivatsan, X. Huang, D. Calderon, W.S. Noble, C.M. Disteche, et al. 2022. Systematic reconstruction of cellular trajectories across mouse embryogenesis. *Nat. Genet.* 54: 328–341. https://doi.org/10.1038/s41588-022-01018-x

Raghavan, S., P.S. Winter, A.W. Navia, H.L. Williams, A. DenAdel, K.E. Lowder, J. Galvez-Reyes, R.L. Kalekar, N. Mulugeta, K.S. Kapner, et al. 2021. Microenvironment drives cell state, plasticity, and drug response in pancreatic cancer. *Cell*. 184:6119–6137.e26. https://doi.org/10.1016/j.cell.2021.11.017

Rajendran, V., P. Ramesh, R. Dai, S. Kalgudde Gopal, H. Ye, H.-G. Machens, H. Adler, D. Jiang, and Y. Rinkevich. 2023. Therapeutic silencing of p120 in fascia fibroblasts ameliorates tissue repair. *J. Invest. Dermatol.* 143: 854–863.e4. https://doi.org/10.1016/j.jid.2022.10.018

Rezvani, M., R. Español-Suñer, Y. Malato, L. Dumont, A.A. Grimm, E. Kienle, J.G. Bindman, E. Wiedtke, B.Y. Hsu, S.J. Naqvi, et al. 2016. In vivo hepatic reprogramming of myofibroblasts with AAV vectors as a therapeutic strategy for liver fibrosis. *Cell Stem Cell*. 18:809–816. https://doi.org/10.1016/j.stem.2016.05.005

Roberts, E.W., A. Deonarine, J.O. Jones, A.E. Denton, C. Feig, S.K. Lyons, M. Espeli, M. Kraman, B. McKenna, R.J.B. Wells, et al. 2013. Depletion of stromal cells expressing fibroblast activation protein-α from skeletal muscle and bone marrow results in cachexia and anemia. *J. Exp. Med.* 210:1137–1151. https://doi.org/10.1084/jem.20122344

Roesch, K., A.P. Jadhav, J.M. Trimarchi, M.B. Stadler, B. Roska, B.B. Sun, and C.L. Cepko. 2008. The transcriptome of retinal Müller glial cells. *J. Comp. Neurol.* 509:225–238. https://doi.org/10.1002/cne.21730

Sahai, E., I. Astsaturov, E. Cukierman, D.G. DeNardo, M. Egeblad, R.M. Evans, D. Fearon, F.R. Greten, S.R. Hingorani, T. Hunter, et al. 2020. A framework for advancing our understanding of cancer-associated fibroblasts. *Nat. Rev. Cancer* 20:174–186. https://doi.org/10.1038/s41568-019-0238-1

Schönhuber, N., B. Seidler, K. Schuck, C. Veltkamp, C. Schachtler, M. Zukowska, S. Eser, T.B. Feyerabend, M.C. Paul, P. Eser, et al. 2014. A next-generation dual-recombinase system for time- and host-specific targeting of pancreatic cancer. *Nat. Med.* 20:1340–1347. https://doi.org/10.1038/nm.3646

Sherman, M.H., and M.P. di Magliano. 2023. Cancer-associated fibroblasts: Lessons from pancreatic cancer. *Annu. Rev. Cancer Biol.* 7:43–55. https://doi.org/10.1146/annurev-cancerbio-061421-035400

Shirley, J.L., Y.P. de Jong, C. Terhorst, and R.W. Herzog. 2020. Immune responses to viral gene therapy vectors. *Mol. Ther.* 28:709–722. https://doi.org/10.1016/j.ymthe.2020.01.001

Simoncello, F., G.M. Piperno, N. Caronni, R. Amadio, A. Cappelletto, G. Canarutto, S. Piazza, S. Bicciato, and F. Benvenuti. 2022. CXCL5-mediated accumulation of mature neutrophils in lung cancer tissues impairs the differentiation program of anticancer CD8 T cells and limits the efficacy of checkpoint inhibitors. *Oncoimmunology*. 11:2059876. https://doi.org/10.1080/2162402X.2022.2059876

Song, G., M. Pacher, A. Balakrishnan, Q. Yuan, H.-C. Tsay, D. Yang, J. Reetz, S. Brandes, Z. Dai, B.M. Pützer, et al. 2016. Direct reprogramming of hepatic myofibroblasts into hepatocytes in vivo attenuates liver fibrosis. *Cell Stem Cell*. 18:797–808. https://doi.org/10.1016/j.stem.2016.01.010

Steele, N.G., E.S. Carpenter, S.B. Kemp, V.R. Sirihorachai, S. The, L. Delrosario, J. Lazarus, E.D. Amir, V. Gunchick, C. Espinoza, et al. 2020. Multimodal mapping of the tumor and peripheral blood immune landscape in human pancreatic cancer. *Nat. Cancer*. 1:1097–1112. https://doi.org/10.1038/s43018-020-00121-4

Stein-O'Brien, G.L., R. Arora, A.C. Culhane, A.V. Favorov, L.X. Garmire, C.S. Greene, L.A. Goff, Y. Li, A. Ngom, M.F. Ochs, et al. 2018. Enter the matrix: Factorization uncovers knowledge from omics. *Trends Genet.* 34:790–805. https://doi.org/10.1016/j.tig.2018.07.003

Suzuki, K., Y. Tsunekawa, R. Hernandez-Benitez, J. Wu, J. Zhu, E.J. Kim, F. Hatanaka, M. Yamamoto, T. Araoka, Z. Li, et al. 2016. In vivo genome editing via CRISPR/Cas9 mediated homology-independent targeted integration. *Nature*. 540:144–149. https://doi.org/10.1038/nature20565

Tabebordbar, M., K.A. Lagerborg, A. Stanton, E.M. King, S. Ye, L. Tellez, A. Krunnfusz, S. Tavakoli, J.J. Widrick, K.A. Messemer, et al. 2021. Directed evolution of a family of AAV capsid variants enabling potent muscle-directed gene delivery across species. *Cell*. 184:4919–4938.e22. https://doi.org/10.1016/j.cell.2021.08.028

Trapnell, C., D. Cacchiarelli, J. Grimsby, P. Pokharel, S. Li, M. Morse, N.J. Lennon, K.J. Livak, T.S. Mikkelsen, and J.L. Rinn. 2014. The dynamics and regulators of cell fate decisions are revealed by pseudotemporal ordering of single cells. *Nat. Biotechnol.* 32:381–386. https://doi.org/10.1038/nbt.2859

Tsukui, T., K.H. Sun, J.B. Wetter, J.R. Wilson-Kanamori, L.A. Hazelwood, N.C. Henderson, T.S. Adams, J.C. Schupp, S.D. Poli, I.O. Rosas, et al. 2020. Collagen-producing lung cell atlas identifies multiple subsets with distinct localization and relevance to fibrosis. *Nat. Commun.* 11:1920. https://doi.org/10.1038/s41467-020-15647-5

Tsukui, T., P.J. Wolters, and D. Sheppard. 2024. Alveolar fibroblast lineage orchestrates lung inflammation and fibrosis. *Nature*. 631:627–634. https://doi.org/10.1038/s41586-024-07660-1

Tyler, M., A. Gavish, C. Barbolin, R. Tschernichovsky, R. Hoefflin, M. Mints, S.V. Puram, and I. Tirosh. 2025. The Curated Cancer Cell Atlas provides a comprehensive characterization of tumors at single-cell resolution. *Nat. Cancer*. 6:1088–1101. https://doi.org/10.1038/s43018-025-00957-8

Vivian, J., A.A. Rao, F.A. Nothaft, C. Ketchum, J. Armstrong, A. Novak, J. Pfeil, J. Narkizian, A.D. Deran, A. Musselman-Brown, et al. 2017. Toil enables reproducible, open source, big biomedical data analyses. *Nat. Biotechnol.* 35:314–316. https://doi.org/10.1038/nbt.3772

Wang, Z., H.-I. Ma, J. Li, L. Sun, J. Zhang, and X. Xiao. 2003. Rapid and highly efficient transduction by double-stranded adeno-associated virus vectors in vitro and in vivo. *Gene Ther.* 10:2105–2111. https://doi.org/10.1038/sj.gt.3302133

Wang, B., Q. Li, L. Qin, S. Zhao, J. Wang, and X. Chen. 2011. Transition of tumor-associated macrophages from MHC class II(hi) to MHC class II(low) mediates tumor progression in mice. *BMC Immunol.* 12:43. https://doi.org/10.1186/1471-2172-12-43

Wang, D., P.W.L. Tai, and G. Gao. 2019. Adeno-associated virus vector as a platform for gene therapy delivery. *Nat. Rev. Drug Discov.* 18:358–378. https://doi.org/10.1038/s41573-019-0012-9

Wang, X., B.-L. Xu, and X.-W. Chen. 2021. Acute gene inactivation in the adult mouse liver using the CRISPR-Cas9 technology. *STAR Protoc.* 2:100611. https://doi.org/10.1016/j.xpro.2021.100611

Wei, T., and Simko, V., 2010. Corrplot: Visualization of a Correlation Matrix. CRAN: Contributed Packages. https://CRAN.R-project.org/package=corrplot

Westhaus, A., M. Cabanes-Creus, A. Rybicki, G. Baltazar, R.G. Navarro, E. Zhu, M. Drouyer, M. Knight, R.F. Albu, B.H. Ng, et al. 2020. High-throughput *in vitro*, *ex vivo*, and *in vivo* screen of adeno-associated virus vectors based on physical and functional transduction. *Hum. Gene Ther.* 31:575–589. https://doi.org/10.1089/hum.2019.264

Wu, F., J. Yang, J. Liu, Y. Wang, J. Mu, Q. Zeng, S. Deng, and H. Zhou. 2021. Signaling pathways in cancer-associated fibroblasts and targeted therapy for cancer. *Signal. Transduct. Target. Ther.* 6:218. https://doi.org/10.1038/s41392-021-00641-0

Yamamoto, K., A. Venida, J. Yano, D.E. Biancur, M. Kakiuchi, S. Gupta, A.S.W. Sohn, S. Mukhopadhyay, E.Y. Lin, S.J. Parker, et al. 2020. Autophagy promotes immune evasion of pancreatic cancer by degrading MHC-I. *Nature*. 581:100–105. https://doi.org/10.1038/s41586-020-2229-5

Yang, L., J. Huang, X. Ren, A.E. Gorska, A. Chytil, M. Aakre, D.P. Carbone, L.M. Matrisian, A. Richmond, P.C. Lin, and H.L. Moses. 2008. Abrogation of TGF beta signaling in mammary carcinomas recruits Gr-1+CD11b+ myeloid cells that promote metastasis. *Cancer Cell*. 13:23–35. https://doi.org/10.1016/j.ccr.2007.12.004

Ye, J., J.M. Baer, D.V. Faget, V.A. Morikis, Q. Ren, A. Melam, A.P. Delgado, X. Luo, S.M. Bagchi, J.I. Belle, et al. 2024. Senescent CAFs mediate immunosuppression and drive breast cancer progression. *Cancer Discov.* 14:1302–1323. https://doi.org/10.1158/2159-8290.CD-23-0426

Zhou, S.-L., Z. Dai, Z.-J. Zhou, Q. Chen, Z. Wang, Y.-S. Xiao, Z.-Q. Hu, X.-Y. Huang, G.-H. Yang, Y.-H. Shi, et al. 2014. CXCL5 contributes to tumor metastasis and recurrence of intrahepatic cholangiocarcinoma by recruiting infiltrative intratumoral neutrophils. *Carcinogenesis*. 35:597–605. https://doi.org/10.1093/carcin/bgt397

Zhou, X., R.A. Franklin, M. Adler, J.B. Jacox, W. Bailis, J.A. Shyer, R.A. Flavell, A. Mayo, U. Alon, and R. Medzhitov. 2018. Circuit design features of a stable two-cell system. *Cell*. 172:744–757.e17. https://doi.org/10.1016/j.cell.2018.01.015

Zhu, S., W. Chen, A. Masson, and Y.-P. Li. 2024. Cell signaling and transcriptional regulation of osteoblast lineage commitment, differentiation, bone formation, and homeostasis. *Cell Discov.* 10:71. https://doi.org/10.1038/s41421-024-00689-6

Zimmerman, K.D., M.A. Espeland, and C.D. Langefeld. 2021. A practical solution to pseudoreplication bias in single-cell studies. *Nat. Commun.* 12:738. https://doi.org/10.1038/s41467-021-21038-1

JEM

Supplemental material

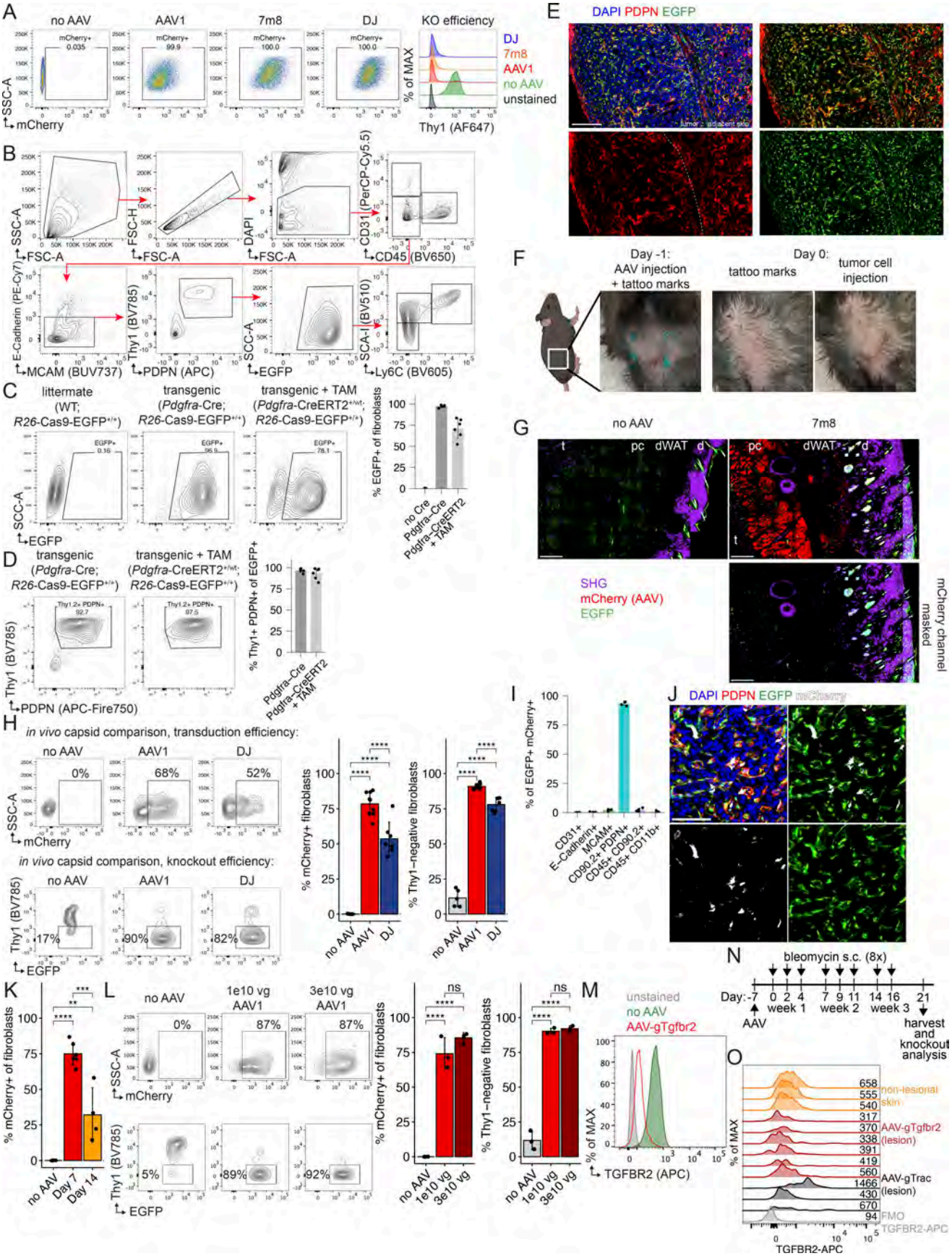

Figure S1. **Local injection of scAAV1-U6-gRNA into *Pdgfra*-Cre;*R26*-Cas9-EGFP mice allows efficient and specific *in vivo* gene editing of fibroblasts.** **(A)** NIH/3T3.Cas9 cells were transduced with three different self-complementary AAVs as outlined in Fig. 1 B, all carrying the same hU6-gThy1-CBh-mCherry cassette but generated with three different capsids (AAV1, 7m8, and DJ). Left: Flow cytometry plots depicting mCherry expression in NIH/3T3.Cas9 cells as a readout for transduction efficiency of AAVs after 96 h at an MOI of 1e5. Right: Flow cytometry overlay plots of those NIH/3T3.Cas9 cells showing KO efficiency of the AAVs with different capsids at day 6 after AAV transduction. One of two representative experiments is shown. **(B)** *In vivo* gating scheme to identify tumor fibroblasts: DAPI$^-$ CD31$^-$ CD45$^-$ E-Cadherin$^-$ MCAM$^-$ THY1$^+$ PDPN$^+$ EGFP$^+$ in *Pdgfra*-Cas9-EGFP mice. For *Col1a2*$^{CreERT2/+}$;*Tgfbr2*$^{fl/fl}$ mice in Fig. 1, O and P, tumor fibroblasts were gated as DAPI$^-$ CD31$^-$ CD45$^-$ E-Cadherin$^-$ MCAM$^-$ THY1$^+$ PDPN$^+$. **(C)** Left: Flow cytometry contour plots of EGFP expression in tumor fibroblasts (DAPI$^-$ CD31$^-$ CD45$^-$ E-Cadherin$^-$ MCAM$^-$ Thy1$^+$ PDPN$^+$) as gated in B on day 14 after 2.5e5 HY19636 pancreatic tumor cell s.c. injection in *Pdgfra*-Cre;*R26*-Cas9-EGFP$^{+/+}$ or *Pdgfra*-CreERT2$^{+/wt}$;*R26*-Cas9-EGFP$^{+/+}$ mice. *Pdgfra*-CreERT2$^{+/wt}$;*R26*-Cas9-EGFP$^{+/+}$ mice were injected with 2 mg of tamoxifen (TAM) on five consecutive days 1 wk prior to tumor engraftment to induce Cas9-EGFP expression. One of two representative experiments is shown. Right: Quantification of percentage of EGFP$^+$ tumor fibroblasts in *Pdgfra*-Cre;*R26*-Cas9-EGFP$^{+/+}$ mice or tamoxifen-treated *Pdgfra*-CreERT2$^{+/wt}$;*R26*-Cas9-EGFP$^{+/+}$ mice (n = 6/group, pooled from two independent experiments). Data are mean ± SD. **(D)** Left: Flow cytometry contour plots of fibroblast markers Thy1 and PDPN expression on DAPI$^-$ EGFP$^+$ cells from tumors in C. One of two representative experiments is shown. Right: Quantification of percentage of DP Thy1$^+$ PDPN$^+$ fibroblasts of DAPI$^-$ EGFP$^+$ cells in *Pdgfra*-Cre;*R26*-Cas9-EGFP$^{+/+}$ mice or tamoxifen-treated *Pdgfra*-CreERT2$^{+/wt}$;*R26*-Cas9-EGFP$^{+/+}$ mice (n = 6/group, pooled from two independent experiments). Data are mean ± SD. **(E)** Tumor cross-section of day 14 HY19636 s.c. tumor in Pdgfra-Cas9-EGFP mouse stained for PDPN and counterstained with DAPI. Dotted line demarcates tumor margin. Scale bar, 200 µm. **(F)** Pictures of subsequent injections of AAV and tumor cells on consecutive days to generate local gene KO in tumor fibroblasts. Local AAV injection is marked by tattoo paste using a 31-gauge needle on day −1 around wheal from AAV injection. Tattoo pricks are visible on day 0 and used as a guide for tumor cell injection that day. **(G)** Skin cross-sections of *Pdgfra*-Cas9-EGFP mice injected s.c. with 1e10 vg of scAAV with 7m8 capsid on day −1, 5e5 YUMM5.2 tumor cells were injected on day 0 at the same site, and cross-sections of skin plus tumor mass were generated 8 days later. The SHG (violet) signal to image fibrillar collagen is saturated in the dermis of the skin to visualize fibrillar collagen deposition in the deeper skin layers and the tumor mass. Red mCherry$^+$ signal highlights myocytes in panniculus carnosus infected with scAAV containing 7m8 capsid. Bright green signal in dermis is caused by autofluorescence of hairs. Scale bar, 250 µm. t, tumor; pc, panniculus carnosus; dWAT, dermal white adipose tissue; d, dermis. **(H)** Left: Flow cytometry contour plots of EGFP$^+$ tumor fibroblasts from *Pdgfra*-Cas9-EGFP mice injected s.c. with 1e10 vg scAAV-gThy1-CBh-mCherry (AAV1 or DJ capsid) on day −1 and 5e5 YUMM5.2 tumor cells on day 0. Tumors were excised on day 7 and (top) mCherry expression in tumor fibroblasts (gated as outlined in B) was measured as a readout for transduction efficiency and (bottom) surface level of Thy1 was measured as a readout for KO efficiency by the different AAV capsids. One of two representative experiments is shown. Right: Quantification of percentage transduction efficiency and KO efficiency plotted on the right (n = 5–9/group, pooled from two experiments). Data are mean ± SD, and significance was tested using one-way ANOVA with Tukey's multiple comparisons test. **(I)** *Pdgfra*-Cas9-EGFP mice were injected with 1e10 vg scAAV1-gTrac-CBh-mCherry s.c. and then challenged with 2.5e5 HY19636 cells the next day at the same s.c. site. On day 14 after tumor injection, AAV1-infected DAPI$^-$ EGFP$^+$ mCherry$^+$ cells were identified by flow cytometry. The bar plot quantifies distribution of the following cell types within that gate: CD45$^-$ CD31$^+$ (endothelial cells), CD45$^-$ CD31$^-$ E-Cadherin$^+$, CD45$^-$ CD31$^-$ MCAM$^+$, CD45$^-$ CD31$^-$ E-Cadherin$^-$ MCAM$^-$ CD90.2$^+$ PDPN$^+$ (CAFs), CD45$^+$ CD90.2$^+$ (non-B cell lymphoid), and CD45$^+$ CD11b (myeloid). Data mean ± SD (n = 4/group). One of two representative experiments is shown. **(J)** Immunofluorescence image of day 14 HY19636 s.c. tumor in *Pdgfra*-Cas9-EGFP mouse treated with scAAV1-gRNA-CBh-mCherry as outlined in F and stained for PDPN and counterstained with DAPI. Scale bar, 100 µm. **(K)** Quantification of mCherry$^+$ cells in all EGFP$^+$ tumor fibroblasts on day 7 or 14 after treatment with scAAV1-gRNA-CBh-mCherry and tumor challenge as outlined in F (n = 4–6/group). One of three representative experiments is shown. Data are mean ± SD, and significance was tested using one-way ANOVA with Tukey's multiple comparisons test. **P < 0.01, ***P < 0.001, and ****P < 0.0001. **(L)** Test of different scAAV1 doses for transduction and KO in tumor fibroblasts. *Pdgfra*-Cas9-EGFP mice were injected s.c. on day −1 with 1e10 or 3e10 vg of scAAV1-gThy1-CBh-mCherry (scAAV carrying gRNA-targeting *Thy1* and an mCherry ORF). On day 0, 5e5 YUMM5.2 cells were injected s.c. at site of prior AAV injection. Tumors were harvested on day 7, and transduction and *Thy1* KO efficiency were assessed. Top: flow cytometry contour plots of all tumor fibroblasts (gated as outlined in B) showing mCherry expression. Left: Flow cytometry plots of all tumor fibroblasts for THY1 surface expression. Right: Quantification of transduction and KO efficiency at two different doses of scAAV1-gThy1-CBh-mCherry. Data are mean ± SD, and significance was tested using one-way ANOVA with Tukey's multiple comparison test. ns, nonsignificant. ****P < 0.0001. **(M)** Flow cytometry overlay plot of surface TGFBR2 expression on NIH/3T3.Cas9 cells transduced with or without scAAV1-gTgfbr2 at an MOI of 1e6 and analyzed 72 h later. One of three representative experiments is shown. **(N)** Experimental scheme for bleomycin-induced skin fibrosis model. **(O)** Overlay histograms of TGFBR2 surface expression by flow cytometry on all skin fibroblasts isolated from non-lesional or lesional skin of *Pdgfra*-Cas9-EGFP mice treated as outlined in N. 3e10 vg scAAV1-gTrac (control) or scAAV1-gTgfbr2 were injected. GeoMFI values listed for each sample. MOI, multiplicity of infection.

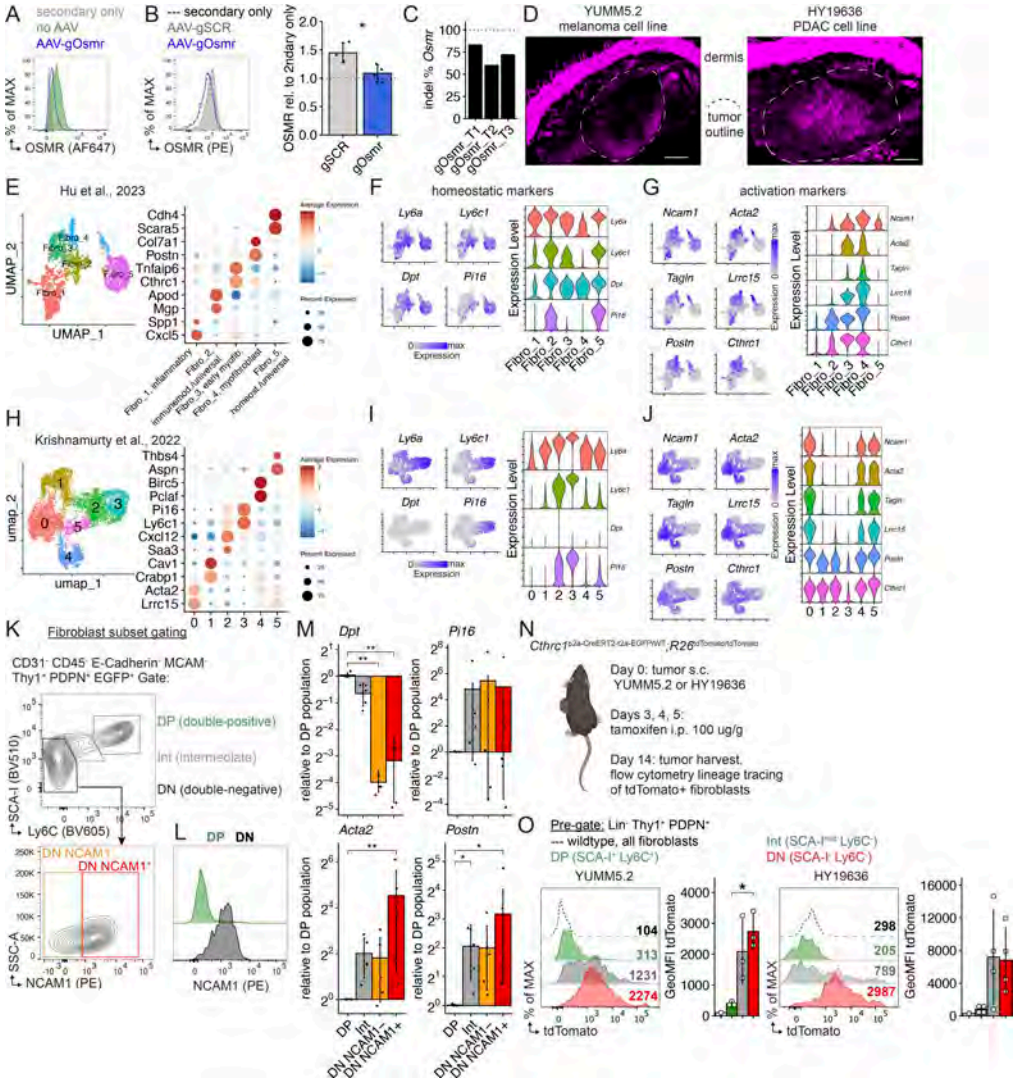

Figure S2. **Ly6C, SCA-I, and NCAM1 are markers for different CAF states. (A)** Flow cytometry overlay plot of surface OSMR expression on NIH/3T3.Cas9 cells treated with or without scAAV1-gOsmr at an MOI of 1e6 and analyzed 6 days later. One of three representative experiments is shown. **(B)** Left: Flow cytometry overlay plot of EGFP$^+$ tumor fibroblasts from *Pdgfra*-Cas9-EGFP mice injected s.c. with 3e10 vg AAV-gSCR (control) or AAV-gOsmr and YUMM5.2 tumor cells on subsequent days. Flow analysis done on day 14 after tumor challenge. Right: Quantification of OSMR (GeoMFI) surface expression on EGFP$^+$ tumor fibroblasts treated with control AAV-gSCR (control) or *Osmr*-targeting AAV-gOsmr (n = 3–4 tumors/group) normalized to secondary only stain control. Data are mean ± SD, and significance was tested using Welch's t test. One of two representative experiments is shown. GeoMFI, geometric mean fluorescence intensity. **(C)** Indel percentages as measured by ICE analysis of the *Osmr* KO locus from sorted CAFs from three different HY19636 tumors on day 14 after tumor injection s.c. and prior injection of 3e10 vg AAV-gOsmr on day −1. **(D)** SHG imaging (magenta) of s.c. injected (left) YUMM5.2 mouse melanoma and (right) HY19636 mouse pancreatic cancer cell lines to visualize fibrillar collagen deposition in tumor mass on day 10 in 150-µm-thick sections via maximum projection. Dermal skin layer at top of images is thresholded to visualize collagen deposition in tumor mass. White dotted line demarcates outline of tumor mass. Scale bar, 500 µm. One of three representative tumors for each cell line is shown. **(E)** Left: UMAP of mouse wound fibroblasts by Hu et al. (2023) analyzed by scRNA-seq and colored by cluster. Right: Dot plot showing relative average expression of marker genes across all clusters. **(F)** Fibroblast homeostatic marker gene expression in wound fibroblasts is highlighted (left) on the UMAP and (right) by cluster annotation. **(G)** Fibroblast activation marker gene expression in wound fibroblasts is highlighted (left) on the UMAP and (right) by cluster annotation. **(H)** Left: UMAP of mouse pancreatic tumor fibroblasts by Krishnamurty et al. (2022) analyzed by scRNA-seq and colored by cluster. Right: Dot plot showing relative average expression of marker genes across all clusters. **(I)** Fibroblast homeostatic marker gene expression in tumor fibroblasts is highlighted (left) on the UMAP and (right) by cluster annotation. **(J)** Fibroblast activation marker gene expression in tumor fibroblasts is highlighted (left) on the UMAP and (right) by cluster annotation. **(K)** Gating strategy to identify three different tumor fibroblast subsets: DP SCA-I$^+$ Ly6C$^+$, Int SCA-I^{mid} Ly6C^{mid}, and DN SCA-I$^-$ Ly6C$^-$. The fibroblast DN subset is further divided by NCAM1 low and high expression. **(L)** NCAM1 expression in DP (SCA-I$^+$ Ly6C$^+$) and DN (SCA-I$^-$ Ly6C$^+$) tumor fibroblasts. NCAM1 expression is absent in DP subset. **(M)** Tumor fibroblast subsets were isolated and sorted based on gating strategy in J from WT C57BL/6 mice challenged with 2.5e5 HY19636 s.c. on day 8–10 after tumor challenge. Gene expression of homeostatic genes *Dpt* and *Pi16* and activation genes *Acta2* and *Postn* were analyzed by quantitative real-time PCR. Data are mean ± SD, and significance was tested using one-way ANOVA with Tukey's multiple comparison test (n = 5 tumors, pooled from two experiments). **(N)** Experimental scheme to lineage trace *Cthrc1*-expressing cells in tumor-(YUMM5.2 or HY19636) challenged mice. **(O)** Representative overlay histograms of tdTomato expression in (Lin$^-$ [CD31 CD45 E-Cadherin MCAM] CD90.2$^+$ PDPN$^+$) tumor fibroblast cell subsets harvested from (left) YUMM5.2 or (right) HY19636 tumors. Quantification of tdTomato mean fluorescence intensity is plotted as mean ± SD (n = 3 YUMM5.2 tumors; n = 4 HY19636 tumors), and significance was tested using one-way ANOVA with Tukey's multiple comparison test. *P < 0.05, **P < 0.01. UMAP, uniform manifold approximation and projection; MOI, multiplicity of infection.

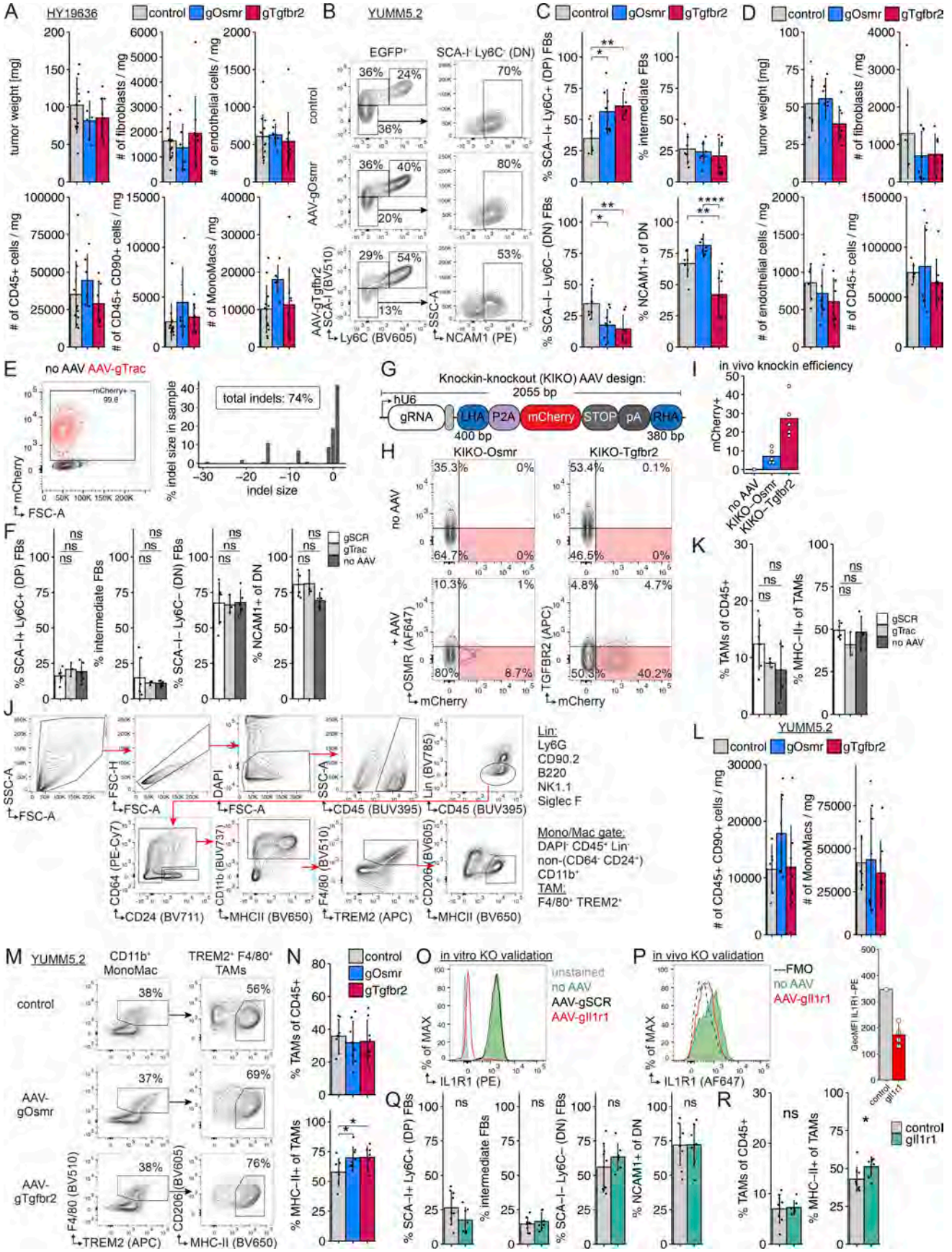

Figure S3. **Local *Osmr* or *Tgfbr2* KO in CAFs has similar effects in multiple tumor models. (A)** Quantification of tumor weight, fibroblasts (Lin$^-$ [CD31 CD45 E-Cadherin MCAM] CD90.2$^+$ PDPN$^+$ EGFP$^+$), endothelial cells (CD45$^-$ CD31$^+$), immune cells (CD45$^+$ CD31$^-$), and CD45$^+$ CD90$^+$ lymphocytes, and MonoMacs (CD45$^+$ Lin$^-$ CD11b$^+$) normalized by tumor weight in HY19636 pancreatic tumors on D14 after tumor challenge in mice treated with AAV outlined in Fig. 2 A. Data are mean ± SD (n = 6–13 tumors/group, pooled from four independent experiments). **(B)** Flow cytometry plots of (left) EGFP$^+$ tumor fibroblasts and (right) DN tumor fibroblasts from control-, AAV-gOsmr, or AAV-gTgfbr2–injected *Pdgfra*-Cas9-EGFP mice on day 14 after YUMM5.2 tumor challenge. One of two representative experiments is shown. **(C)** Quantification of EGFP$^+$ tumor fibroblast subsets from tumors with *Osmr* or *Tgfbr2* KO in fibroblasts. Data are mean ± SD, and significance was tested using one-way ANOVA with Tukey's multiple comparisons test (n = 7–8 tumors/group, pooled from two independent experiments). **(D)** Quantification of YUMM5.2 tumor weight and fibroblasts (Lin$^-$ CD90.2$^+$ PDPN$^+$ EGFP$^+$), endothelial cells (CD45$^-$ CD31$^+$), and immune cells (CD45$^+$ CD31$^-$) normalized by tumor weight. Data are mean ± SD (n = 6–8 tumors/group, pooled from two independent experiments). **(E)** NIH/3T3.Cas9 cells were transduced with genome cutting control AAV-gTrac at an MOI of 1e6 and 3 days later analyzed for (top) transduction efficiency by mCherry expression readout via flow cytometry and for (bottom) indel frequency as a readout of cutting at the *Trac* locus via ICE analysis. One of two representative experiments is shown. **(F)** Quantification of EGFP$^+$ tumor fibroblast subsets from tumors of different control groups—1-3e10 vg AAV-gSCR or AAV-gTrac (genome cutting control), and "no AAV"—in HY19636 mouse pancreatic cancer models on day 14 after tumor challenge. Data are mean ± SD, and significance was tested using one-way ANOVA with Tukey's multiple comparison test (n = 3–6 tumors/group). **(G)** Design of KIKO AAV cassette to insert payload (mCherry ORF) and targeting gene of interest for (gRNA) for gene KO. LHA, left homology arm; RHA, right homology arm. **(H)** *In vivo* KIKO of target genes *Osmr* or *Tgfbr2* in tumor fibroblasts. Flow cytometry contour plots of EGFP$^+$ tumor fibroblasts from *Pdgfra*-Cas9-EGFP mice injected s.c. with 3e10 vg AAV-KIKO-gRNA-mCherry-STOPpA and HY19636 tumor cells on subsequent days. Flow analysis done on day 10 after tumor challenge. Bottom right quadrant highlights receptor-negative, mCherry$^+$ fibroblasts with successful KIKO. One of two representative experiments is shown. **(I)** Quantification of mCherry$^+$ tumor fibroblasts from H as a readout for KIKO efficiency (n = 5 per KIKO group; pooled from two independent experiments). **(J)** Gating strategy for Mono/Mac and TAM identification in mouse tumors. TAMs gated as DAPI$^-$ CD45$^+$ Ly6G$^-$ CD90.2$^-$ B220$^-$ NK1.1$^-$ SiglecF$^-$ non-(CD64$^-$ CD24$^+$) CD11b$^+$ F4/80$^+$ TREM2$^+$. **(K)** Same control group comparison as in F for TAM comparison in HY19636 mouse pancreatic cancer tumors. Data are mean ± SD and significance was tested using one-way ANOVA with Tukey's multiple comparison test (n = 3–6 tumors/group). **(L)** Quantification of CD45$^+$ CD90$^+$ lymphocytes, and MonoMacs (CD45$^+$ Lin$^-$ CD11b$^+$) normalized by tumor weight in YUMM5.2 melanoma on day 14 after tumor challenge in mice treated with AAV outlined in Fig. 2 A. Data are mean ± SD (n = 6–8 tumors/group, pooled from two independent experiments). **(M)** Flow cytometry plots of (left) CD11b$^+$ MonoMacs and (right) F4/80$^+$ TREM2$^+$ TAMs from YUMM5.2 tumors with *Osmr* or *Tgfbr2* KO in fibroblasts as treated in Fig. 2 A. One of two representative experiments is shown. **(N)** Quantification of M. Data are mean ± SD, and significance was tested using one-way ANOVA with Dunnett's multiple comparisons test (n = 7–8 tumors/group, pooled from two independent experiments). **(O)** *In vitro* validation of scAAV1-gIl1r1. Flow cytometry overlay plot of surface expression on NIH/3T3.Cas9 cells infected with control AAV (scAAV1-gSCR) or scAAV1-gIl1r1 at a MOI of 1e6 and analyzed 6 days later. One of two representative experiments is shown. **(P)** *In vivo* validation of AAV-mediated *Il1r1* KO. Representative flow cytometry overlay plot of EGFP$^+$ tumor fibroblasts from *Pdgfra*-Cas9-EGFP mice injected s.c. with 3e10 vg AAV-gIl1r1 and HY19636 tumor cells on subsequent days. Flow analysis done on day 14 after tumor challenge. Quantification of IL1R1 surface expression (GeoMFI) on EGFP$^+$ tumor fibroblasts treated with AAV-gIl1r1 are plotted as mean ± SD (n = 1–4/group). One of two representative experiments is shown. **(Q)** Quantification of EGFP$^+$ tumor fibroblast subsets in *Pdgfra*-Cas9-EGFP mice 14 days after s.c. challenge with HY19636 tumor cells and prior local KO of *Il1r1* in fibroblasts via 3e10 vg AAV-gIl1r1 s.c. injection. Data are mean ± SD, and significance was tested using Welch's t test (n = 7–9 tumors/group, pooled from two independent experiments). **(R)** Quantification of TAMs and MHCII-hi TAMs in tumors from Q. MOI, multiplicity of infection. *P < 0.05, **P < 0.01, and ****P < 0.0001.

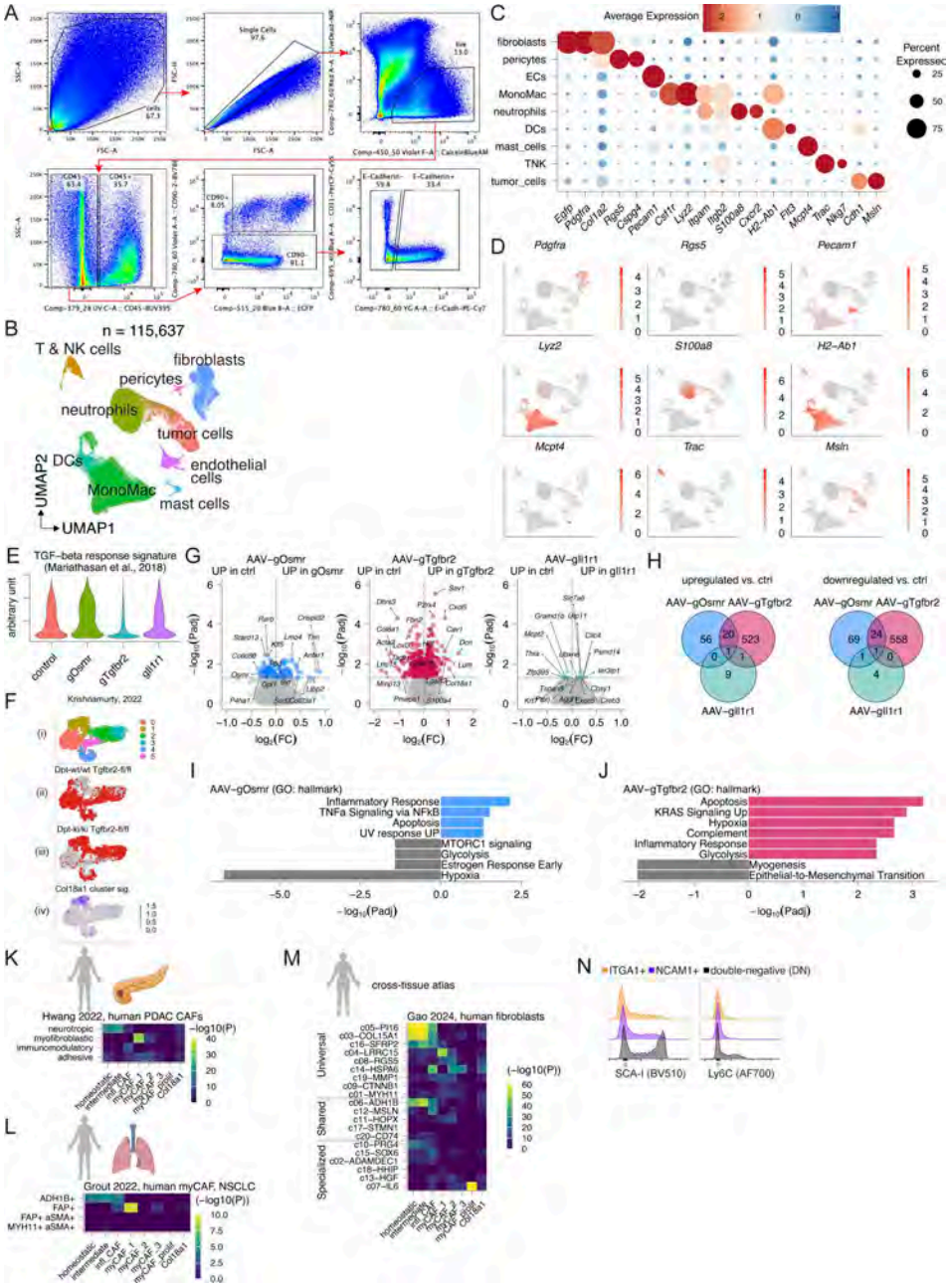

Figure S4. **Comparative single-cell RNA sequencing analysis reveals unique CAF state after local *Tgfbr2* KO. (A)** Gating scheme for sorting cells in Fig. 3 A. **(B)** Uniform manifold approximation and projection (UMAP) of all collected cells by scRNA-seq. **(C)** Bubble plot of scaled marker gene expression in main cell types identified in Fig. S4 B. EC, endothelial cells; TNK, T and NK cells. **(D)** UMAP visualization of marker gene expression in all captured cells. **(E)** Violin plot depicting mean expression of TGF-beta response signature by Mariathasan et al (2018) in CAFs grouped by AAV-gRNA condition. **(F)** UMAP visualization of CAFs by Krishnamurty et al. (2022) (reanalyzed mouse PDAC scRNA-seq data set) colored by (1) cluster, CAFs identified in (2) $Dpt^{wt/wt}$;$Tgfbr2^{fl/fl}$ control or (3) $Dpt^{ki/ki}$;$Tgfbr2^{fl/fl}$ mice with conditional *Tgfbr2* KO in fibroblasts, and (4) Col18a1 CAF cluster signature expression. AAV-gTgfbr2–induced Col18a1 CAFs also appear in *Tgfbr2* KO mice challenged with PDAC tumor. **(G)** Volcano plots of differentially expressed genes (DEG, pseudobulk scRNA-seq) in CAFs between control (AAV-gTrac) and (left) AAV-gOsmr, (middle) AAV-gTgfbr2, or (right) AAV-gIl1r1. Selected genes are highlighted. Y-axis shows Benjamini–Hochberg adjusted P values (−log10 scale). Dotted line demarcates significant genes as defined by adjusted P value <0.05. X-axis shows log2 fold-change (FC) between control and experimental group. **(H)** Venn diagram of (left) upregulated and (right) downregulated DEGs between control (ctrl) and AAV-gOsmr, AAV-gTgfbr2, or AAV-gIl1r1. **(I and J)** Enriched gene sets (Gene Ontology hallmark) based on the up- and downregulated DEGs between control and (I) AAV-gOsmr and (J) AAV-gTgfbr2. **(K–M)** Similarity of DEGs between mouse CAF subsets (columns) and (K) human PDAC CAF subsets from Hwang et al. (2022) (rows) or (L) human non-small cell lung carcinoma CAF subsets from Grout et al. (2022) or (M) cross-tissue human fibroblast atlas subtypes from Gao et al. (2024). Statistical significance of DEG overlap (−log10 [P value], hypergeometric test, P value adjusted using Bonferroni correction) for each pairwise comparison plotted as heatmap. Yellow indicates high statistically significant overlap of DEG lists. Human genes from gene lists by Hwang et al. (2022), Grout et al. (2022), and Gao et al. (2024) were relabelled as their mouse orthologs prior to comparison. **(N)** Flow cytometry histograms of homeostatic fibroblast markers (left) SCA-I and (right) Ly6C in CAF subpopulations as gated in Fig. 3 I. DN CAFs have the highest expression of homeostatic markers. One of three representative experiments is shown.

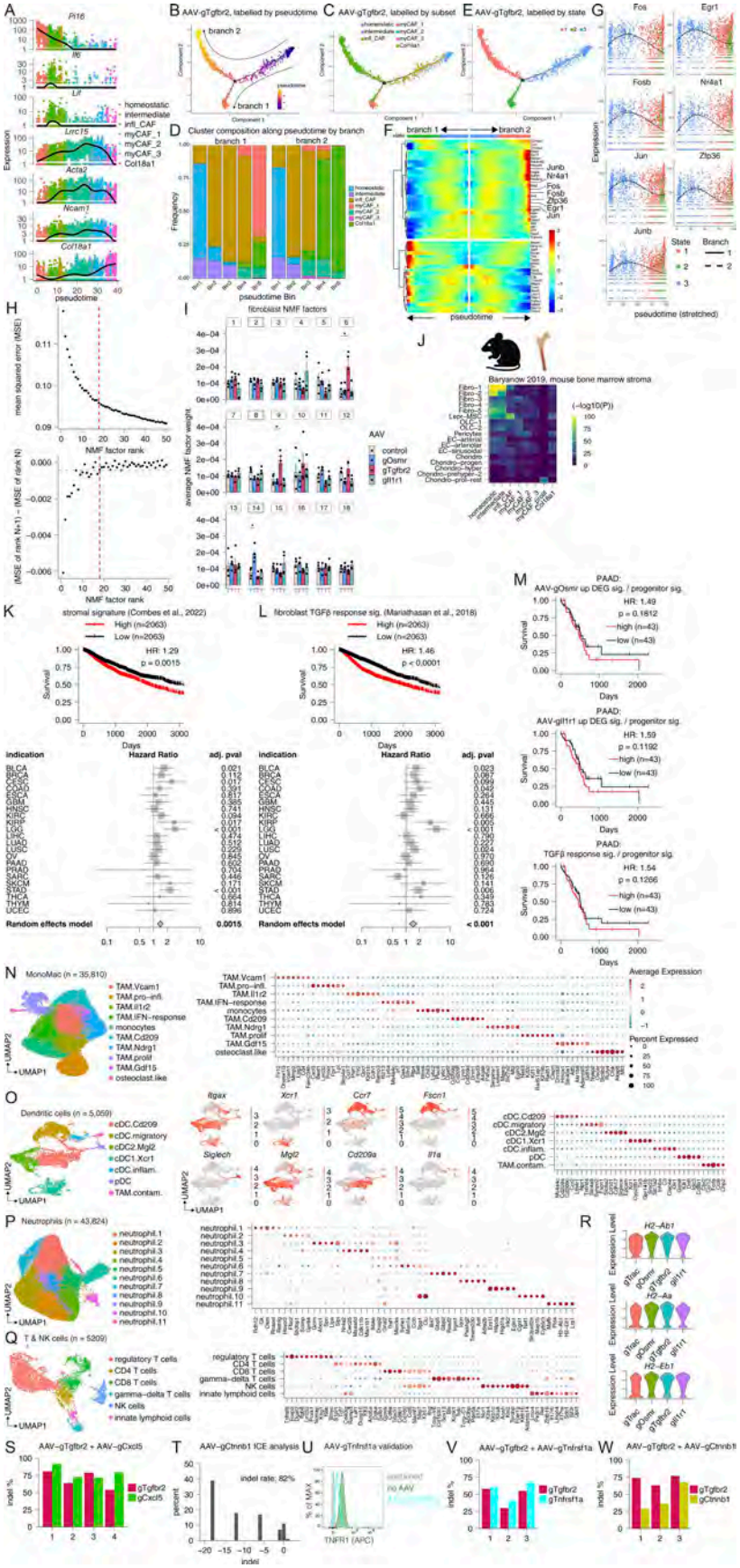

Figure S5. **Single-cell trajectory analysis of AAV-gTgfbr2 CAFs, NMF of CAF gene expression, and survival analysis using CAF-derived signatures highlights distinct transcriptional state of *Tgfbr2* KO CAFs. (A)** Gene expression of select genes (homeostatic *Pi16*; inflammatory *Il6* and *Lif*; myofibroblast-associated *Lrrc15*, *Acta2*, and *Ncam1*; AAV-gTgfbr2-associated *Col18a1*) along pseudotime in CAFs from Fig. 4 A. **(B)** Pseudotime distribution along Monocle 2–generated trajectory of AAV-gTgfbr2 CAFs. Black circle labelled "1" marks the branchpoint generating two trajectories (branch 1 and branch 2). **(C)** AAV-gTgfbr2 CAF subsets labelled on Monocle 2–generated pseudotime trajectory. **(D)** To quantify AAV-gTgfbr2 CAF subset distribution along the two branches, cells were divided into five equal pesudotime bins along each branch (branch 1, myCAF_1-associated; branch 2, Col18a1-associated). Within each bin, the relative frequency of each CAF cluster was calculated and plotted as a function of pseudotime progression. **(E)** AAV-gTgfbr2 CAFs labelled by states that change as a function of pseudotime relative to the branchpoint. **(F)** Heatmap of differentially expressed genes between branch 1 (myCAF_1 trajectory) and branch 2 (Col18a1) trajectory. Gene expression is plotted relative to pseudotime for each trajectory, with the beginning of pseudotime set at the middle of the y-axis. The branchpoint for each trajectory is marked by the cell state change from state "3" (blue) to the other color. **(G)** Gene expression of seven transcription factors differentially expressed between branch 1 (myCAF_1 trajectory) and branch 2 (Col18a1 trajectory) along pseudotime. Solid (branch 1) and dashed (branch 2) lines represent smoothed expression profile for the two divergent trajectories. **(H)** Top: MSE of an NMF model vs. model factorization rank (k = 1–50) in the fibroblast object. Vertical dotted line at k = 18 highlights model selected for analysis. Bottom: Delta between MSE values from successive NMF model ranks to better visualize inflection point of top graph as defined by the point where the values plateau (highlighted by gray dotted line). **(I)** Bar charts of average expression of NMF factors in CAFs grouped by AAV-gRNA condition plotted as mean ± SEM (n = 4 per group). *P < 0.05 one-way ANOVA with Dunnett's multiple comparison test. **(J)** Similarity of DEGs between mouse CAF subsets (columns) and mouse bone marrow stroma cells by Baryawno et al. (2019) (rows). Statistical significance of DEG overlap (−log10 [P value], hypergeometric test, P value adjusted using Bonferroni correction) for each pairwise comparison plotted as heatmap. Yellow indicates high statistically significant overlap of DEG lists between annotated subsets. **(K)** Top: Kaplan–Meier survival plots of TCGA patients categorized into upper and lower quartiles by the stroma score identified by Combes et al. (2022). Hazard ratio (HR) and P value of Cox regression fit are shown. Bottom: Forest plot of hazard ratios ±95% confidence interval and Benjamini–Hochberg procedure-adjusted P values (adj. pval) in Cox regression model for overall survival of TCGA patients separated by indication and categorized into upper and lower quartiles by stroma score. **(L)** Top: Kaplan–Meier survival plots of TCGA patients categorized into upper and lower quartiles by the fibroblast TGFβ response signature by Mariathasan et al. (2018). Hazard ratio (HR) and P value of Cox regression fit are shown. Bottom: Forest plot of hazard ratios ±95% confidence interval and Benjamini–Hochberg procedure-adjusted P values (adj. pval) in Cox regression model for overall survival of TCGA patients separated by indication and categorized into upper and lower quartiles by fibroblast TGFβ response signature. **(M)** Kaplan–Meier survival plots of PAAD patients from TCGA excluding PNET (pancreatic neuroendocrine tumor) diagnosed patients categorized into upper and lower quartiles by the ratio of (top) AAV-gOsmr DEG signature from this study, (middle) AAV-gIl1r1 DEG signature from this study, or (bottom) TGFβ response signature by Mariathasan et al. (2018) to the fibroblast progenitor signature (see Materials and methods for details). The mouse-derived AAV-gOsmr and AAV-gIl1r1 DEG signatures were generated using human orthologs. Hazard ratio (HR) and P value of Cox regression fit are shown. **(N)** Left: UMAP of MonoMac cell subsets from all AAV-gRNA tumors. Right: Bubble plot of scaled differentially expressed genes (DEGs) in MonoMac cell subsets. **(O)** Left: UMAP of DC subsets from all AAV-gRNA tumors. Middle: UMAP visualization of select DC marker genes in the DC object. Right: Bubble plot of scaled DEGs in DC subsets. **(P)** Left: UMAP of neutrophil subsets from all AAV-gRNA tumors. Right: Bubble plot of scaled DEGs in neutrophil subsets. **(Q)** Left: UMAP of lymphoid cell subsets from all AAV-gRNA tumors. Right: Bubble plot of scaled DEGs in lymphoid cell subsets. **(R)** Violin plots of *H2-Ab1*, *H2-Aa*, and *H2-Eb1* expression in the TAM.Ndrg1 subset, grouped by AAV-gRNA tumors. **(S)** Indel percentage at gTgfbr2 and gCxcl5 cut sites in EGFP$^+$ tumor fibroblasts sorted from *Pdgfra*-Cas9-EGFP mice on day 14 after 2.5e5 HY19636 s.c. cell injection with combinatorial 2e10 vg AAV-gTgfbr2 and 3e10 AAV-gCxcl5 injection on day −1. Four different tumor samples are plotted. **(T)** Histogram depicting insertion/deletion (indel) distribution in NIH/3T3.Cas9 cells at gCtnnb1 cut site 3 days after transduction with AAV-gCtnnb1, as analyzed by ICE analysis. **(U)** Flow cytometry histogram overlay plot of surface TNF receptor 1 (TNFR1) expression on NIH/3T3.Cas9 cells transduced with or without scAAV1-gTnfrsf1a at an MOI of 1e6 and analyzed 72 h later. One of two representative experiments is shown. **(V)** Indel percentage at gTgfbr2 and gTnfrsf1a cut sites in EGFP$^+$ tumor fibroblasts sorted from *Pdgfra*-Cas9-EGFP mice on day 14 after 2.5e5 HY19636 s.c. cell injection with combinatorial 2e10 vg AAV-gTgfbr2 and 3e10 AAV-gTnfrsf1a injection on day −1. Three different tumor samples are plotted. **(W)** Indel percentage at gTgfbr2 and gCtnnb1 cut sites in EGFP$^+$ tumor fibroblasts sorted from *Pdgfra*-Cas9-EGFP mice on day 14 after 2.5e5 HY19636 s.c. cell injection with combinatorial 2e10 vg AAV-gTgfbr2 and 3e10 AAV-gCtnnb1 injection on day −1. Three different tumor samples are plotted. UMAP, uniform manifold approximation and projection. MOI, multiplicity of infection. MSE, mean squared error.

Provided online are Table S1, Table S2, Table S3, Table S4, Table S5, and Table S6. Table S1 shows the DEGs for each cell subtype identified within major cell types. Table S2. shows the DEGs of AAV-gRNA groups using pairwise pseudobulk differential gene expression analysis comparing control (AAV-gTrac) with experimental groups (AAV-gOsmr, AAV-gTgfbr2, or AAV-gIl1r1). Table S3 shows the weighted gene output ordered by non-NMF factors from fibroblast object. Table S4 shows the signature genes used for survival analysis. Table S5 shows the DNA sequences of plasmids and gRNAs used in this study. Table S6 shows the table of reagents used in this study.